

AD-A218 373

DTIC FILE COPY

6

## DYNAMIC FRACTURE OF CONCRETE

## PART II

Approved for public release;  
distribution unlimited.

## Jung Heum Yon Department of Civil Engineering

**A.S. Kobayashi**  
**Department of Mechanical Engineering**

**Neil M. Hawkins  
Department of Civil Engineering**

**University of Washington  
Seattle, WA 98195**

### Prepared for

**Air Force Office of Scientific Research  
Bolling Air Force Base  
Washington, DC 20332-6448**

## Final Report on AFOSR Contract 86-0204

**February 14, 1990**

### **Distribution Unlimited:**

DTIC  
ELECTED  
FEB 26 1990  
S B D  
No

90 02 23 062

UNCLASSIFIED

SECURITY CLASSIFICATION OF THIS PAGE

Form Approved  
OMB No. 0704-0188

## REPORT DOCUMENTATION PAGE

1a. REPORT SECURITY CLASSIFICATION Unclassified		1b. RESTRICTIVE MARKINGS	
2a. SECURITY CLASSIFICATION AUTHORITY		3. DISTRIBUTION/AVAILABILITY OF REPORT	
2b. DECLASSIFICATION/DOWNGRADING SCHEDULE		Unlimited	
4. PERFORMING ORGANIZATION REPORT NUMBER(S)		5. MONITORING ORGANIZATION REPORT NUMBER(S) <b>AFOSR-TR-90-0208</b>	
6a. NAME OF PERFORMING ORGANIZATION University of Washington	6b. OFFICE SYMBOL (If applicable) UWCE	7a. NAME OF MONITORING ORGANIZATION Air Force Office of Scientific Research	
6c. ADDRESS (City, State, and ZIP Code) Department of Civil Engineering Seattle, WA 98195		7b. ADDRESS (City, State, and ZIP Code) Bolling Air Force Base Washington, D.C. 20332	
8a. NAME OF FUNDING/SPONSORING ORGANIZATION Air Force Office of Sci Res	8b. OFFICE SYMBOL (If applicable) AFOSR /NA	9. PROCUREMENT INSTRUMENT IDENTIFICATION NUMBER AFOSR-86-0204	
8c. ADDRESS (City, State, and ZIP Code) Bolling Air Force Base Washington, D.C. 20332		10. SOURCE OF FUNDING NUMBERS PROGRAM ELEMENT NO. 61102F PROJECT NO. 2302 TASK NO. C2 WORK UNIT ACCESSION NO.	
11. TITLE (Include Security Classification) Dynamic Fracture of Concrete, Part II			
12. PERSONAL AUTHOR(S) J.H. Yon, N.M. Hawkins, A.S. Kobayashi			
13a. TYPE OF REPORT Final	13b. TIME COVERED FROM 15/06/86 TO 14/12/89	14. DATE OF REPORT (Year, Month, Day) 1990 February 14	15. PAGE COUNT 128
16. SUPPLEMENTARY NOTATION			
17. COSATI CODES		18. SUBJECT TERMS (Continue on reverse if necessary and identify by block number) Concrete fracture, fracture process zone, moire interferometry, dynamic finite element analysis	
19. ABSTRACT (Continue on reverse if necessary and identify by block number)			
<p>A displacement controlled dynamic test system and instrumentation for dynamic fracture testing of concrete specimens, was developed. Also a hybrid experimental-numerical procedure for evaluating the dynamic fracture data thus generated was developed. The experimental data consisted of the applied load and transient strains in single edge notched, three point bend specimens which were subjected to controlled displacement loading. In addition, moire interferometry data was obtained in three point bend specimens subjected drop weight loading. Also the applied load, transient strains and crack opening displacement were measured in crack-line wedge-loaded, double cantilever beam specimens which were subjected to controlled wedge displacement loading. These test systems and the hybrid analysis were used to determine the strain rate sensitivity of the elastic properties and the fracture process zone of rapidly fracturing concrete specimens. The increase in both tensile and compressive moduli of elasticity and the tensile strength with increasing strain rate were quantified. The fracture process zone decreased in magnitude with increasing strain rate but the tensile strength necessary to propagated the tip of the fracture process zone under a tensile strength criterion increased substantially with the strain rate. The net effect was that dynamic fracture responses of a rapidly propagating crack in concrete resembled that of linear elasto-dynamic fracture mechanics with influence of the fracture process zone decreasing with increasing strain rate of loading.</p>			
20. DISTRIBUTION/AVAILABILITY OF ABSTRACT <input checked="" type="checkbox"/> UNCLASSIFIED/UNLIMITED <input type="checkbox"/> SAME AS RPT. <input type="checkbox"/> DTIC USERS		21. ABSTRACT SECURITY CLASSIFICATION Unclassified	
22a. NAME OF RESPONSIBLE INDIVIDUAL Dr. Spencer Wu		22b. TELEPHONE (Include Area Code) (202) 767-6962	22c. OFFICE SYMBOL AFOSR/NA

AMERICAN INSTITUTE

Research sponsored by the Air Force Office of Scientific Research, Air Force Systems Command, USAF, under grant or cooperative agreement number, AFOSR 86-0204. The US Government is authorized to reproduce and distribute reprints for Governmental purposes notwithstanding any copyright notation thereon.

This manuscript is submitted for publication with the understanding that the US Government is authorized to reproduce and distribute reprints for Governmental purposes.

## Abstract

A displacement controlled dynamic test system and instrumentation for dynamic fracture testing of concrete specimens, was developed. Also a hybrid experimental-numerical procedure for evaluating the dynamic fracture data thus generated was developed. The experimental data consisted of the applied load and transient strains in single edge notched, three point bend specimens which were subjected to controlled displacement loading. In addition, moire interferometry data was obtained in three point bend specimens subjected drop weight loading. Also the applied load, transient strains and crack opening displacement were measured in crack-line wedge-loaded, double cantilever beam specimens which were subjected to controlled wedge displacement loading. These test systems and the hybrid analysis were used to determine the strain rate sensitivity of the elastic properties and the fracture process zone of rapidly fracturing concrete specimens. The increase in both tensile and compressive moduli of elasticity and the tensile strength with increasing strain rate were quantified. The fracture process zone decreased in magnitude with increasing strain rate but the tensile strength necessary to propagated the tip of the fracture process zone under a tensile strength criterion increased substantially with the strain rate. The net effect was that dynamic fracture responses of a rapidly propagating crack in concrete resembled that of linear elasto-dynamic fracture mechanics with influence of the fracture process zone decreasing with increasing strain rate of loading.

(S) T

By	
Distribution/	
Availability Codes	
Dist	Avail and/or Special
R-1	

DTIC  
COPY  
REPRODUCED  
BY

## Table of Contents

1. Introduction and Objectives .....	1
1.1 General Remarks .....	1
1.2 Objectives .....	2
1.3 Scope .....	3
2. Literature Review .....	4
2.1 Introduction .....	4
2.2 Fracture Behavior of Concrete .....	6
2.3 Dynamic Fracture Test Methods .....	13
.1 Drop-Weight Test .....	13
.2 Instrumented Drop Weight Test .....	13
.3 Charpy Impact Test .....	14
.4 Modified Charpy Test .....	14
.5 Split Hopkinson Bar Test .....	15
.6 Dynamic Tensile Test .....	16
.7 Explosive Test .....	16
.8 Constant Strain Rate Test .....	17
2.4 Strain Rate Sensitivities of Mechanical Properties of Concrete .....	17
3. Experimental and Analytical Procedures .....	26
3.1 Displacement-Controlled Dynamic Fracture Test System .....	26
3.2 Impact Loading Test System .....	30
3.3 Experimental Test Program .....	33
3.4 Numerical Analysis .....	35
.1 Dynamic Finite Element Analysis .....	35
.2 Application of Crack Closure Stress .....	36

.3	Modeling of Continuous Crack Propagation .....	37
.4	Determination of Mechanical Properties of Concrete .....	40
.1	Hybrid Experimental-Numerical Technique..	42
.2	Elastic Properties.....	43
.3	Fracture Properties.....	45
4.	Displacement Controlled Three-Point-Bend Tests .....	47
4.1	Experimental Set-Up .....	47
4.2	Numerical Analysis .....	50
4.3	Results .....	53
.1	Experimental Results .....	53
.2	Numerical Results .....	57
.3	Strain Rate Sensitivity of Mechanical Properties .....	65
4.4	Discussion .....	68
4.5	Conclusions .....	73
5.	Impact Loading Three-Point Bend Tests with Moire Interferometry .....	75
5.1	Introduction .....	75
5.2	Numerical Analysis .....	75
5.3	Results .....	79
.1	Experimental Results .....	79
.2	Numerical Results .....	87
.3	Strain Rate Sensitivity .....	92
5.4	Discussion .....	93
5.5	Conclusions .....	97

6. Crack-Line, Wedge-Loaded Double-Cantilever Beam Tests	99
6.1 CLWL-DCB Tests .....	99
6.2 Numerical Analysis .....	106
6.3 Results .....	108
.1 Experimental Results .....	108
.2 Numerical Results .....	117
6.4 Discussion .....	117
6.5 Conclusions .....	118
7. Summary .....	120
8. Publications from This Study and Related Work .....	123
9. Recommendation for Future Research .....	126
9.1 Justification .....	126
9.2 Recommended Research .....	127
9.3 Relevancy .....	129
References .....	130

## CHAPTER ONE

### INTRODUCTION

#### 1.1 General Remarks

In Part I of this report, a general survey of the literature on fracture mechanics and dynamic fracture testing of concrete was provided. A constitutive relation, which related the crack closure stress and crack-opening displacement (COD) in quasi-statically fracturing three-point-bend and crack-line, wedge-loaded, double cantilever beam (CLWL-DCB) concrete specimens was obtained by a hybrid experimental-numerical procedure. The procedure consisted of matching the computed COD with the COD measured by Moire interferometry. The former was obtained through an elastic finite element analysis of the concrete fracture specimens with a postulated constitutive equation relating the the crack closure stress and the COD. This constitutive relation was then used successfully to model the dynamic fracture responses of published experimental results of impacted three-point bend concrete specimens.

In this Part II, the results of experiments on hybrid experimental-numerical analyses of dynamically loaded three-point bend and CLWL-DCB concrete specimens are reported. For four fracturing three-point bend specimens, moire interferometry was also used to measure the transient COD distributions.

## 1.2 Objectives

The objective of this research is to delineate the dynamic fracture mechanism of concrete under mode I loading. The ultimate objectives of this research are to obtain an accurate description of the strain rate sensitivity of the mechanical properties of concrete and a numerical simulation of the dynamic fracture behavior of concrete.

To achieve those objectives, the following four tasks were completed:

1. A displacement controlled dynamic fracture test system was developed.
2. The strain rate sensitivity of concrete was established through testing two different types of specimens, a three-point bend specimen and a crack-line wedge-loaded, double-cantilever beam (CLWL-DCB) specimen.
3. A numerical model of the propagating crack with a fracture process zone (FPZ) was developed.
4. An inverse technique was developed for determining the mechanical properties required to simulate accurately the global experimental responses.

### 1.3 Scope

Details of the dynamic loading research accomplished to date are documented in this report. Those results are preceded in Chapter 2 by a literature survey on dynamic fracture of concrete. Chapter 3 describes general features of the dynamic loading system, instrumentation and data recording systems used along with general details of the numerical analysis procedures. Chapter 4 describes the findings from the displacement controlled three point bend tests including details of the test results and their evaluation. Chapter 5 describes the findings from the impact loading tests on three point bend tests together with details of the test results and their evaluation. Chapter 6 describes the results of the displacement controlled tests on CLWL-DCB specimens. Chapter 7 summarizes the investigation and the principal conclusions that can be drawn from it. Publications from this study and related work are summarized in Chapter 8 and recommendations for continuation of this work are presented in Chapter 9.

CHAPTER TWO  
LITERATURE REVIEW ON  
DYNAMICS FRACTURE MECHANICS OF CONCRETE

**2.1 Introduction**

Although concrete is a very common structural material, the state of science relating to its fracture, particularly its dynamic fracture, lags behind the current advanced state of science for dynamic fracture of metals and polymers. For concrete members, where failure is controlled by yielding of the reinforcement or crushing of the concrete, common practice provides reasonably reliable information. However, for members with failure modes controlled by crack propagation considerations, i.e., concrete fracture, diagonal tension failure or splitting failures, common practice does not yield reliable information since little is known about dynamic crack propagation in concrete under dynamic loading.

While research on the dynamic fracture properties of concrete is in its infancy [1,2], the extensive non-linear effects present in the static fracture of concrete suggest that the direct technology transfer of linear elastodynamic fracture mechanics concepts from brittle materials to concrete is not likely to be successful. Indeed, available evidence [3] suggests that dynamic fracture of concrete, in the absence of crack curving, closely mimics dynamic ductile tearing which reduces the crack driving force and hence the crack velocity in metals

and polymers [4]. The similarities between the apparent dynamic fracture responses of ductile metals/polymers and concrete suggest that plastic deformation in the former can be replaced by aggregate crack bridging in the latter. The dynamic extension of the similarity between the static Dugdale strip yield zone [5] for ductile metals/polymers and the static fracture process zone due to aggregate crack bridging forces in concrete [6-8], is, however, not straight forward due to the large increases in tensile strength [9-12], and the even greater relative increases in energy absorption [3], reported for concrete loaded dynamically.

For both static and dynamic loadings, crack propagation in concrete is a continuous process and the resulting failure, unlike fracture in metals and polymers occurs relatively slowly. Even for concrete subjected to static loading, a crack takes time to fully develop [13,14], and therefore it is only to be expected that, for dynamic loadings, cracks propagate at relatively low velocities [15].

The foregoing observations suggest two mechanistic changes in the resistance of concrete to crack propagation with increasing strain rates. One change reflects the behavioral change from a domination by aggregate crack bridging forces for the fully developed fracture process zone present in static fracture, to a mechanism involving only a partially developed zone for dynamic loading. The slow crack velocity for dynamic

loading makes it distinctly possible that the energy input drops off before the fracture process zone is fully developed. The second mechanism involves the development of relatively more micro-cracking, along and in the vicinity of the line of the extending crack, for dynamic as opposed to static loading. More micro-cracking would result effectively in a more circuitous crack, and therefore greater energy absorption with increasing strain rates.

## **2.2 Fracture Behavior of Concrete**

Concrete can be modeled as a composite material consisting of aggregates and hardened cement paste. The elastic moduli of the aggregates and paste are essentially constant to the point of failure [16]. As shown in Figure 2.1 the behavior of concrete is highly nonlinear due to bond cracks between the aggregates and paste, and progressive cracking as the load increases [17]. The numerous bond cracks that exist at the interfaces between mortar and coarse aggregates in concrete specimens that have never been loaded are generated by: water lenses, which develop under coarse aggregates during setting of the fresh concrete; volume change in the cement during hydration; and dry shrinkage of hardened concrete [16-19]. The stress-strain curve for concrete loaded in compression can be divided into the four parts shown in Fig. 2.2 [20]. Within each part, there are different growth rates for the bond cracks between the

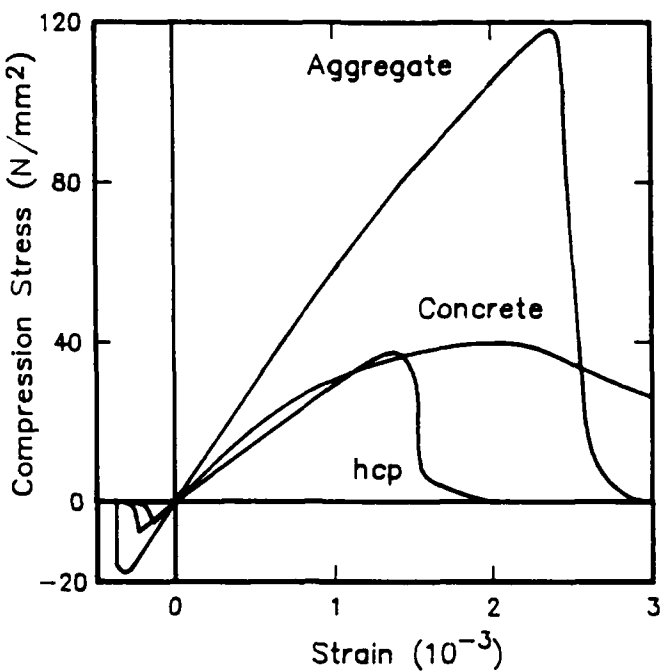


Figure 2.1: Stress-Strain Diagram of Hardened Cement Paste, Aggregate and Concrete [16].

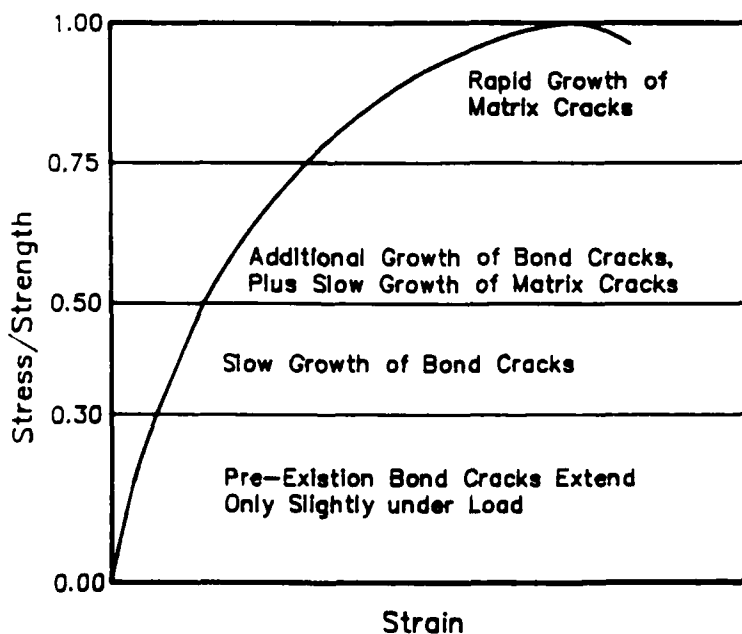


Figure 2.2: Stress-Strain Curve for Concrete under Compressive Loading [20].

aggregate and the matrix and the cracks within the matrix itself. Figure 2.3 shows cracking maps drawn from X-ray images [22] of a model of concrete during loading. Those maps illustrate the relative developments with loading of bond and matrix cracks.

Fracture behavior in tension is very important since fracture under compression is actually initiated by tension forces. However, only a few experiments on the complete stress-deformation behavior in tension are presented in literature [23-29]. The early experiments of Evans and Marathe [24] showed that the cracking occurred between 90 and 140 micro-strain, and that the corresponding normal stress is between 68 and 89 percent of the maximum average stress. These values were larger than those (30 to 80 micro-strain) reported by Kaplan's [30] because of the initiation of micro-cracks within the gage length. The strain reading for cracking was found to be gage-length dependent.

Figure 2.4 shows a typical example of the results from the direct tension test conducted by Reinhardt and his co-workers [28]. The experimental stress in Figure 2.4 (a) is calculated from the measured force and the original cross-sectional area; the model stress is the average stress of the stress distribution curve in Figure 2.4 (b); and the deformation is the mean value on a gage length of 35 mm. The stress distributions in Figure 2.4 (b) were calculated from the

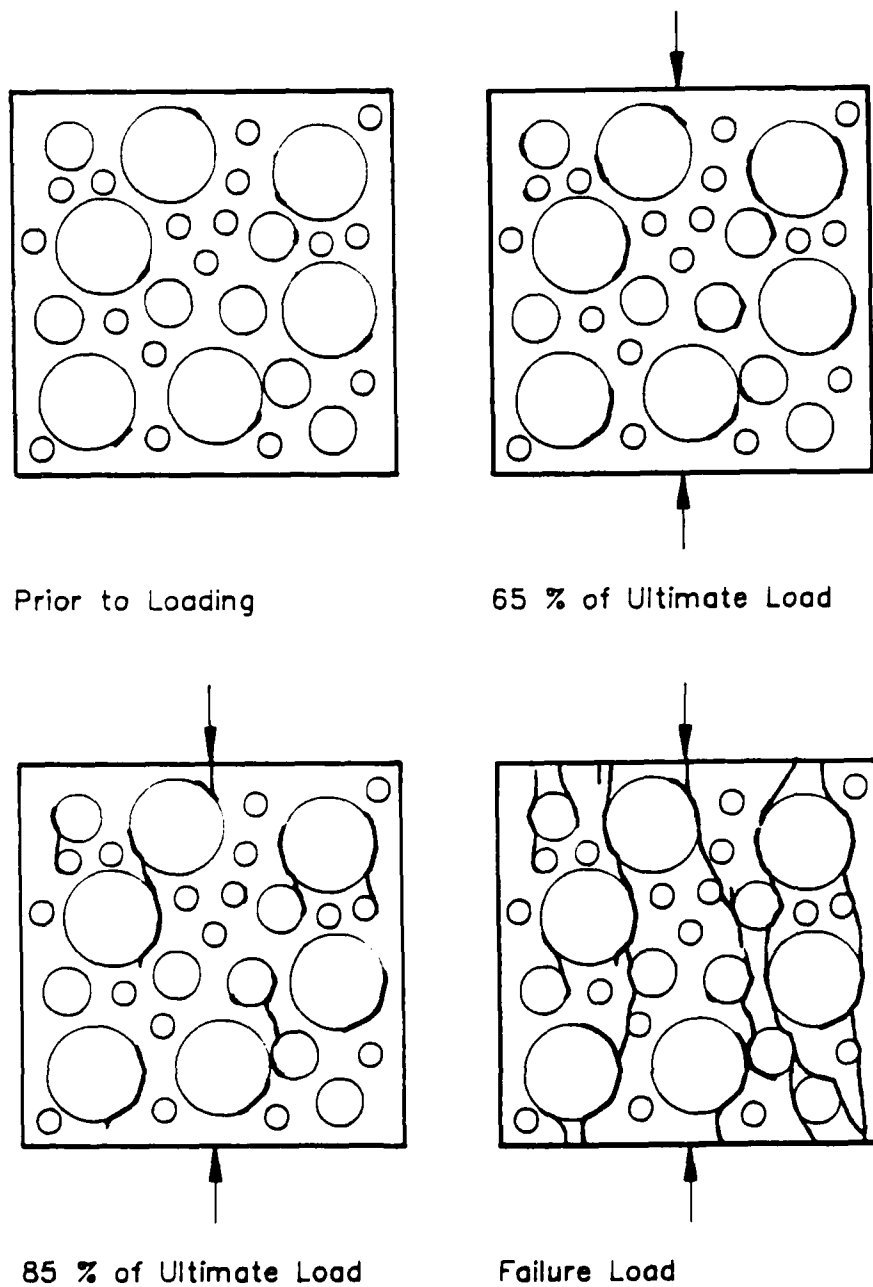


Figure 2.3: Progressive Cracking of Concrete under Uniaxial Compressive Loading [22].

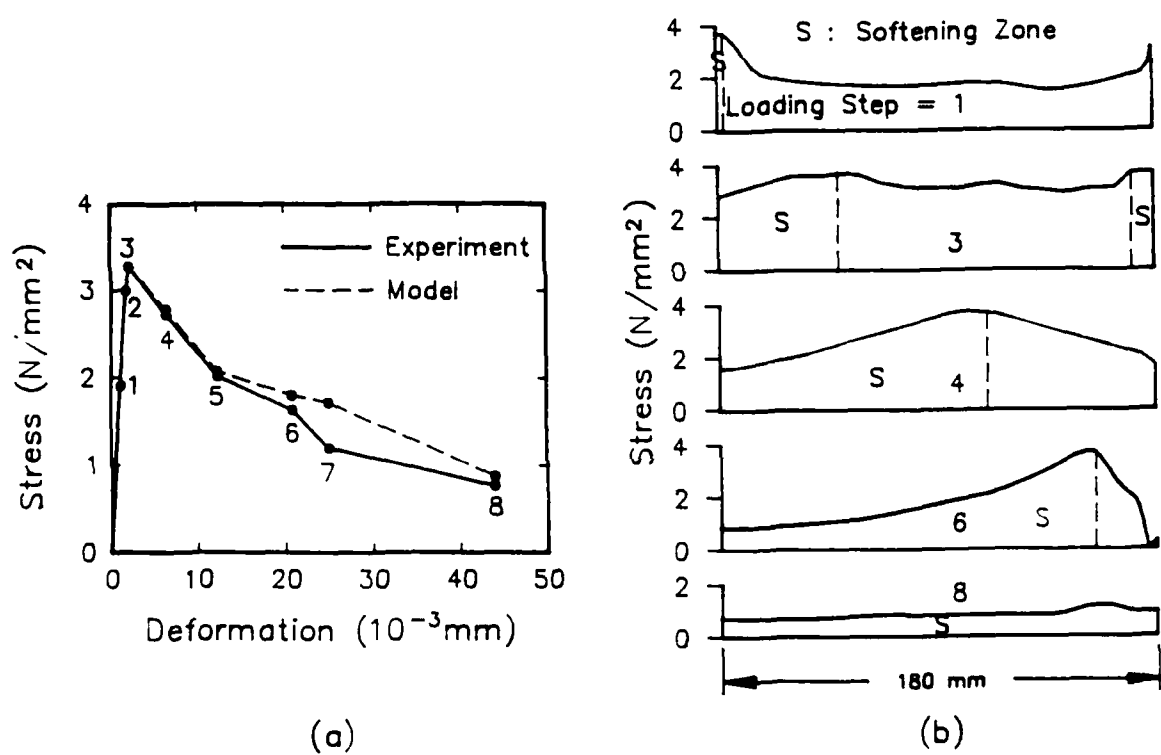


Figure 2.4: (a) Stress-Deformation Relation and (b) Calculated Stress Distribution under Tensile Loading [28].

measured deformation distributions, the modulus of elasticity determined from equilibrium, and the stress-deformation relations determined from the average non-elastic effects during unloading of the material adjacent to the crack faces. The following conclusions can be drawn from Fig. 2.4: micro-cracking in tension occurs at less than 60 percentage of the peak load; the stress-deformation relation is linear up to 90 percent of the peak load; for post peak loads there is a rapid decrease in stress to about 60 percent of that at the peak load and increasing nonlinear deformation. The average stress at the peak load is about 10 percent less than the maximum stress at the terminus of the strain softening zone.

By using moiré interferometry on a dog bone specimen subject to tensile stress, Cedolin et al. [26] found that concrete fails at a low average strain but that locally high strains exist in the specimen due to a non-uniform strain distribution. A meaningful stress-deformation relation is thus difficult to obtain from a direct tension test since the measured average deformation of the tensile specimen has little physical significance in the presence of the localized fracture zone.

The flexural response of concrete as described by Hillerborg et al. [31] is shown in Fig. 2.5.

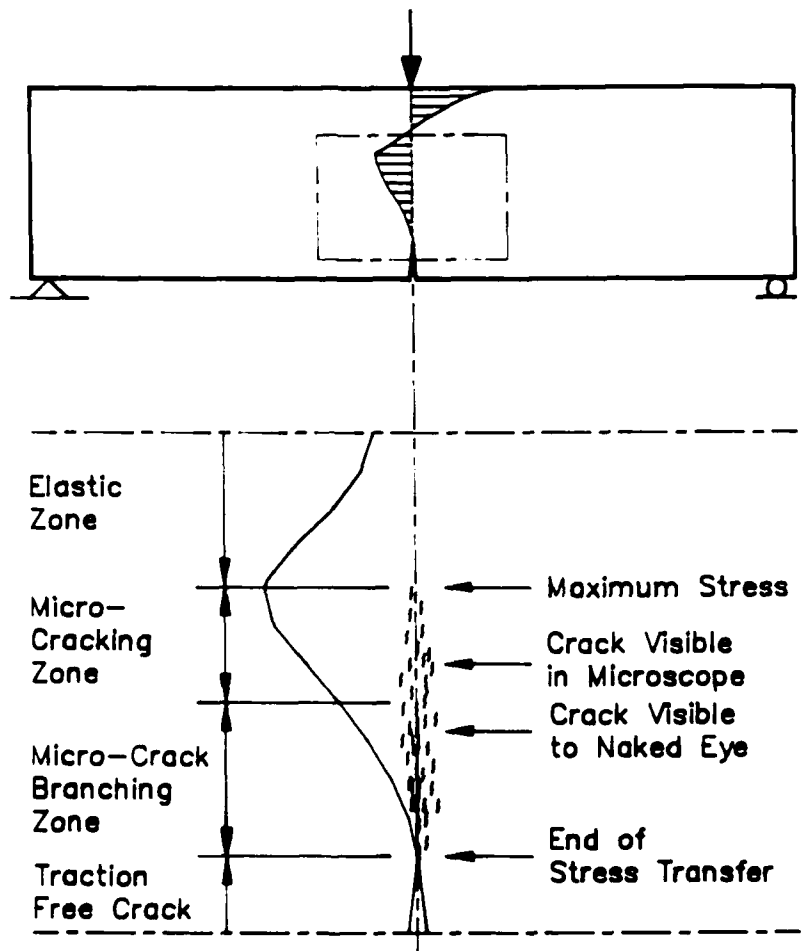


Figure 2.5: Stress Distribution in the Fracture Zone of a Loaded Concrete Beam [31].

## **2.3 Dynamic Fracture Test Methods**

A number of dynamic test methods for determining the dynamic properties of concrete have been proposed but as yet no standard test method has been established. In this section, some of the more important dynamic fracture test methods are briefly reviewed.

### **2.3.1 Drop-Weight Test**

Nanda and Hannant [32] introduced the idea of the "number of blows to no rebound" in order to reduce the subjectivity and arbitrariness in the failure of impacted concrete specimens. This test can be very meaningful when it is used in a comparative way even though the number of blows depend on the drop weight, the drop height, the size of the hammer, its shape and the type of failure. They found that plain concrete failed after 5 blows. The drop-weight test has been recommended by the ACI Committee 544 to evaluate the impact resistance of fiber reinforced concrete [33].

### **2.3.2 Instrumented Drop-Weight Test**

This test is a drop-weight test in which the striking tup and the anvil supports are instrumented to measure load, deflection, strain and energy histories during the impact event. With this data, static analysis is used to compute the basic

material properties, such as ultimate strength and strain at peak load, energy absorbed and fracture toughness at different strain rates.

Suaris and Shah [9,34] proposed this method with a two degree of freedom model for predicting the amplitude and period of inertial loading oscillations for the tup-load versus time trace. Mindess and his co-workers [3,15,35] applied this test method to flexural specimens of hardened cement paste, fiber reinforced concrete and conventionally reinforced concrete.

#### **2.3.3 Charpy Impact Test**

The Charpy impact test is a standard impact test recommended for metals [36]. The impact resistance is measured by the rebound height of the pendulum after impact of a notched beam. The reliability of the method is, however, affected by the stiffness of the pendulum itself in measuring the failure energy and the peak load [37]. Krenchel [38] and Johnston [39] used this method to measure the toughness of fiber reinforced concrete.

#### **2.3.4 Modified Charpy Test**

The modified Charpy test is a Charpy impact test in which the pendulum and the anvil supports are instrumented as in the instrumented drop-weight test. This method was first introduced

by Hibbert [40] who obtained continuous load and energy histories for plain and fiber reinforced concrete beams

Radomski [41] used a rotating impact machine in which the impact load was simulated by releasing a striker from a rotating fly-wheel when it had attained the desired velocity. More recently Shah and his co-workers [42-44] have conducted several series of tests on plain concrete, mortar and fiber reinforced concrete specimens using this method.

### **2.3.5 Split Hopkinson Bar Test**

The specimen in this method is sandwiched between two coaxial elastic bars. Tensile pulses are generated by a weight hitting an anvil fixed at the incident bar. The force acting on the specimen is calculated by measuring the pulse at two points on either side of the specimen and the strain in the specimen can be measured by means of strain gages mounted on the specimen.

Bhargava and Rehnstrom [45] found that the strength of the fiber reinforced concrete was about 50 percent greater than the static tensile strength for an observed pulse rise-time of about 50  $\mu$ sec. Reinhardt and his co-workers [46] developed testing equipment suitable for strain rates between 0.05 and 25/sec. Jawed and his co-workers [47] generated strain rates as high as about 1000/sec and found that at a relatively low strain rate

(less than 250/sec), the ultimate stress increased with increase in strain rate, whereas at high strain rates (greater than 250/sec), it reached a limiting value.

#### **2.3.6 Dynamic Tensile Test**

In this test, typical cylindrical specimens are struck at one end with a high velocity projectiles. The compression wave generated at the striking end is reflected as a tensile wave when it reached the far end of the cylindrical specimen where an impedance matched concrete pellet is placed. The tensile wave causes the concrete to spall. The stresses and strains in concrete are found from the velocity of the pellet. Birkimer and Lindemann [48] conducted tensile tests on steel and nylon fiber reinforced concrete specimens using this method. Recently, Gran and Seam [49] applied this method to plain concrete bars and analyzed the results using a smeared crack-band model.

#### **2.3.7 Explosive Test**

This test consists of applying an explosive shock to a concrete slab. The spall velocity of the fragments is a measure of the impact resistance of the specimen. An improvement in the impact resistance causes a reduction in the spall velocity of the particles as well as their size. This test is ideally suited for situations where a structure would be subjected to rapidly rising pressures resulting from blasts or explosives.

### **2.3.8 Constant Strain Rate Test**

A typical test is carried out at a strain rate that remains constant throughout the whole experiment. Although limited in capacity for achieving high rates of loading, conventional servo-controlled machines have been used to conduct dynamic tests at intermediate strain rates. Kobayashi and Cho [50] used displacement controlled testing of four-point bend specimens to obtain load-deflection curves for polyethylene fiber reinforced concrete beams and observed that the loading velocity affected both the peak load carrying capacity and the corresponding deflection.

## **2.4 Strain Rate Sensitivities of Mechanical Properties of Concrete**

A number of attempts have been made to determine the behavior of concrete under varying strain rates. Most such investigations have shown that concrete is strain rate sensitive. Furthermore, that strain rate sensitivity was found to differ with different test systems. In this section, the strain rate sensitivity of the mechanical properties of concrete under compression, tension and flexure loadings is discussed.

The first experimental study on the strain rate sensitivity of concrete was conducted by Abrams [51] in 1917, who subjected

concrete cylinders to impact compression loading. Green [10] evaluated the performance of concrete for varying strain rates with the independent variables being the cement type, coarse aggregate type and shape, curing conditions, grading and mix proportions, and the specimen age. He found that the higher rate sensitivities the greater the static strength, the angularity of aggregate and the extent of water curing for the specimens.

MacNeely and Lash [52] determined the effect of the loading rate on the flexural strength of concrete and found a linear relationship between the modulus of rupture,  $f_r$ , and the rate of loading,  $\sigma$ ,

$$f_r = A + B \log \sigma \quad (2.1)$$

where A and B are constants.

The compression tests of Atchly and Furr [53] also showed that the compressive strength, absorbed energy, secant modulus and the strain at failure increased with an increase in the strain rate. The compressive strength and the energy absorption reached a constant limiting value at high rates of loading.

Birkimer and Lindemann [48] showed that the critical fracture strain energy theory provides a meaningful fracture criterion and that the critical fracture strain was proportional to the strain rate raised to the one-third power.

Hughes and Gregory [54] developed the load column method in which "low friction" pads was used to reduce the platen friction in dynamic compression tests on concrete prisms. They found a ratio of dynamic to static strength of 1.9. This ratio was independent of the water-cement ratio, age and cement content, but depended upon the type of coarse aggregate.

Hughes and Watson [55] found that the ultimate strains decreased with an increase in the strain rates for concrete cube tests with varying mix proportions and two different types of coarse aggregates under compressive impact loading up to strain rates of 17/sec. This increase was caused by the absence of creep strains at high strain rates. The cause for the large energy requirement in impact tests was that more aggregates failed in high strain rate tests whereas, for low rates, the crack propagated around the aggregate.

Evans [56] suggested the velocity of a growing crack can be described as

$$V \propto K_I^n \text{ or } f'_{td} \propto \sigma^{1/(n+1)} \quad (2.2)$$

where  $V$  is the crack velocity;  $K_I$  is the stress intensity factor;  $f'_{td}$  is the fracture strength,  $\sigma$  is the rate of stress application; and  $n$  is a constant. There are three methods of

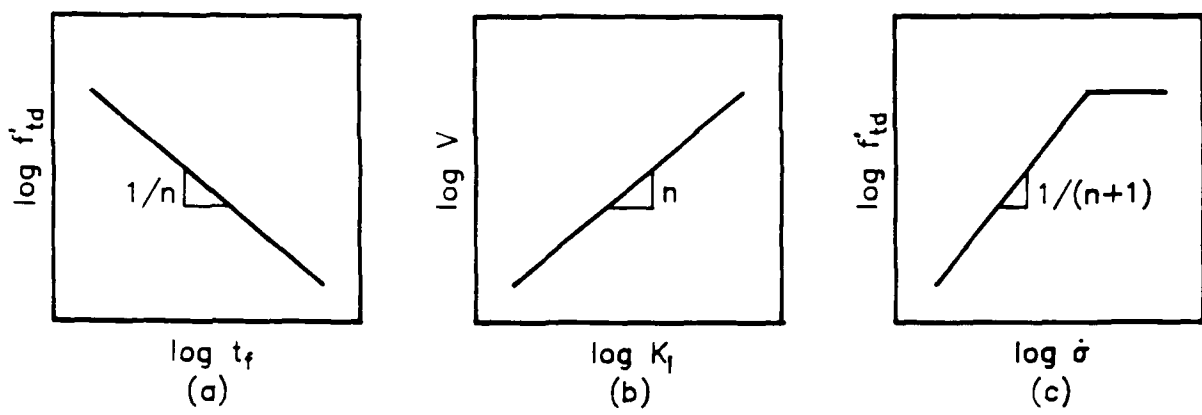


Figure 2.6: Determinations of the Constant "n" [57]

evaluating the value of "n" in Equation (2.2). Figure 2.6 (a) represents results from constant load tests with the applied load causing failure,  $f't_{fd}$ , plotted against the time to failure,  $t_f$ . The slope of that relationship is  $1/n$ . Figure 2.6 (b) corresponds to a plot of the velocity of the growing crack versus  $K_I$  and Figure 2.6 (c) is the outcome for a constant rate of loading test.

Mindess and Nadeau [57] compared the slope,  $n$ , of the  $\log V$  versus  $\log K_I$  plot with the slope of the  $\log f't_{fd}$  versus  $\log \delta$  plot for results from controlled crack growth tests on double torsion specimens, where  $\delta$  is the displacement rate. The value of "n" was almost constant in the case of mortar but differed by a factor of two for cement paste. "n" was also larger for compression tests than for tension and flexural tests.

Mihashi and Izumi [58] developed a theoretical approach to describe the strain rate results satisfactorily as follows:

$$\frac{f_d}{f_s} = \left( \frac{\sigma_d}{\sigma_s} \right)^{\frac{1}{1+\beta}} \quad (2.3)$$

where  $f_d$  and  $f_s$  are the dynamic and static strengths, respectively;  $\sigma_d$  and  $\sigma_s$  are the dynamic and the static stress rates, respectively; and  $\beta$  is a material parameter. The parameter,  $\beta$ , increased with increased strength of concrete.

Thus stronger concrete was less strain rate sensitive than weaker concrete.

Zech and Wittmann [59] generated strain rates of about 2/sec by allowing a missile to fall on mortar flexural specimens and found the distribution function for the flexural strength of the mortar for varying strain rates. The variability of the parameter,  $\beta$ , in Equation (2.3) was not influenced by the rate of loading.

Suaris and Shah [9] used instrumented variable strain rate tests of mortar and found that specimens of higher flexural strength were less strain rate sensitive than those of lower strength. Tensile response was the most strain rate sensitive, compressive response was the least strain rate sensitive, and that flexural response lay somewhere between those two. The constant "n" in Equation (2.2) was not a constant; rather, it decreased with increasing strain rate. Shah and John [60] also point out that the  $\log K_I$  versus  $\log V$  relationship was non-linear especially at high rates of loading

Zielinski and Reinhardt [61,62] investigated the tensile stress-strain behavior of mortar and concrete at high stress rates using the split Hopkinson bar technique. The tensile strength at the high stress rates was found to increase markedly and they concluded that behavior was due to extensive micro-

cracking throughout the whole volume of the stressed specimen. This argument was supported by their observation of higher ultimate strains at higher stress rates and more than one fracture surface along the length of their specimens. The difference between the impact strength of concrete and mortar was attributed to the crack arresting mechanism of the aggregate. For very rapid loading, cracks were forced to develop along the shorter paths of higher resistance, through stronger matrix zones and also through some aggregates because much energy was introduced into the system.

Figure 2.7 shows the influence of stress and strain rates on the tensile properties of concrete such as tensile strength,  $f_{td}/f_{ts}$ , modulus of elasticity,  $E_d/E_s$ , and strain at the maximum stress,  $\epsilon_{ud}/\epsilon_{us}$ , as recommended by Reinhardt [63]. The power  $\alpha$  of the line of tensile strength increase depends on the concrete grade as follows:

$$\frac{1}{\alpha} = 10 + \frac{f_{cm}}{2} \quad (2.4)$$

with  $f_{cm}$  the mean static cube strength in  $N/mm^2$ . The power law becomes

$$\frac{f_{td}}{f_{ts}} = \left( \frac{\sigma}{\sigma_0} \right)^\alpha \quad (2.5)$$

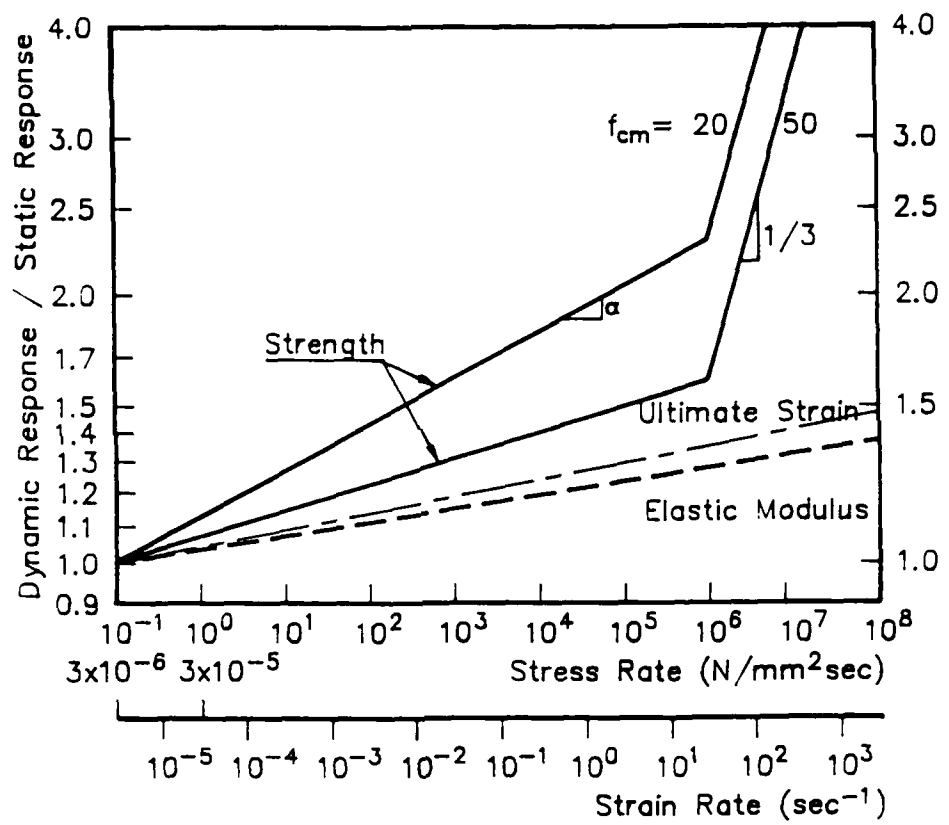


Figure 2.7: Stress and Strain Rate Influence on Tensile Properties of Concrete [63].

where  $\sigma_0$  is the stress rate for static loading with a value of 0.1 N/mm<sup>2</sup>sec. The power of the modulus of elasticity line is 0.016 and that of the ultimate strain line is 0.020.

Malvern and his co-workers [64] generated strain rates of 50 to 800/sec using a large Kolsky bar test system. An apparent rate dependence up to almost twice the static strength was observed. High-strength concrete showed an approximately logarithmic dependence on the strain rate at the maximum stress while mortar showed an apparent linear dependence.

## CHAPTER 3

### EXPERIMENTAL AND ANALYTICAL PROCEDURES

#### **3.1 Displacement Controlled Dynamic Fracture Test System**

A dynamic fracture testing system, which consisted of a high speed displacement-controlled loading system, measurement system and data acquisition system, was constructed for this research project. The displacement-controlled dynamic load was generated by an MTS closed-loop dynamic testing machine. Figure 3.1 shows the MTS equipment used in the loading system and the flow of commands for operating the system. The servo-valve command is generated by the programmable digital wave form generator (MicroProfiler) and that command is transmitted to the displacement controller (AC Controller) through the system controller (MicroConsole). The displacement controller generates the inner loop (IL) command to the valve controller. The valve controller and servo-valve linear variable differential transformer (LVDT) form an inner loop to produce an error signal which represents the difference between the desired and actual transducer output. The error signal is conditioned to produce a valve command which controls the mechanical action of the actuator. The programmed command of the function generator is also used as the triggering signal for the data acquisition system. The 340 l/min (90 gpm) servo-valve and 380 l/min (100

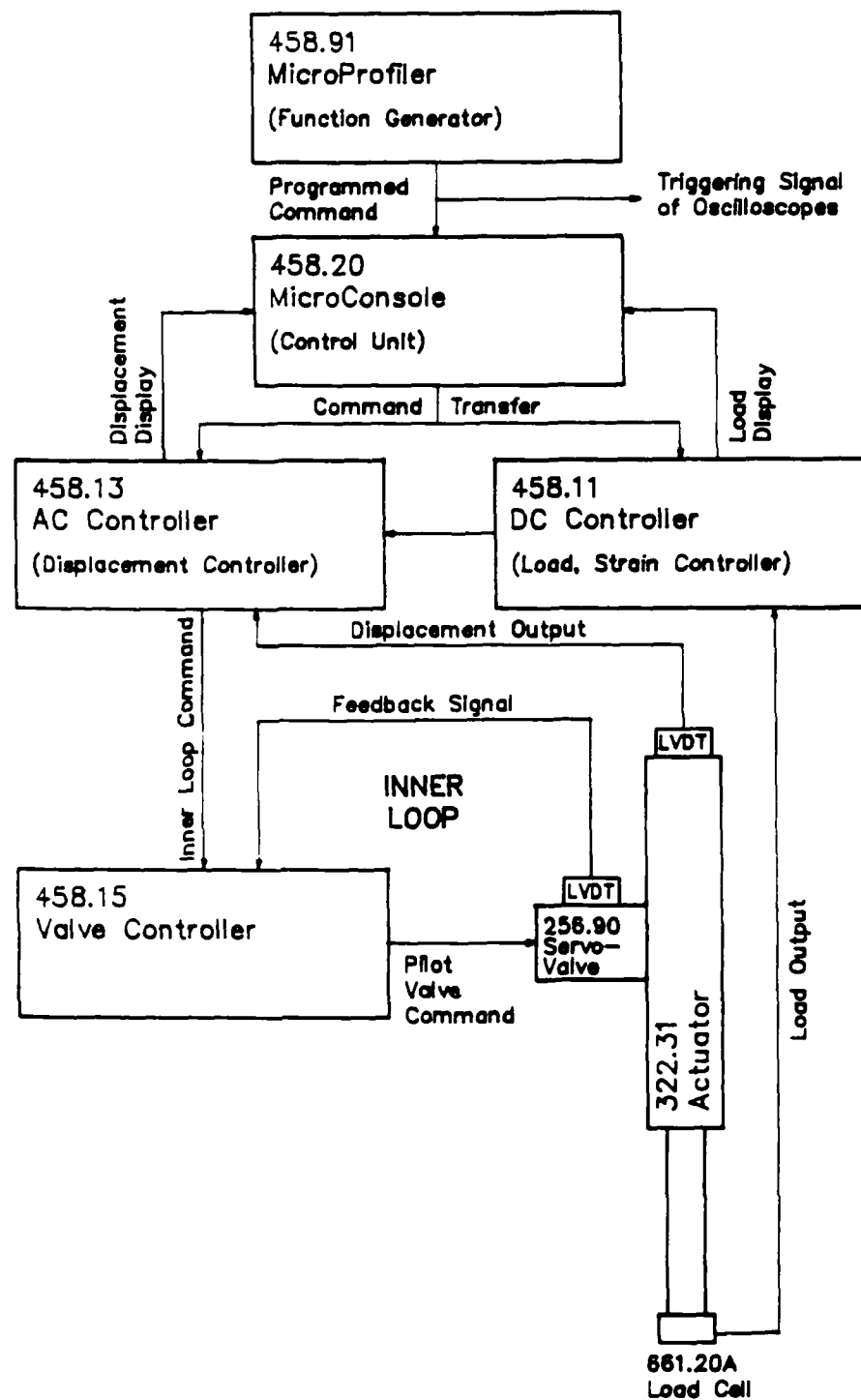


Figure 3.1: MTS Dynamic Loading System

gpm) hydraulic service manifold used in the system can generate a maximum piston velocity of 3.38 m/s (133 in/sec). An 48.9 kN (11 kip) actuator is mounted on the stroke crosshead and the stiffness of the loading system is provided by a 245 kN (55 kip) tee-slotted table and two columns.

The gages and the devices for the measurement system were carefully selected for high speed measurement of 70 KHz resonant frequency. The system, as configured for testing of a three point notched beam specimen, is shown in Figure 3.2. The system consists of: a dynamic load cell and a power unit; three strain gages and a ten-channel strain gage conditioner/amplifier; and two inductive displacement gages and two oscillator/demodulators.

The linear capacity of the dynamic load cell is 22.3 kN (5 kips) and the load cell is designed for fast transient and repetitive applications. It has an inertial mass of 14.2 g (0.5 oz) to minimize its inertial effect. The load cell consists of two thin quartz discs loaded in compression and sandwiched between hardened steel cylindrical members.

The foil strain gages, 5 x 1.5 mm, are located along the crack path to monitor the transient strains associated with a propagating crack. Inductive displacement gages or non-contact capacitance gages of 4.1 mm (0.16 in) maximum capacity are used for transient crack opening displacement measurement.

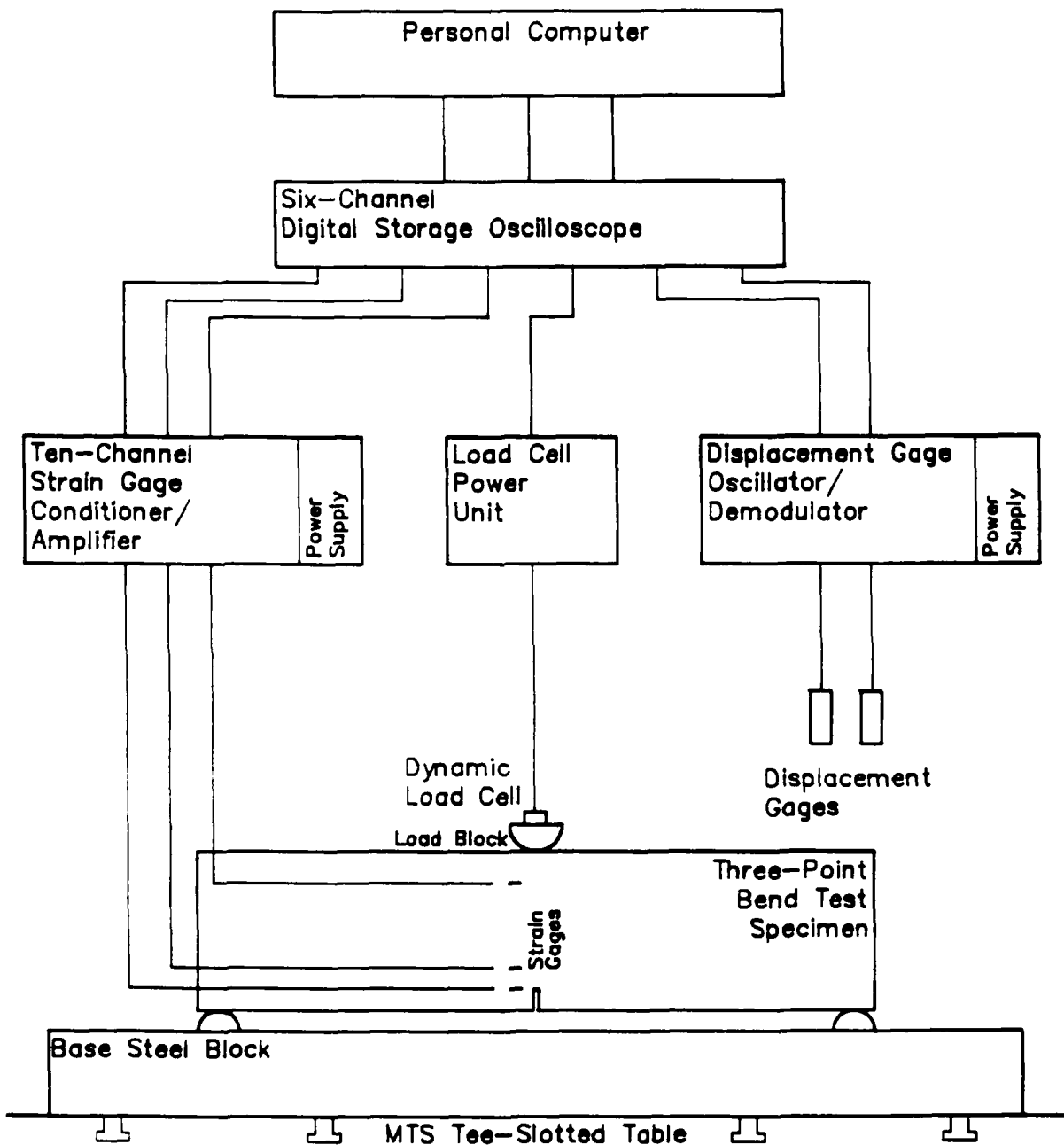


Figure 3.2: Dynamic Measurement System and a Three-Point Bend Specimen

For the data acquisition system, three digital-storage oscilloscopes and a personal computer were used. The data in the oscilloscopes was subsequently transferred to the personal computer for processing, interpretation and permanent storage. Each oscilloscope has two channels with each channel capable of storing up to 1,024 data per sampling within a minimum of 0.001 sec and a maximum of 2 sec.

The configuration of the system for testing of CLWL-DCB specimens is described in Chapter 6. Details of the dynamic loading system and the instrumentation for those tests were the same as described for the three point bend specimens.

### **3.2 Impact Loading Test System**

The strain rates achieved in the displacement controlled three point beam tests did not reach the maximum values desired for this research. Further, the numerical analyses indicated relative energy contribution (Fig. 4.10) significantly different from this typically associated with impact loading results (Fig. 5.10). Accordingly, an impact loading test set-up was also developed in an environment where moire interferometry could also be used to measure crack opening displacements.

A special testing machine was constructed in the optics laboratory of the Department of Mechanical Engineering for the impact loading and moire interferometry studies. The impactor

weighed 98.8 N (22.2 lb) and the maximum height of drop was 1.0 m (39.4 in). The impactor was dropped from a height of 0.4 m (15.7 in). In the same manner as in the displacement controlled tests the concrete specimens were instrumented with a load cell at the contact point and three strain gages located at the same points as shown in Fig. 3.2. Figure 3.2(b) is the test set-up for the impact loading three beam tests.

The basic principles of Moire interferometry were described in Chapter Four, Part I of this contract report. A specimen grating of 600 lines/mm and a reference grating of 1200 lines/mm were used for moire interferometry. The specimen grating was illuminated by an argon ion laser at an oblique incident angle of about 17° where the first order diffracted light provided a 2X fringe multiplication of the specimen grating and interfered with the reference grating. For dynamic fracture analysis, the transient Moire interferometry fringes were recorded by an IMACON 790 high speed camera and 1/5T plug-in with a framing rate of 100,000 frames per second and an exposure time of 2 microseconds. This camera was specially configured to provide four large frames (323 x 18 mm). The larger frames were necessary to resolve the dense Moire fringes. A high speed electric shutter with an exposure time of 7 milliseconds was inserted into the optical path to shield the image tube of the camera from prolonged exposure to the argon ion laser light source.

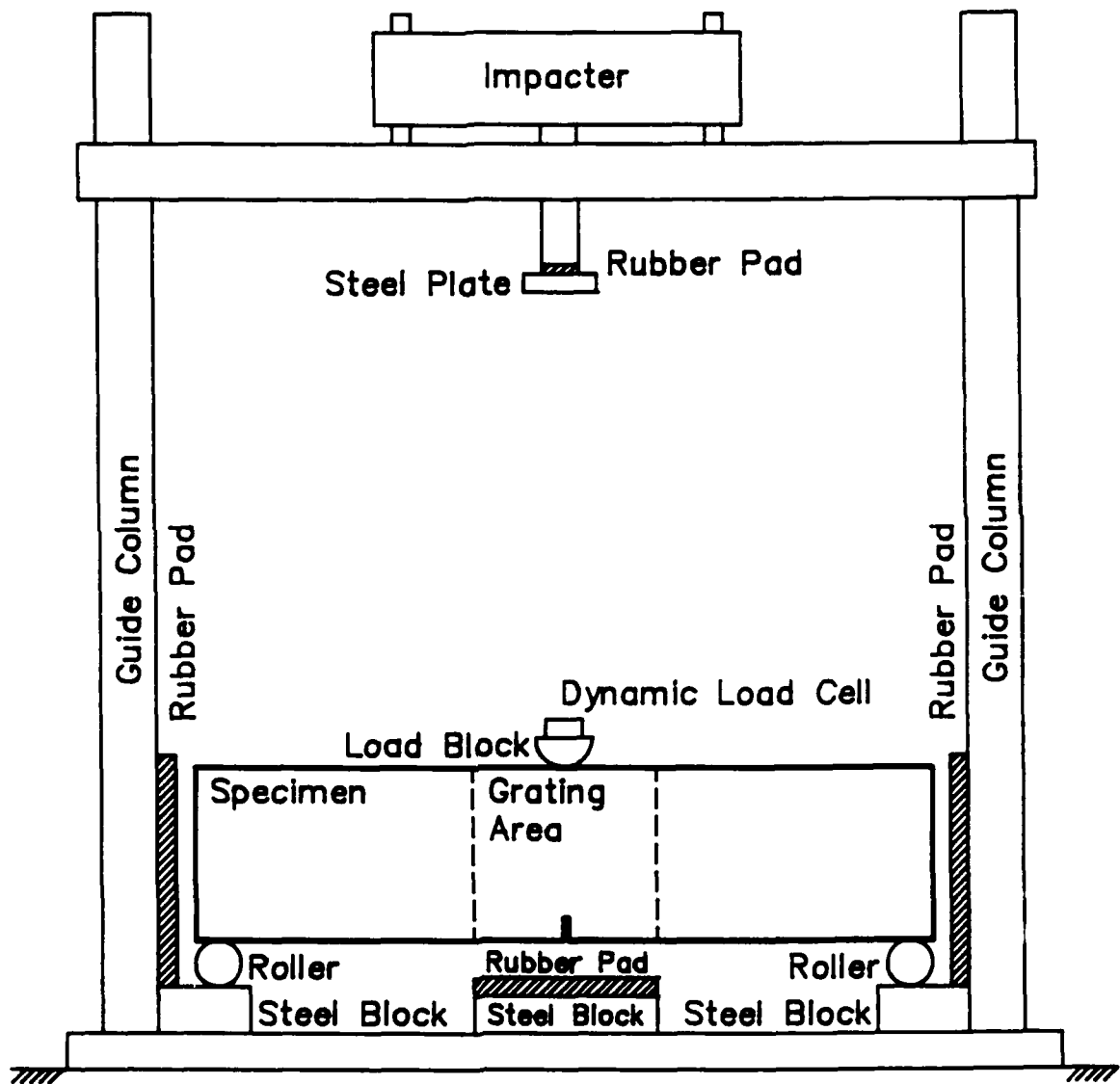


Figure 3.2 (b) : Experimental Set-up for Drop Weight Impact Test System

### **3.3 Experimental Test Program**

The effects of geometry and overall stress state have been investigated by conducting multiple tests on two different type tests of fracture specimens: three-point bend specimens and CLWL-DCB specimens. The same cement, sand, aggregate and aggregate gradation were used for all three point bend and CLWL-DCB specimens so that interpretations of the significance of the results could be concentrated on strain rate and geometrical sensitivity issues rather than material variation issues. Specimens were prepared using the same procedures as those developed for prior static tests [13]. Tables 3.1 and 3.2 show the average gradations for coarse and fine aggregates, respectively. The cement was a type III, high early strength Portland cement, and the sand and the gravel were obtained locally. The same mix proportions were used for all specimens and those proportions are shown in Table 3.3.

Table 3.1: Average Gradation of Coarse Aggregate

Sieve Size	1.5"	0.75"	0.375"	0.25"	No. 4	No. 8
%	0	0	0	0	72	100

Table 3.2: Average Gradation of Fine Aggregate

Sieve Size	No. 4	No. 8	No. 16	No. 30	No. 50	No. 100
%	1.50	15.79	28.87	43.88	78.54	97.50

Table 3.3: Concrete Mix Proportion by Weight

Cement	Sand	Gravel	Water
1.0	2.5	2.0	0.4-0.5

The specimens were cast in a horizontal position in oil lubricated steel forms and steel cylinders. For the CLWL-DCB specimens, those forms contained inserts screwed to them to create holes for the split pins and the starter cracks. Each specimen was compacted with a mechanical form vibrator that moves across the top of the specimen. Particular care was taken to avoid segregation of the ingredient materials. Control cylinders were cast with each batch of fracture specimens and

each control cylinder fabricated in three layers and each layer compacted with a one-inch diameter electric immersion vibrator.

All specimens and their companion cylinders were cured in the same manner. Immediately after casting, the specimens and cylinders were covered with polyethylene sheets and stored at room temperature. The forms were stripped at the age of two days; steel inserts carefully removed from the specimens; and then both specimens and cylinders immediately placed in a moist room. Each specimen was removed from the moist room two days before testing. After it had dried for one day, the surface of the specimen was polished and all necessary gages bonded to that surface.

### **3.4        Numerical Analysis**

#### **3.4.1      Dynamic Finite Element Analysis**

The finite element method used in the research was derived from the regular four-node quadrilateral element using the Hermitian interpolation function [65] and two-dimensional element formulations.

For dynamic analysis, Newmark's  $\beta$  method is applied to solve the equation of motion,

$$[K]\{u\} + [M]\{\ddot{u}\} = \{P\}, \quad (3.1)$$

approximated by the finite element model, where  $[K]$  and  $[M]$  are the stiffness and mass matrices, respectively;  $\{u\}$  and  $\{\ddot{u}\}$  are the displacement and acceleration vectors, respectively, of the finite element assemblage; and  $\{P\}$  is the load vector.

By using Newmark's  $\beta$  method as a direct integration method, all solution techniques employed in static analysis can be used. Another advantage of using Newmark's  $\beta$  method as an implicit scheme is its unconditional stability since the implicit scheme computes the displacement vector directly from the equation of motion at the current time step while the explicit scheme evaluates the current displacement vector using the acceleration vector computed at the previous time step.

### 3.4.2 Application of Crack Closure Stress

To simulate the softened stiffness of the fracture process zone, crack closure forces were applied at released nodes. The equivalent nodal force for the crack closure stress corresponding to a given crack opening displacement,  $\omega$ , the crack closure force vector,  $\mathbf{F}_{ccs}$ , of a released crack tip element was calculated as follow:

$$\begin{aligned}\mathbf{F}_{ccs} &= [\mathbf{k}_\omega] \{\omega\} \\ &= \int_{V_1} [\mathbf{B}]^T [\mathbf{C}_\omega] \{\omega\} dV\end{aligned}$$

$$\begin{aligned}
 &= \int_{V_i} [B]^T \{f_{ccs}\} dV \\
 &= t \int_{A_i} [B]^T \{f_{ccs}\} dA
 \end{aligned} \tag{3.2}$$

where  $[k_{\omega}]$  is the element stiffness matrix for the crack opening displacement;  $V_i$ ,  $A_i$  and  $t$  are the volume, area and thickness of the released element  $i$ ; and  $[B]$  is the strain-displacement matrix of the released element. The nodal stress vector,  $\{f_{ccs}\}$ , is calculated from the assumed constitutive relation,  $[C_{\omega}]$ , between the crack closure stress and crack opening displacement. The direction of the crack closure force vector is opposite to that of the crack opening displacement.

### 3.4.3 Modelling of Continuous Crack Propagation

Crack propagation is simulated by releasing constrained nodes. For a large crack extension in a short time step, this procedure releases a large unbalanced potential energy.

This discrete change is moderated by a gradual movement of the physical crack tip in element,  $i$ , as shown in Figure 3.3. Here the distance of the physical crack tip is assumed to be linearly dependent on the stress at the mathematical crack tip (node  $j+1$ ) as:

$$\beta = \frac{s}{L_i} = \frac{f_{j+1} - f_0}{f_t - f_0} \tag{3.3}$$

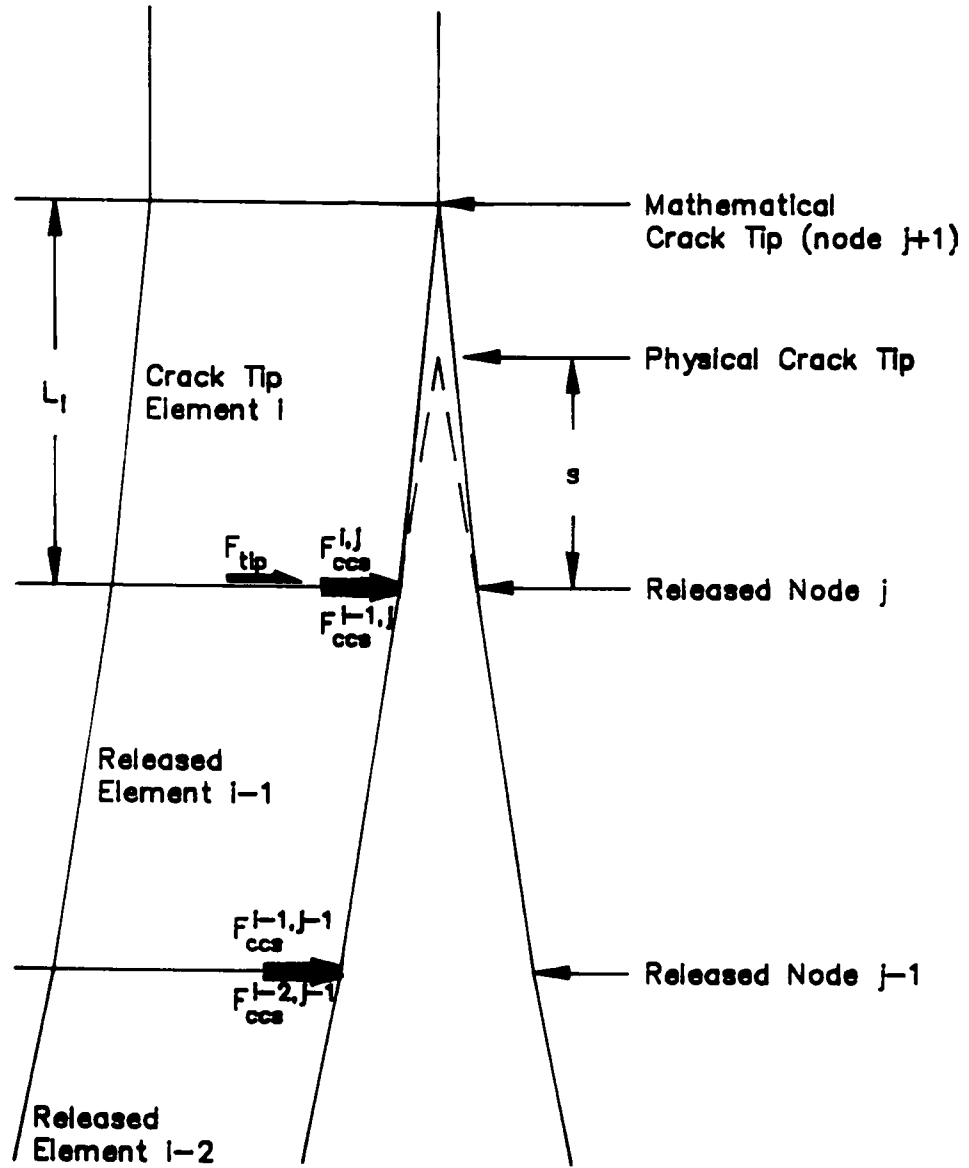


Figure 3.3: Numerical Simulation of Continuous Crack Propagation

where  $\beta$  is the damage rate for the crack tip element  $i$ ;  $s$  is the distance of the physical crack tip from the released node  $j$ ;  $L_i$  is the mesh size of the crack tip element in the crack propagation direction;  $f_t$  is the tensile strength; and  $f_0$  and  $f_{j+1}$  are the stresses at the mathematical crack tip node  $j+1$  when the node  $j$  is released and at the current time, respectively.

To simulate effects for the uncracked portion of the crack tip element  $i$ , a crack tip force,  $F_{tip}$ , is also applied at the released node  $j$  of the crack tip element. That crack tip force is determined from the damage rate  $\beta$  and the response force for the crack tip node  $j$  when that node is released as follows:

$$F_{tip} = \beta F_{tip}^0 \quad (3.4)$$

where  $F_{tip}$  is the crack tip force required to simulate the stiffness of the uncracked portion of the crack tip element  $i$  and  $F_{tip}^0$  is the response force of node  $j$  when that node is released.

For the cracked portion of the crack tip element  $i$ , crack closure force effects are calculated in a similar manner as follows:

$$F_{ccs}^{i,j} = (1-\beta) F_{ccs}^0 \quad (3.5)$$

where  $F_{ccs}^{i,j}$  is the crack closure force for the cracked portion of the crack tip element  $i$  acting on the released crack tip node  $j$  and  $F_{ccs}^0$  is the crack closure force for the crack tip element  $i$  calculated from the crack opening displacement at node  $j$  as described in Section 3.4.2. Therefore the total force applied to the released node  $j$  of the crack tip element  $i$  becomes

$$F_{tip} + F_{ccs}^{i,j} + F_{ccs}^{i-1,j} \quad (3.6)$$

where  $F_{ccs}^{i-1,j}$  is the fraction of the total crack closure force associated with the released element  $i-1$  and acting on the node  $j$  as the result of the crack opening displacement of the node  $j$ .

### **3.4 Determination of Mechanical Properties of Concrete**

The mechanical properties of concrete under dynamic load were investigated using a hybrid experimental-numerical technique. First the elastic properties of the test specimens were determined from the experimental data using the measured responses prior to micro-crack propagation. Then the fracture properties were optimized. Figure 3.4 shows the flow chart of the optimization procedure for determining the elastic and fracture properties.

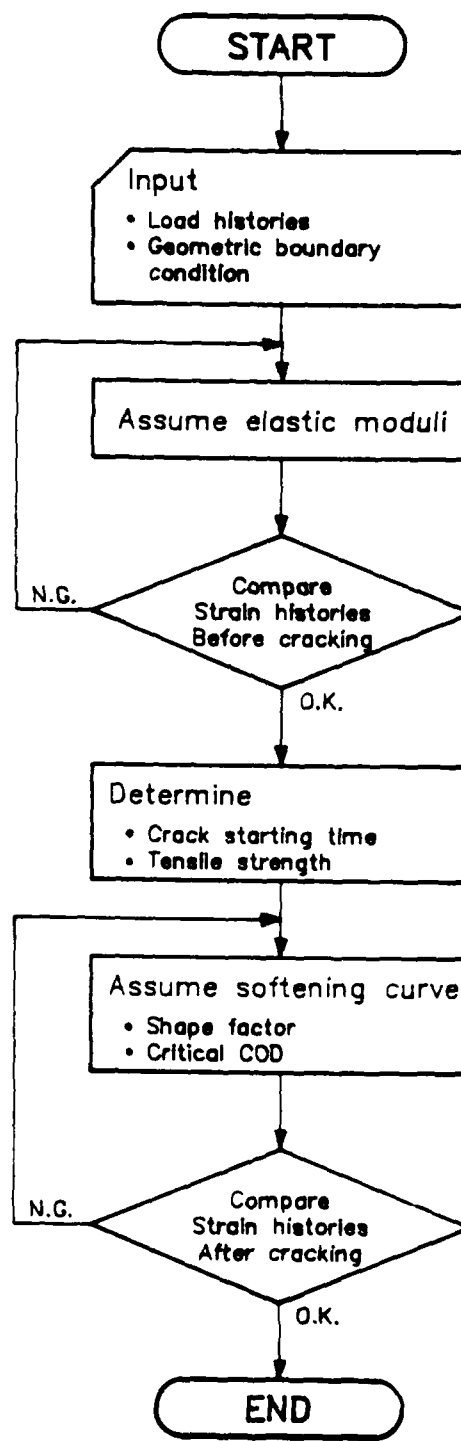


Figure 3.4: Flow Chart for Determination of Mechanical Properties

### **3.4.1 Hybrid Experimental-Numerical Technique**

The hybrid experimental-numerical technique [66, 67] consists of two phase analyses using "generation" and "application" modes. In the generation mode, a characteristic form is assumed for the crack closure stress function and the parameters quantifying that form are determined through a numerical technique using boundary conditions observed experimentally. In the application mode, the numerical technique is used to generate results for an extending crack. Those results are compared with the experimental results. Postulated boundary conditions and constitutive equations are then modified and the procedure repeated until the numerical and experimental results are in agreement with each other.

In this research, the load history was used as an input boundary condition for a two dimensional dynamic finite element analysis and strain histories were generated numerically. Those numerically generated strain histories were then compared with the strain histories measured experimentally to optimize the elastic and fracture constitutive relationships.

This hybrid experimental-numerical method provides reasonable results since it does not require unrealistic assumptions, such as a constant stress state for a direct tensile test or beam theory for a modulus-of-rupture test. Also, the method can accommodate, in theory, variable mechanical properties

throughout the fracture specimen as predicted from available data on the strain rate sensitivities of tension, compression and flexure tests [60,68,69].

### 3.4.2 Elastic Properties

With the hybrid experimental-numerical technique, the mechanical properties required for the concrete can be determined by numerical analysis. The elastic numerical analysis requires the following parameters: moduli of elasticity in tension and compression; and tensile strength or maximum tensile strain.

Moduli of elasticity were determined by matching the initial part of the numerical and experimental strain histories. Since analysis based on strain gage data is very sensitive to the modulus of elasticity, it is necessary to use different moduli of elasticity for tensile and compressive elements, where the tensile and compressive elements are defined from the rate of volume change. Once the moduli of elasticity are determined, the crack-initiation time can be determined as the time when the numerical strain no longer matches the experimental strain. The tensile strength was calculated numerically from the maximum tensile stress at the crack-starting time. Although this tensile strength is dependent on the mesh size, that dependence can be

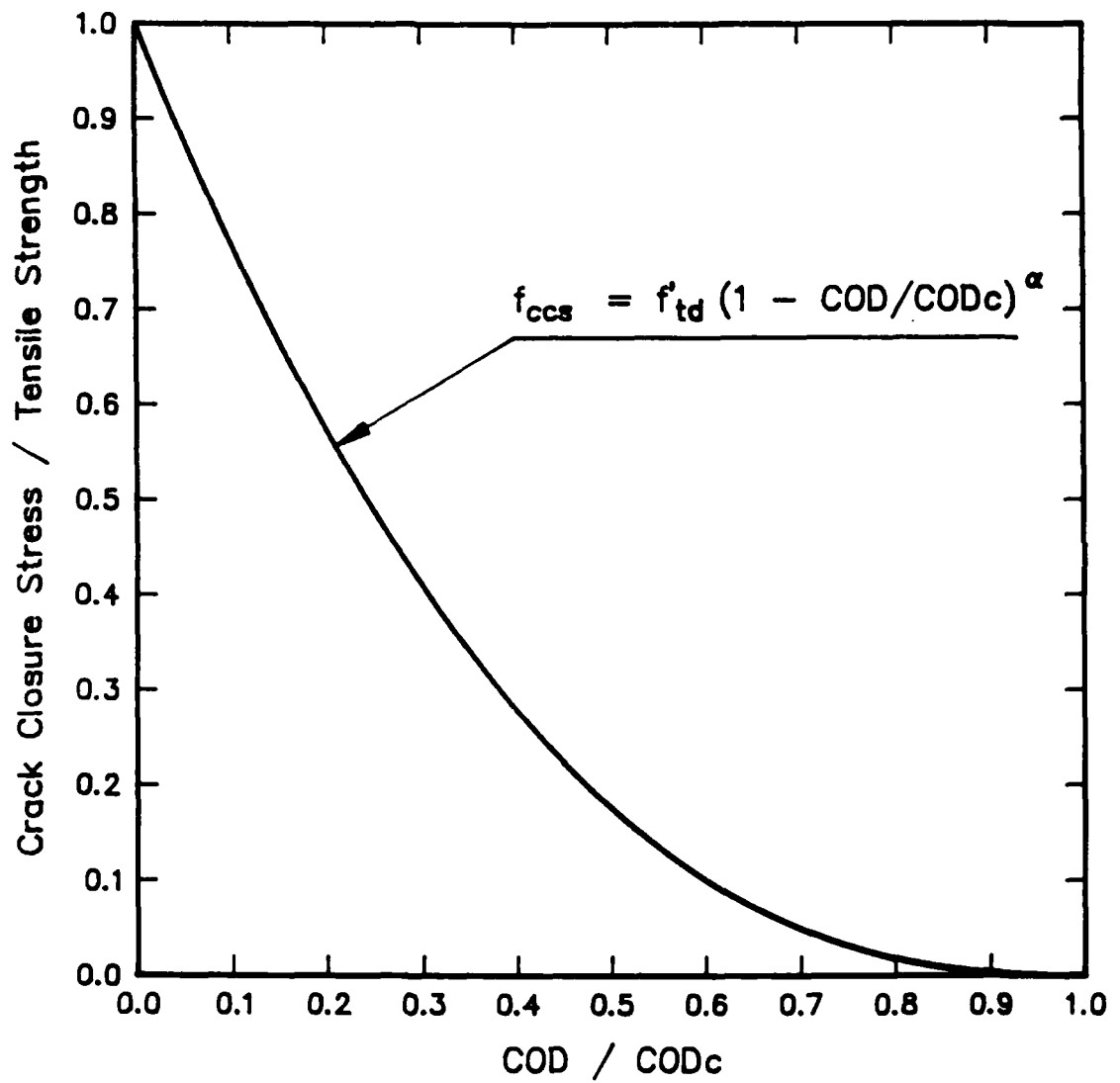


Figure 3.5: FPZ Constitutive Relation

overcome by taking the maximum aggregate size as the mesh size because the experimental value for the strength of concrete also depends on the maximum aggregate size.

### 3.4.3 Fracture Properties

The fracture behavior of the cohesive crack model is specified using a softening curve. The softening curve is described using the following parameters: the tensile strength; the shape factor; and the critical crack opening displacement, as shown in Figure 3.5.

In this research, the softening curve was assumed as

$$f_{ccs} = f_{td} \left(1 - \frac{\omega}{\omega_c}\right)^\alpha \quad (3.7)$$

where  $f_{ccs}$  is the crack closure stress, which represents the remaining stiffness of the fracture process zone;  $f_{td}$  is the dynamic tensile strength;  $\omega$  and  $\omega_c$  are the crack opening displacement (COD) and the critical crack opening displacement ( $COD_c$ ), respectively; and  $\alpha$  is the shape factor. Therefore, the fracture properties are specified with the shape factor,  $\alpha$ , and the  $COD_c$  values. Those two parameters are optimized by comparing the strain histories, which are generated numerically from the experimental load history, with the strain histories observed

experimentally after the crack-starting time. The fracture energy density  $G_F$  of the assumed softening curve is calculated as

$$G_F = \int_0^{\omega_c} f_{ccs} d\omega = \frac{1}{1 + \alpha} f_{td} \omega_c \quad (3.8)$$

It is anticipated that the fracture energy density  $G_F$  is a material property independent of the strain rate and the specimen geometry. For static loading, the fracture energy density,  $G_F$ , and the stiffness in the FPZ were chosen to match those provided by the corresponding three segment model of [68].

## CHAPTER 4

### DISPLACEMENT CONTROLLED THREE-POINT BEND TESTS

#### 4.1 Experimental Set-Up

Three-point bend tests were used in the first phase of this research since such tests are relatively simple to perform and the measured data can be easily interpreted. Figure 4.1 shows the dimensions of the three-point bend specimen used, and the arrangement of gages and fixtures. An initial crack of a 12.7 mm (0.5 in) length and 3.2 mm (0.125 in) width was precast into the specimen using a removable steel plate. That starter crack insured straight crack growth.

An actuator mounted on the crosshead was used to generate external load by vertical motion of its piston as described in Section 3.1. A pre-load of about 22.2 N (5 pounds) was applied for the stable positioning of the specimen, load block and supports. The piston was then accelerated to its programmed velocity and moved at a predetermined constant velocity thereafter until the visible crack tip reached more than 90 percent of the beam depth.

The signal from the function generator that the test was starting triggered the three oscilloscopes allowing the output

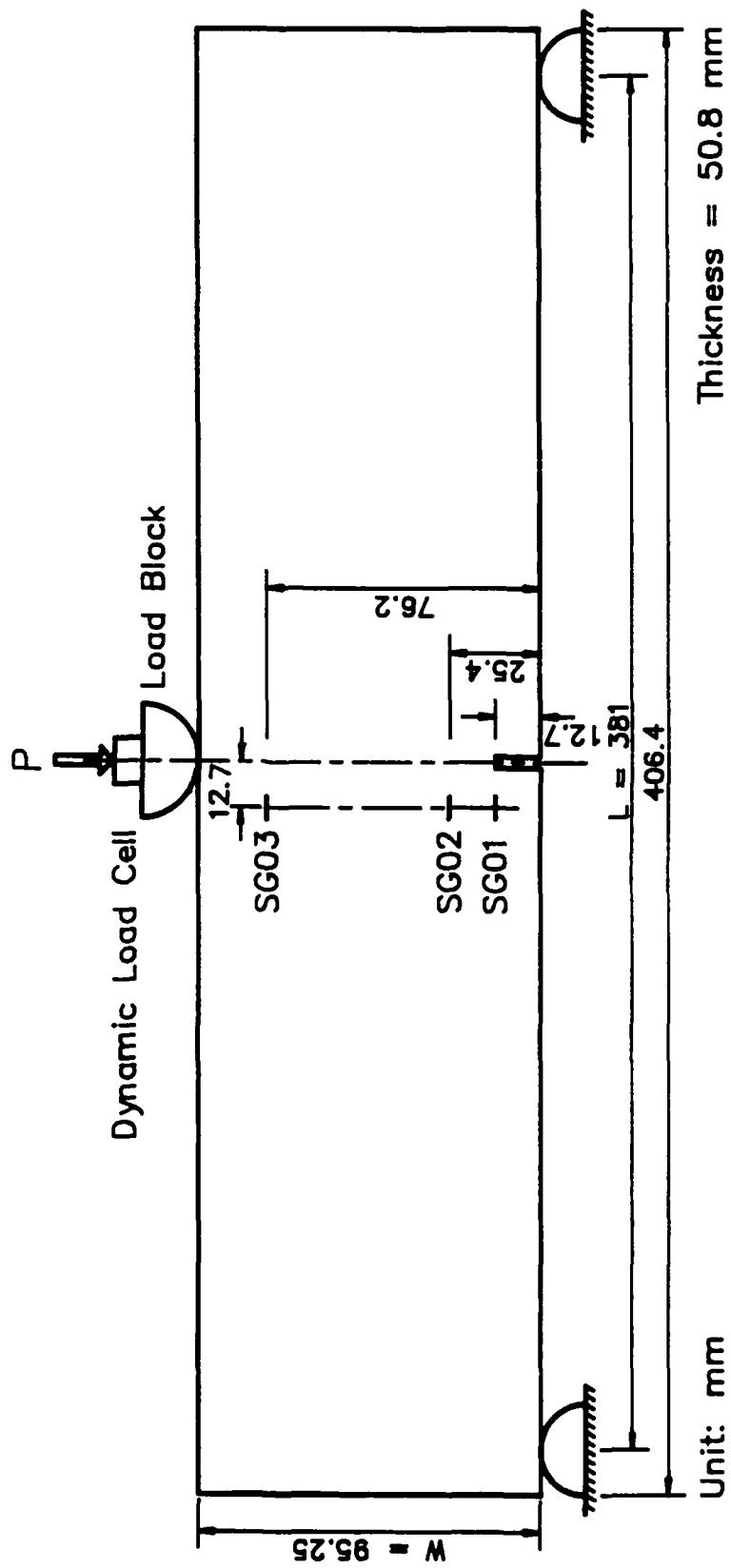


Figure 4.1: Single-Edge Notched Three-Point Bend Specimen

voltages from the six gages to be recorded in the storage of the oscilloscopes. The response load, including the inertial effect of the steel load block, was measured by a dynamic load cell fixed on the top of the load block. Two non-contact capacitance gages, which were mounted on either side of the load block, measure the beam deflection or load-line displacement relative to MTS machine table. Three foil strain gages, 5 x 1.5 mm, were bonded at 12.7 mm (0.5 in) offsets from the center line of the beam. Despite that offset, those gages provided information not only on the strain histories in the fracture process zone (FPZ) but also the time when the micro-crack tip of the FPZ passed those gages. That was possible because the speed at which the unloading compression stress waves from a moving crack tip propagated laterally towards the gage, was very fast compared to the relatively slow velocity of the propagating crack. That crack velocity was less than five percent of the elastic longitudinal wave speed.

From the bend test, five experimental results were obtained: the load history; the load-line displacement history (the average reading of two inductive gages); and the strain histories for three different depths at which gages were attached. Of those results, the load-line displacement history was the least reliable result because values include effects associated with penetration of the load and the supports into the specimen during the test.

#### 4.2 Numerical Analysis

Figure 4.2 shows a typical finite element model used in fitting the data for a three-point bend specimen. The mechanical properties of the specimens were optimized by comparing the strain histories measured experimentally with those generated numerically from the measured load history and the assumed mechanical properties. The validity of the optimized mechanical properties was then verified by comparing the measured load-line displacement history with the numerically generated one.

Initiation of dynamic crack propagation at the precast notch tip was complicated by pre-existing micro-cracks generated by shrinkage stresses. Through a trial-and-error process, this effect was found to be best modelled by reducing the stiffness of the crack tip element and delaying the initiation time of crack extension as that given by the strain history of gage SG01.

The strain rate sensitivity of the dynamic tensile strength,  $f'_{td}$ , was assumed equal to the strain rate sensitivity of the maximum impact load. The maximum static load used to normalize that strain rate sensitivity was the maximum load for the Group 5, tests, which, as apparent from Table 4.1, were the

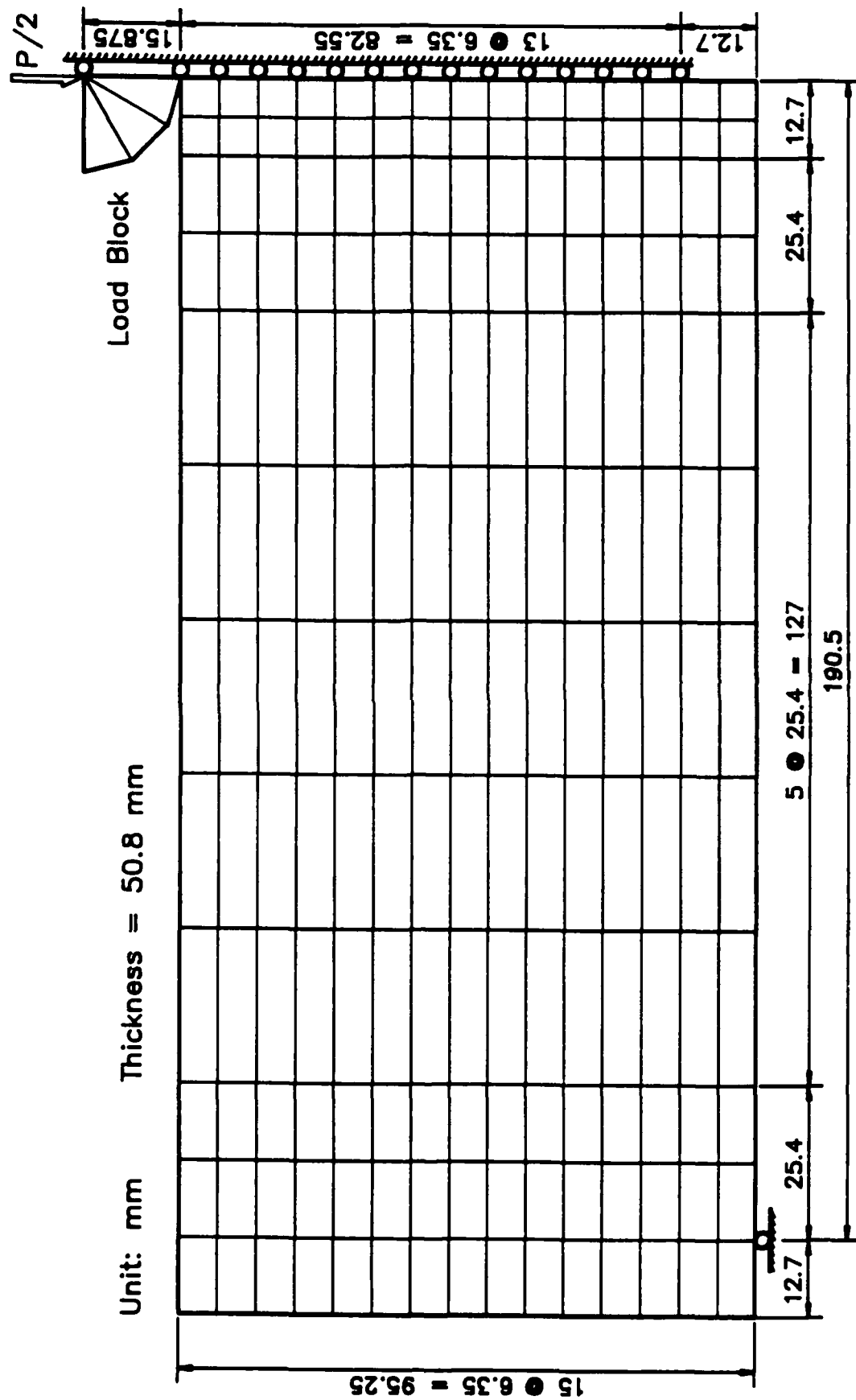


Figure 4.2: Finite Element Model of Single-Edged Notched Three-Point Bend Specimen

slowest loading tests. The fracture properties,  $\alpha$  and  $COD_c$ , as well as the tensile and compressive moduli of elasticity,  $E_{td}$  and  $E_{cd}$ , respectively, were obtained, as described in Chapter 3, via an inverse process in which these properties were optimized to fit the measured strain histories.

As in all inverse procedures, the uniqueness of the constitutive relation for the FPZ and the tensile and compressive moduli of elasticity are not guaranteed. The computed results were assumed correct within the region where the computed strains at the three strain gage locations and the computed load-line displacement agreed with their measured counterparts. Another validation check involved computing the kinetic, strain and fracture energies separately and then comparing the sum of these three quantities with the total input work at each instance of crack extension. The final validation check involved the internal consistency of the computed results and their convergence to their known static counterparts at low strain rates. In spite of the trial-and-error process used in this analysis, these strong correlations between the several different computed and measured data left little reason to suspect that the computed material properties deviated from the corresponding measured results.

### 4.3 Results

#### 4.3.1 Experimental Results

Five groups of specimens, with five identical specimens in each group, were loaded at five different programmed actuator displacement rates which yielded failure times of 2, 5, 25, 100, and 1000 msec. Of the five tests, two test results which best represented the responses of each of those five groups, were used in subsequent numerical analyses. The test conditions for each of these two specimens are listed in Table 4.1.

Table 4.1  
Three-Point Bend Test Data

Group No.	Test No.	P <sub>max</sub> (kN)	Time to P <sub>max</sub> (msec)	SGO1 max.	Strain ( $\mu\epsilon$ ) SGO2 max.	SGO3 min.	Time to Failure (msec) t <sub>F</sub>
1	11	7.34	1.5	43	115	-80	2.0
	12	7.43	1.4	68	144	-93	2.0
2	21	5.56	3.8	47	144	-84	4.6
	22	5.29	3.5	31	123	-64	4.3
3	31	4.25	18.6	40	123	-78	21.9
	32	4.29	18.6	46	102	-71	21.9
4	41	3.88	74.8	36	84	-62	84.0
	42	3.92	71.7	49	101	-67	87.4
5	51	3.41	655	24	87	-74	1000
	52	3.52	601	28	62	-74	1000

Typical load and strain histories for a specimen, Test 11, loaded to failure in 2 msec are shown in Figure 4.3. The time at which the FPZ tip was taken as passing a given gage position, is indicated by a symbol on the response for that gage. The strain peaks for strain gages SGO2 and SGO3 in Figure 4.1, were taken as the time at which the FPZ tip passed those gages. However, such was not the case for the first strain gage, i.e. SGO1 in Figure 4.1, since, as discussed previously, numerical experimentation demonstrated that locked-in shrinkage effects altered the behavior at that location. The first plateau in the SGO1 record indicated that dynamic microcrack tip extension initiated at 1.10 msec and at a stress lower than  $f'_{td}$ . The continued slight rise and the subsequent plateau in the SGO1 strain history represent continuous increase in strain in the crack tip element despite the onset of micro-crack propagation at 1.10 msec. In contrast, the passage of the micro-crack tip past SGO2 and SGO3 is characterized by a precipitous drop in strains. Average crack velocities were 64 m/sec (2,500 in/sec) between strain peaks for SGO1 and SGO2 and 154 m/sec (6,060 in/sec) between strain peaks for SGO2 and SGO3.

Figure 4.4 shows the load and the three strain histories for the specimen, Test 52, loaded to failure in 1000 msec. The average crack velocities were 0.060 m/sec (2.38 in/sec) between the strain peaks for SGO1 and SGO2 and 0.233 m/ssec (9.17 in/sec) between the strain peaks for SGO2 and SGO3.

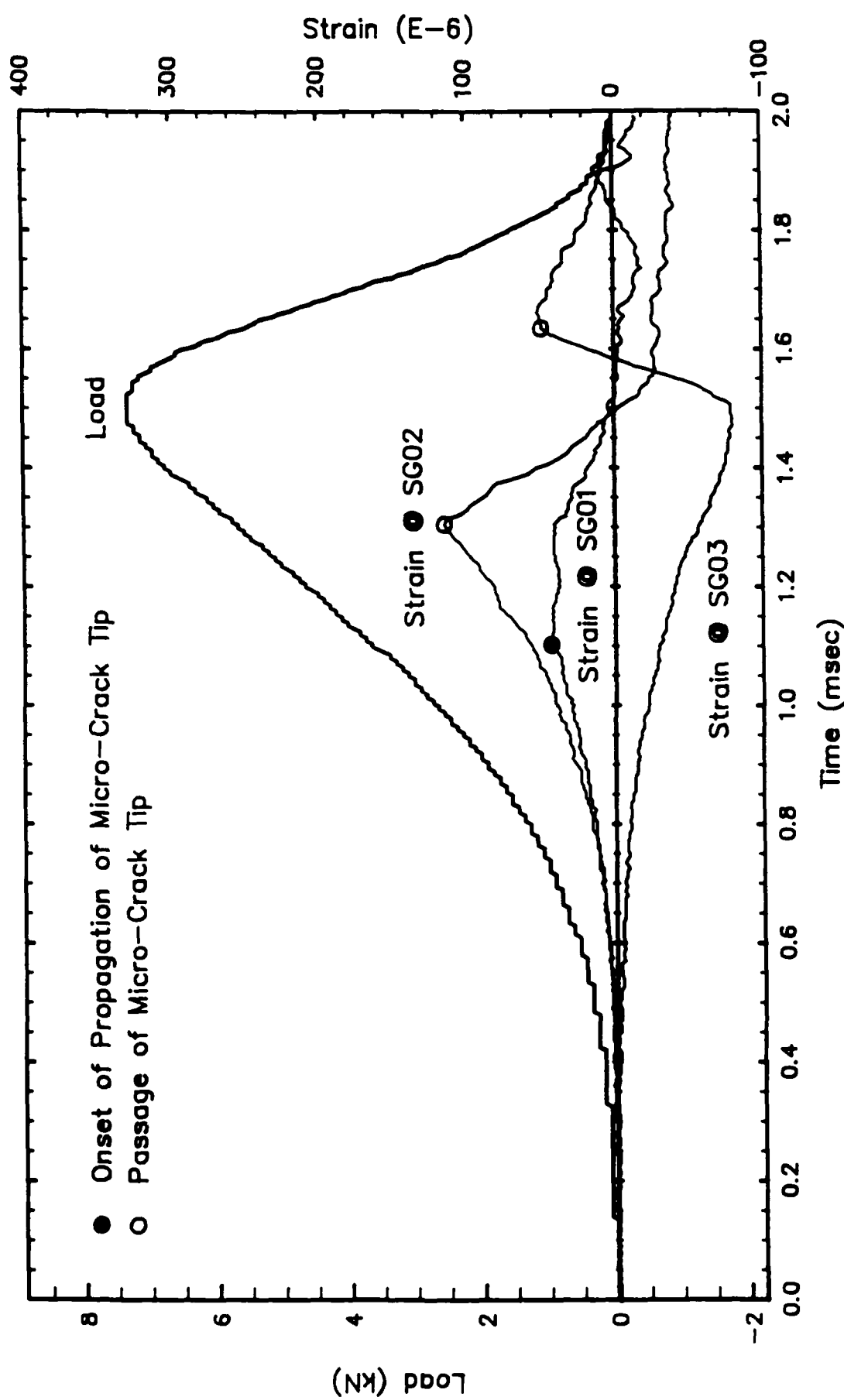


Figure 4.3: Load and Strain Histories of Test 11

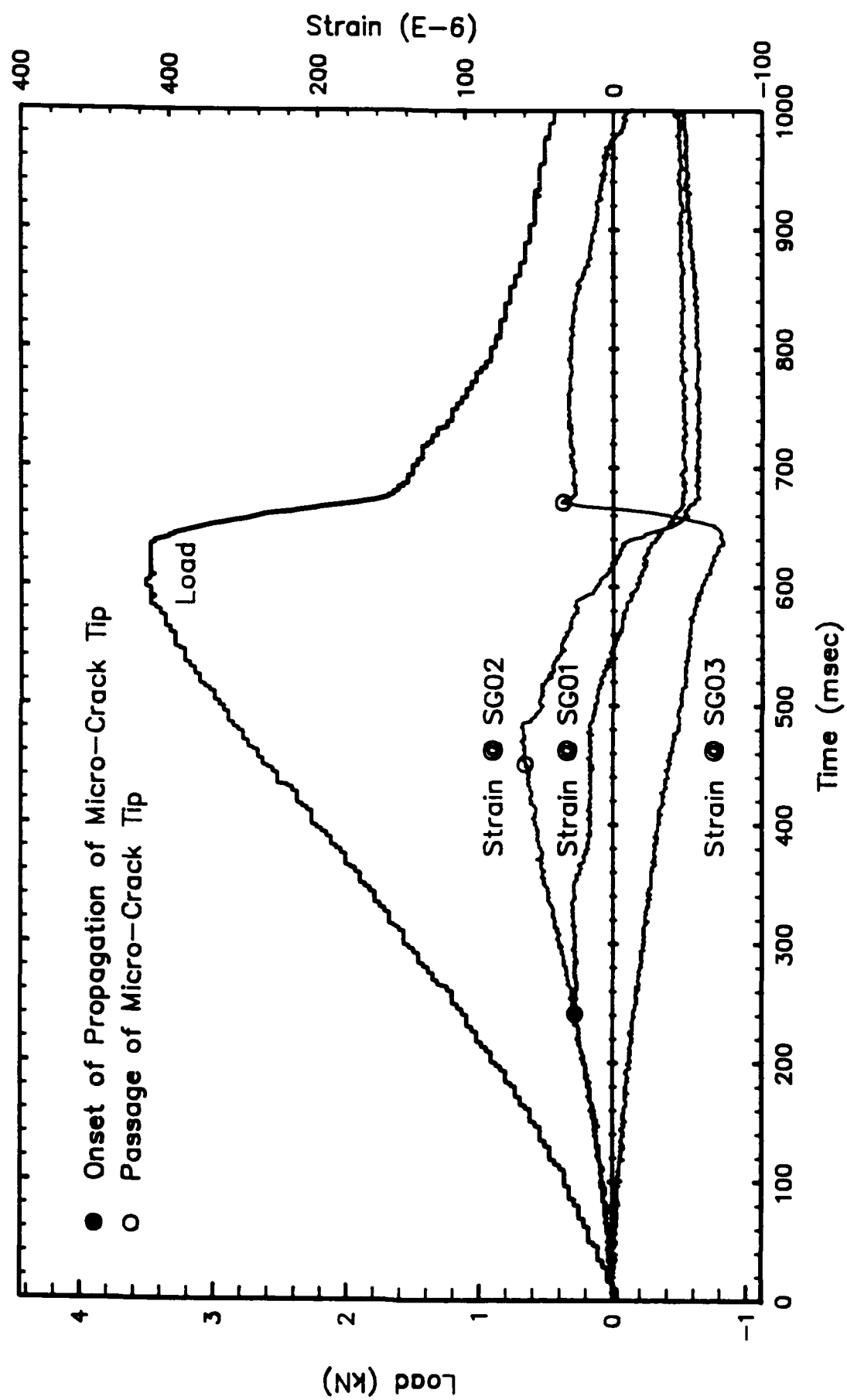


Figure 4.4: Load and Strain Histories of Test 52

Figure 4.5 shows the load versus load-line displacement histories for the five different strain rate loadings. The increase in strength, and to a lesser extent initial stiffness, with increasing strain rate is obvious.

#### 4.3.2 Numerical Results

The experimental results for two tests from each of the five groups of tests were analyzed numerically using the measured loading history and the postulated constitutive relation for the FPZ, i.e. Equation (3.8), as input boundary conditions. This propagation analysis was preceded by an extensive sensitivity analysis of the variables involved in this inverse process. The particular form of the continuous function for the constitutive equation of the FPZ was based on the previously obtained three segment model of the FPZ [68,69]. Use of that static model greatly reduced the amount of trial-and-error analysis involved in matching the computed and measured crack extension and the three strain gage histories.

Figure 4.6 shows the computed crack extension histories for the specimens which were loaded to failure in 4.6 and 84 msec, respectively. The slow crack velocities during the initial phase of dynamic crack propagation represent the influence of the pre-existing damage region, at the precast notch tip, caused by shrinkage effects. The symbols on Fig. 4.6 indicated measured, as opposed to computed results.

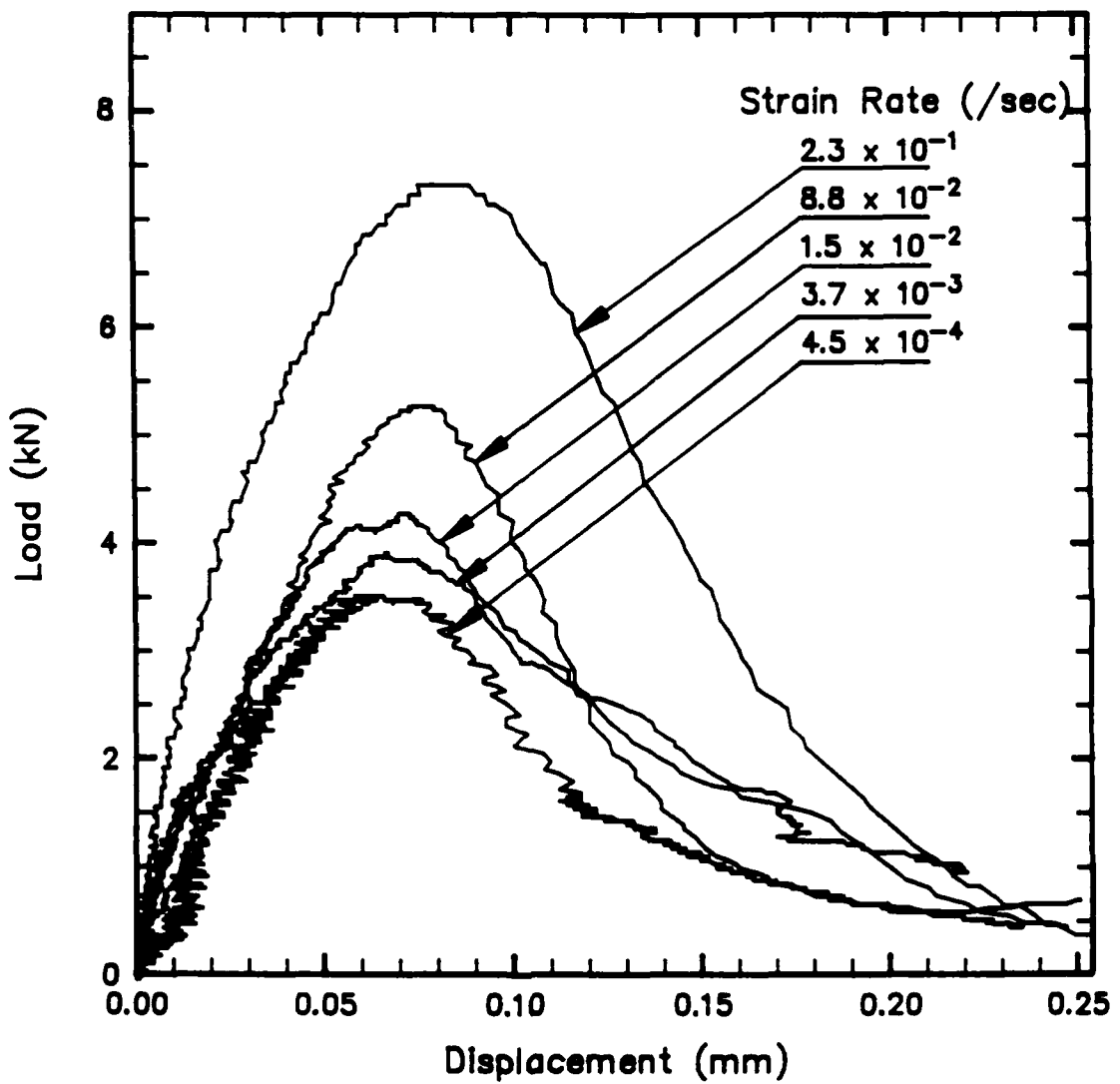


Figure 4.5: Load versus Load-Line Displacement

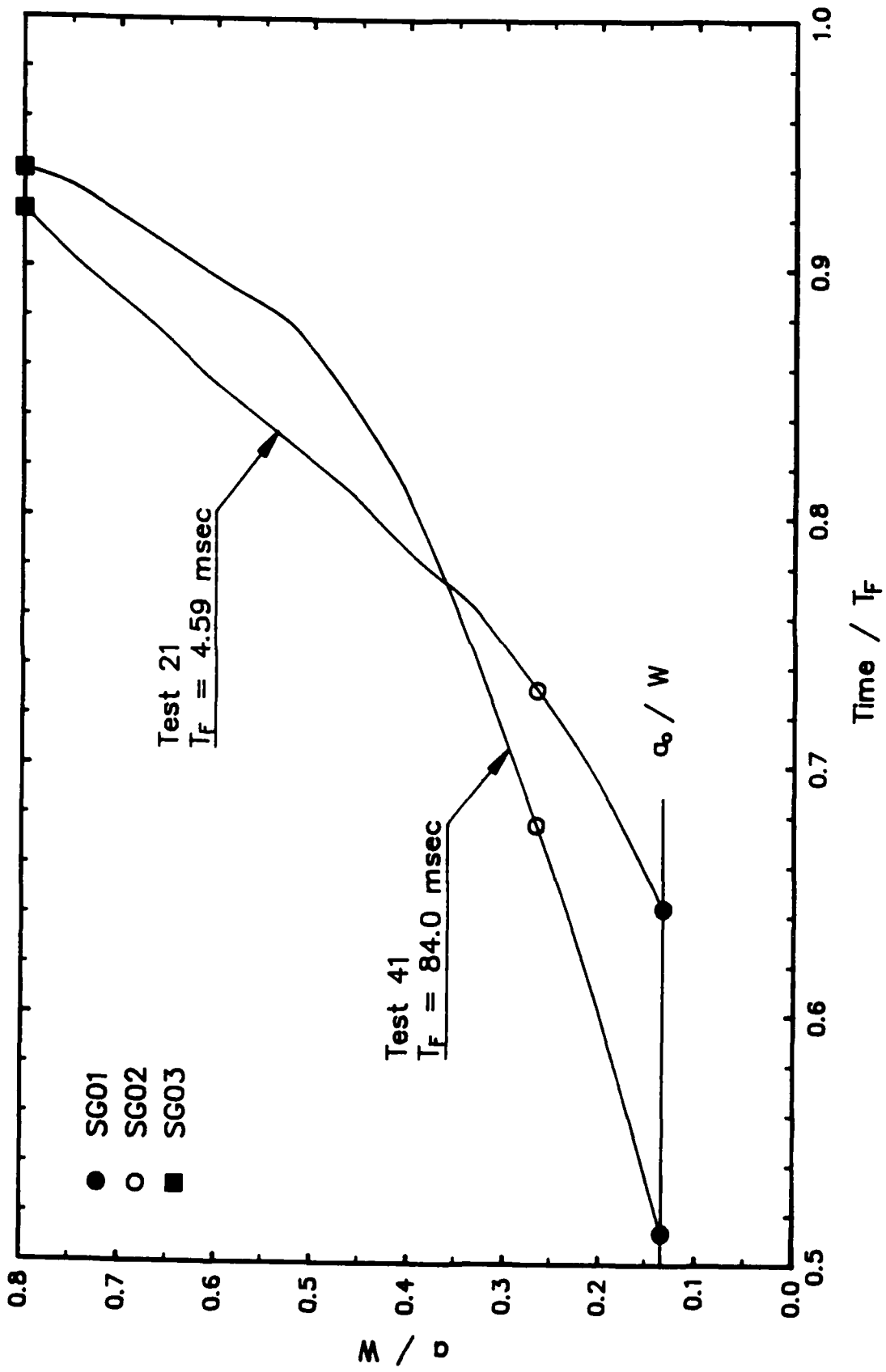


Figure 4.6: Crack Extension Histories of Tests 21 and 41

Figures 4.7 and 4.8 show the measured and computed strain histories at the three strain gage locations for Group 2 and 4 tests. Excellent agreements between the computed and measured strains are noted prior to the arrival of the microcrack tip of the FPZ at the location of SGO2. The subsequent decrease in the measured strains is also modelled relatively well by the numerical simulation.

Figure 4.9 shows the measured and computed load versus displacement relationships for Tests 21 and 41. Excellent agreements between the measured and numerical results are noted. Much of the strain softening portion of the loading history was not simulated in Figure 4.9 due to limits on the amount of available computer time.

Figure 4.10 shows the variations in energy partitions with crack propagation for Tests 21 and 41. The sums of the three energies, i.e. strain, kinetic and fracture energies, were at the worst within 3 percent of the corresponding input work during the dynamic fracture process. It is noteworthy that, unlike similar impacted metallic three-point bend specimens, the kinetic energy is negligible. Because of the lack of substantial kinetic energy, the two broken halves of the bend specimens remained attached under this displacement controlled impact loading condition. The good to excellent agreement between the

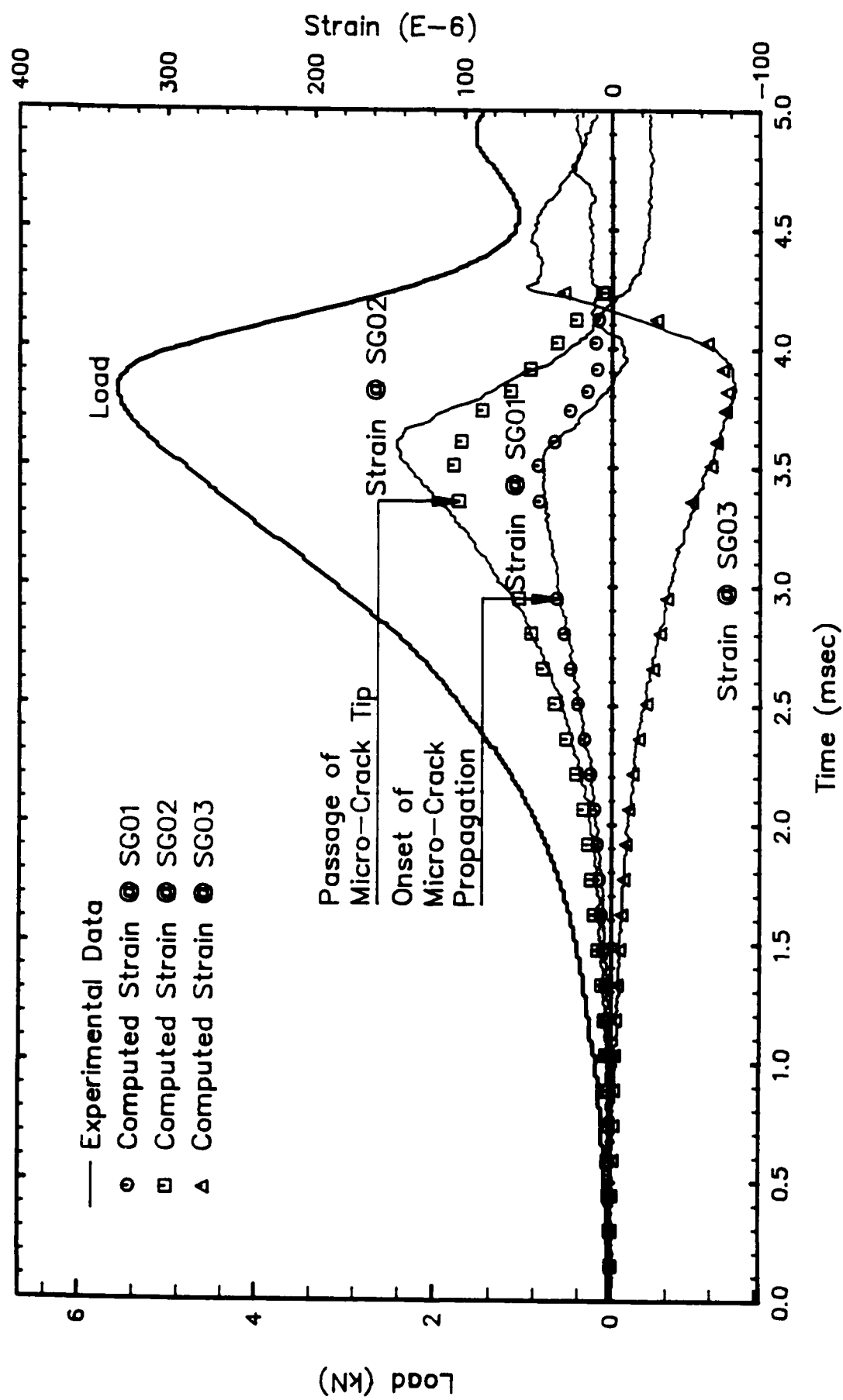


Figure 4.7: Experimental and Computed Strain Histories of Test 21

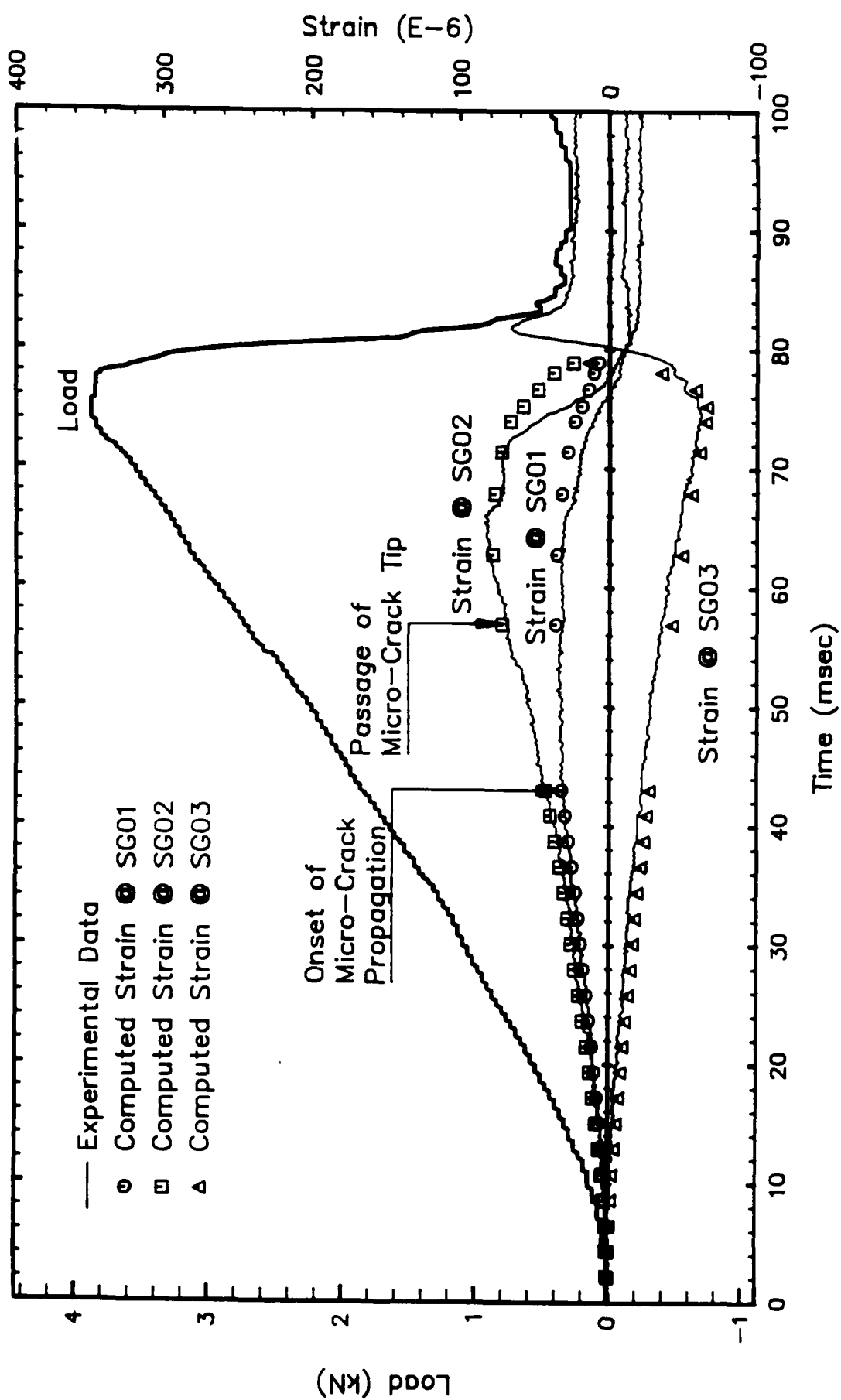


Figure 4.8: Experimental and Computed Strain Histories of Test 41

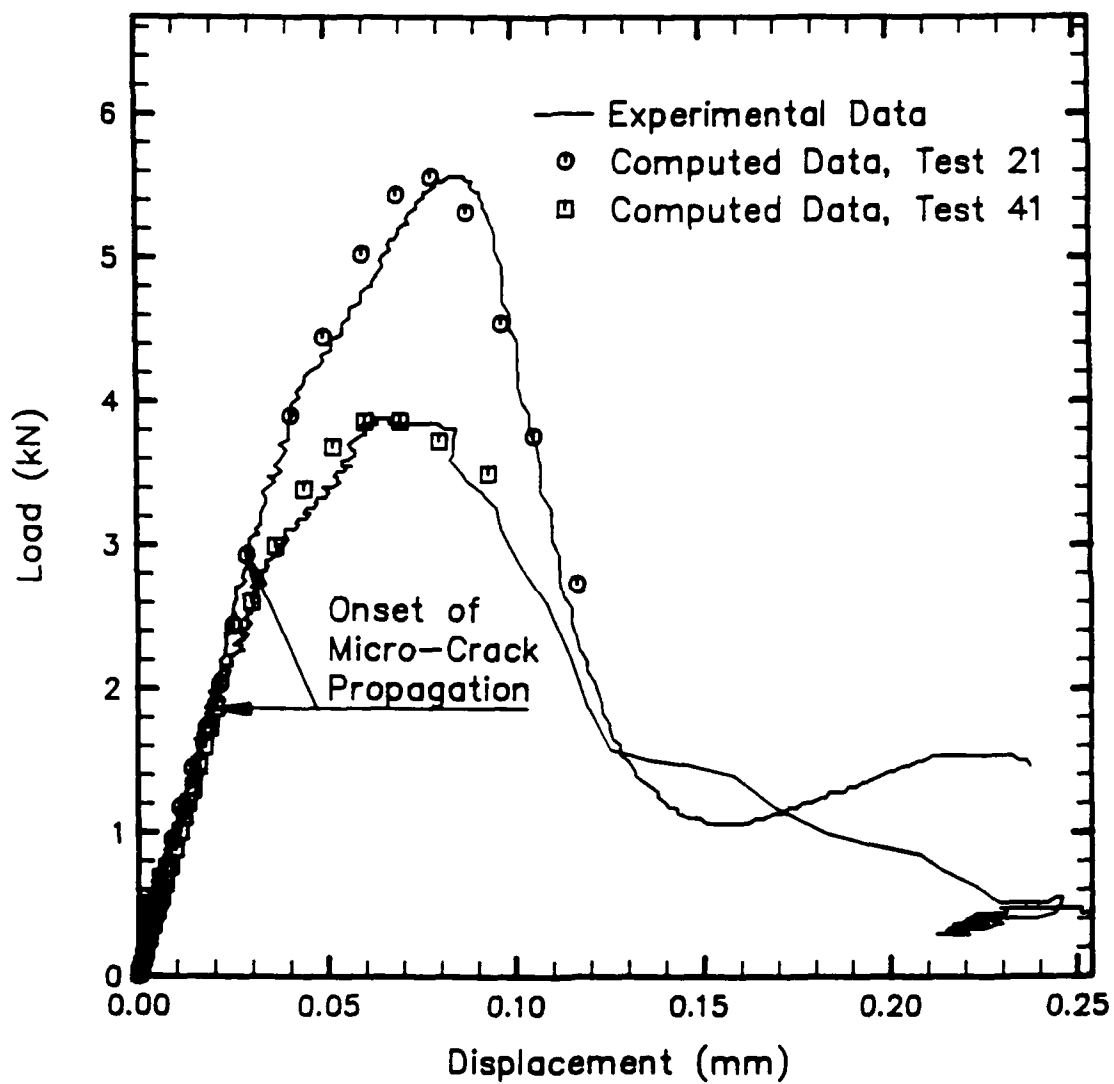


Figure 4.9: Load Displacement versus Load-Line Displacement of Tests 21 and 41

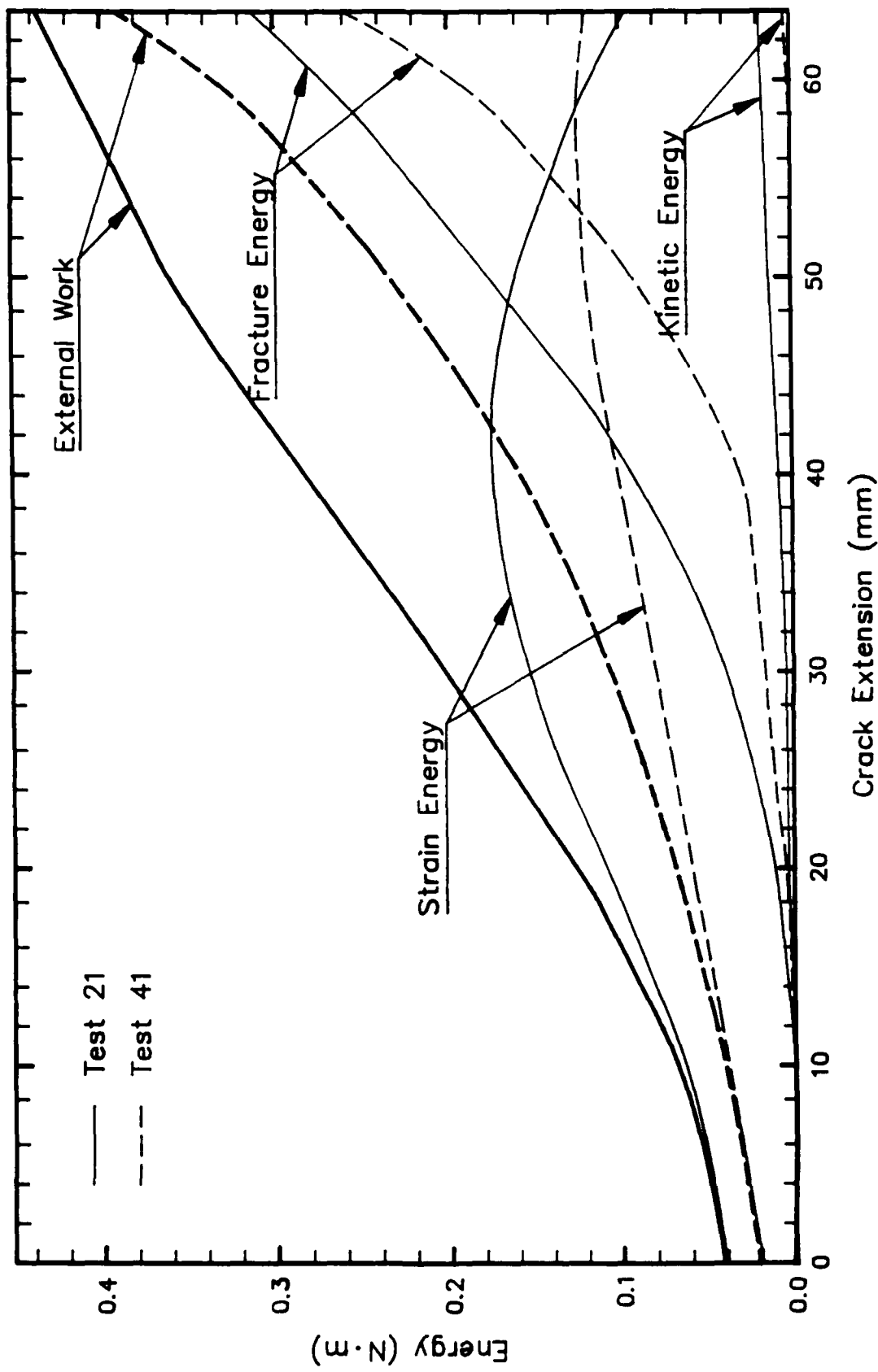


Figure 4.10: Energy Partition, Tests 21 and 41

measured and computed values in the foregoing comparison provides additional verification of the numerical analysis. The final material properties gleamed from the entire numerical analysis, two per group for the five groups, are summarized in the following section.

#### 4.3.3 Strain Rate Sensitivity of Mechanical Properties

The computed strain rate sensitivities of the tensile strength and the tensile and compression moduli of elasticity are shown graphically in Figures 4.11 and 4.12, respectively. Symbols indicate computed results and the bilinear curves represents the best fit to those results. The higher dynamic tensile strength,  $f'_{td}$ , at higher strain rates is consistent with the observed increase in trans-aggregate failures on the fracture surfaces. In contrast, the fracture surfaces of statically loaded specimens exhibited interface failures around the aggregates due to the lower interface strength between the aggregates and the cement matrix.

The two pseudo-static results control the horizontal portions of the bilinear curves and from Figure 4.12  $E_t$  is predicted to be  $0.83 E_c$ . The results for two representative tests from each of the five groups and the associated numerical

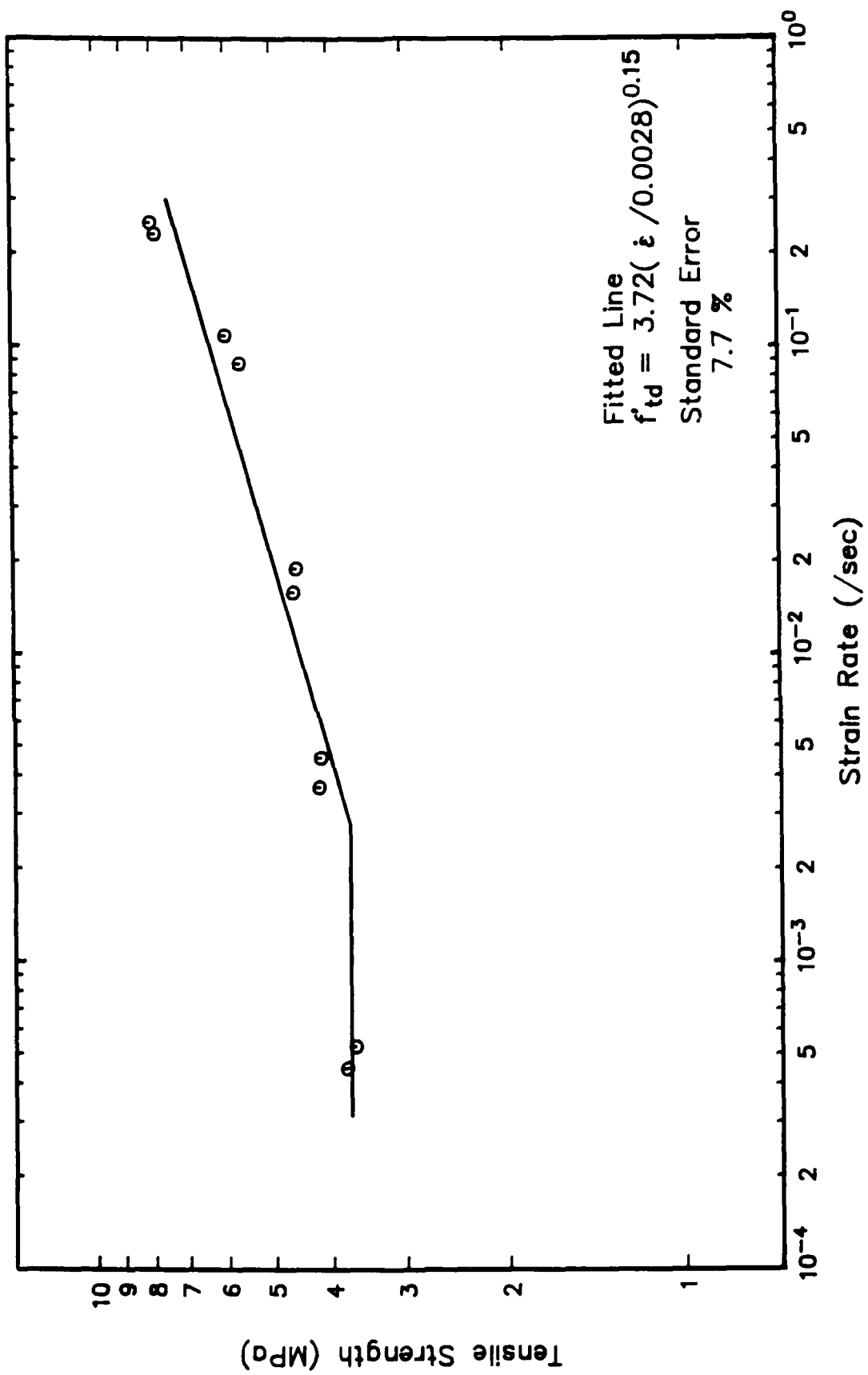


Figure 4.11: Strain Rate Sensitivity of Tensile Strength

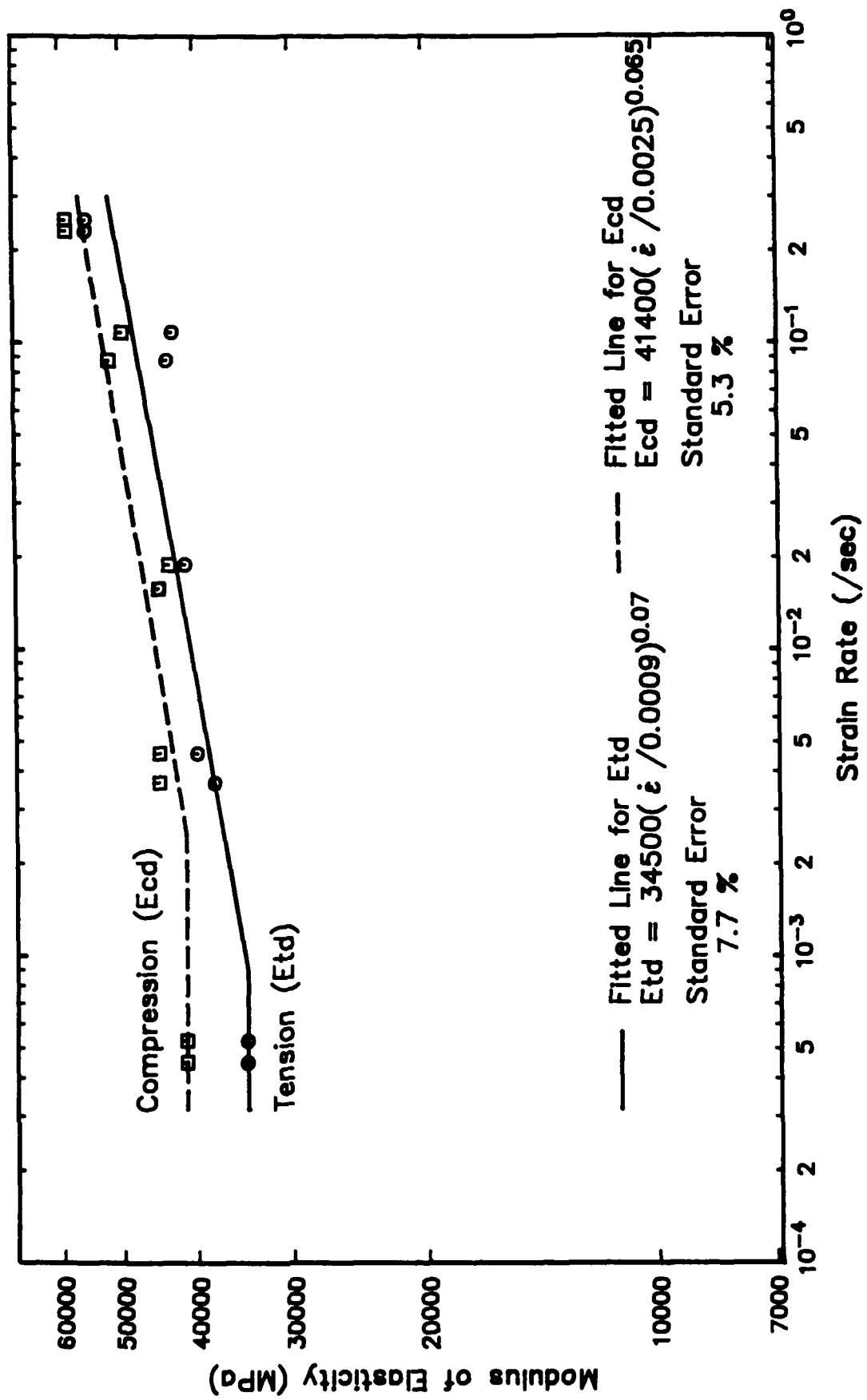


Figure 4.12: Strain Rate Sensitivity of Moduli of Elasticity

analyses are summarized in Table 4.2. Average strains in the initial crack tip element prior to onset of micro-crack tip propagation were used to compute the strain rates as shown in column 3. The damaged region which was induced by shrinkage stress at the precast notch tip during concrete curing was modeled by using the reduced modulus of elasticity,  $E_{tsm}$  shown in column 6.

Figure 4.13 shows the variations in the constitutive equation, which relates the crack closure stress and the COD in the FPZ, with strain rate. The crack closure stress shape factor,  $\alpha$ , (Fig. 3.5 and Eq. 3.7) is related to the slope of the constitutive relation in Figures 4.2 and 4.13. Values for  $\alpha$  are listed in column (8) of Table 4.2. Also shown for comparison is the three-segment model which was obtained previously for static crack extension [68].

Figure 4.14 shows that the fracture energy density,  $G_F$ , is strain rate insensitive. Its value remained constant in spite of the application of loading rates that markedly changed the tensile strength and modulus of elasticity of the concrete.

#### 4.4 Discussion

The increasing tensile strength with increasing loading rate indicates a reduction in the microcracked region, which precedes the propagating crack tip, with increasing strain rate.

**Table 4.2**  
**Strain Rate Sensitivity of Mechanical Properties**

Group No.	Specimen No.	$\dot{\epsilon}$ (sec $^{-1}$ )	$E_{cd}$ (GPa)	$E_{td}$ (GPa)	$E_{tsm}$ (GPa)	$f'_{td}$ (MPa)	$\alpha$	$G_f$ (N/m)
1	011	0.231	58.6	55.2	12.4	7.86	1.6	154
	012	0.252	58.6	55.2	19.3	8.00	1.6	156
2	021	0.108	49.6	42.7	6.2	5.98	1.8	154
	022	0.0877	51.7	43.4	9.0	5.67	1.8	154
3	031	0.0189	43.4	41.4	8.3	4.56	2.0	155
	032	0.0158	44.8	44.8	13.8	4.61	2.0	154
4	041	0.0046	44.8	40.0	9.0	4.17	2.2	149
	042	0.00373	44.8	37.9	15.2	4.21	2.2	151
5	051	0.00053	41.4	34.5	6.9	3.66	2.5	144
	052	0.00045	41.4	34.5	13.8	3.79	2.5	144

$\dot{\epsilon}$ : average strain rate computed at notch tip element prior to onset of microcrack propagation.

$E_{cd}$ : dynamic compression modulus of elasticity.

$E_{td}$ : dynamic tensile modulus of elasticity.

$E_{tsm}$ : dynamic tensile modulus of elasticity of notch tip element.

$f'_{td}$ : dynamic tensile strength.

$G_f$ : fracture energy density

$\alpha$ : crack closure stress shape factor. (Fig. 3.5 and Eq. 3.7)

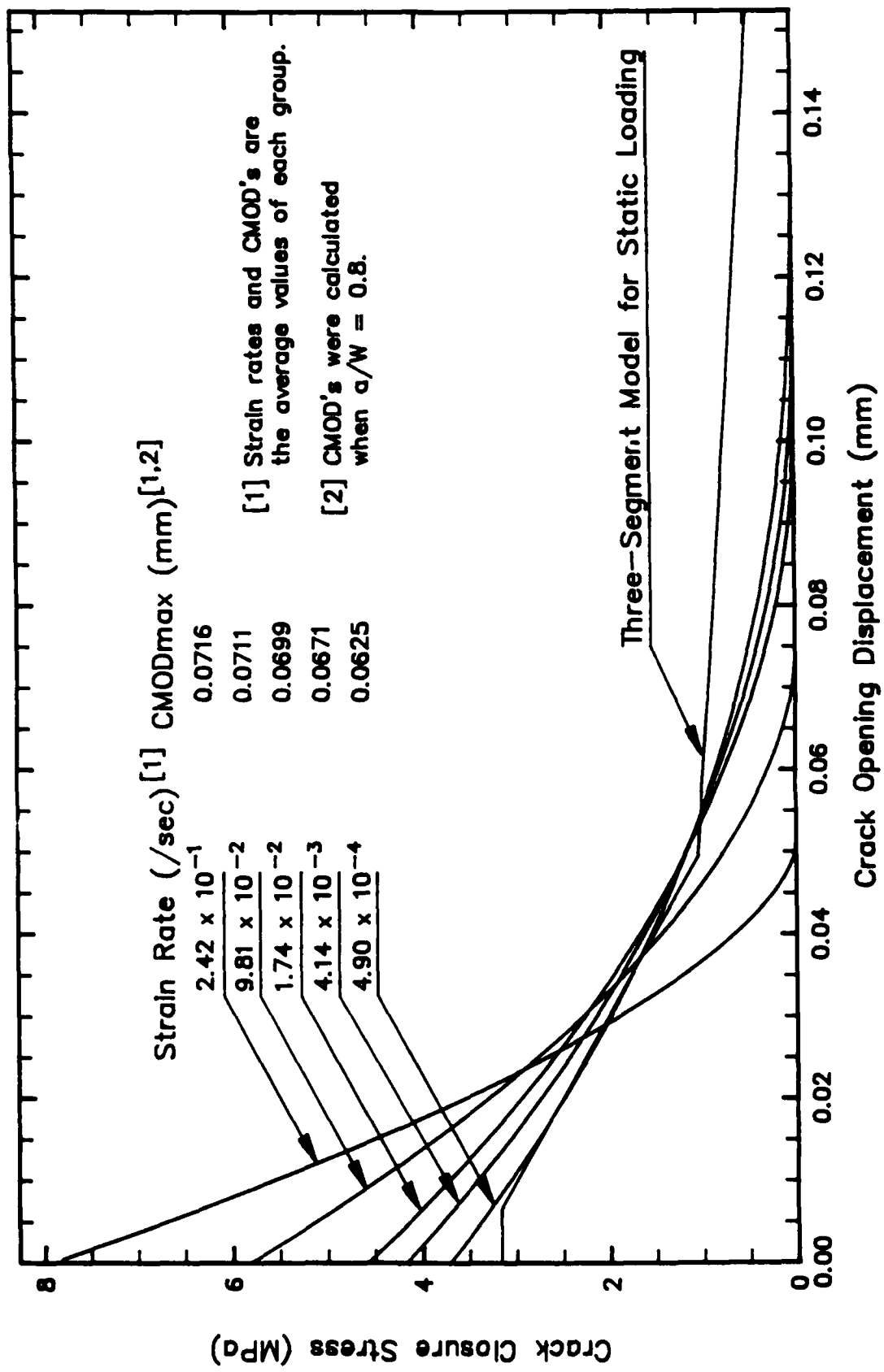


Figure 4.13: Strain Rate Sensitivity of FPZ Constitutive Relation

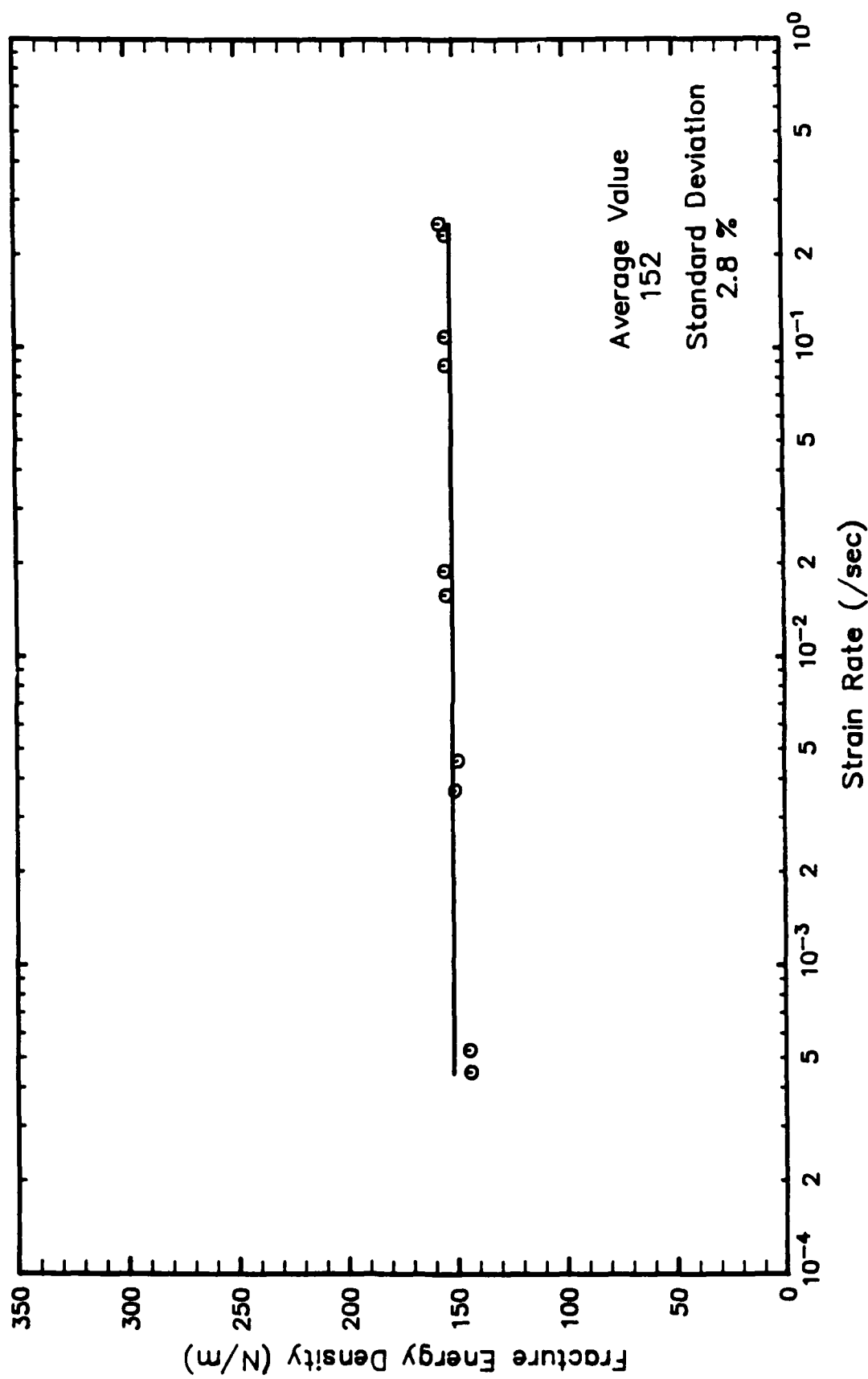


Figure 4.14: Strain Rate Sensitivity of Fracture Energy Density

The crack closure stresses in the FPZ, which trail the crack tip, thus increase with increasing strain rates. This result is consistent with the findings for slow loading rates reported in [70].

As shown in the legend for Figure 4.13, the calculated maximum crack mouth opening displacements ( $CMOD_{max}$ ) at the precast notch tip never reached the critical COD,  $COD_c$ , for average strain rates less than  $0.0981 \text{ sec}^{-1}$ . For the average strain rates of  $0.0981$  and  $0.242 \text{ sec}^{-1}$ ,  $CMOD_{max}$  was approximately equal to  $COD_c$  and  $CMOD_{max}$  was greater than  $COD_c$ , respectively. The FPZ was never fully developed at average strain rates equal or less than  $0.174 \text{ sec}^{-1}$  and the two halves of the fractured specimen remained rigidly attached to each other after the microcrack had penetrated through the last ligament of the specimen. The crack closure stress due to aggregate bridging had to be overcome in order to separate the two halves.

Figures 4.3, 4.4, 4.7 and 4.8 show that the peak load was achieved when the strain at gage SG03 changed from compressive to tensile strain. The numerical results showed that the microcrack tip had then extended to about 43.1mm (1.7 in.) from the precast notch tip. This FPZ length of 43.1mm (1.7 in.) was independent of the notch tip strain rate and must therefore be a function of specimen geometry.

Since the FPZ did not fully develop in the specimens subjected to the slower strain rate loadings, i.e average strain rates equal or less than  $0.174 \text{ sec}^{-1}$ , larger size specimens are needed for comprehensive studies of strain rate effects on crack closure stresses. Also slight discrepancies in the measured and computed strains after passage of the microcrack tip through the location of SGO2 suggest that further decrease in the crack closure stress in the trailing portion of the constitutive relation in Figure 4.14 may be warranted. Finally the difficulties with determining the response for the ligament at the precast notch tip, due to shrinkage effects, demonstrate clearly the need to minimize factors that cause those effects due to laboratory testing and the likely importance of those effects for practical applications of fracture mechanics to concrete structures.

#### 4.5 Conclusions

This dynamic fracture study of concrete three-point bend specimens showed that for the range of strain rates studied (0.0009 through  $0.24 \text{ sec}^{-1}$ ):

- (1) The log of the tensile strength increased almost linearly with the log of the strain rate. The strength at the fastest rate of  $0.24 \text{ sec}^{-1}$  was 110 percent greater than the static tensile strength.

- (2) The logs of the tensile and compressive moduli of elasticity increased almost linearly with the log of the strain rate. Tensile and compressive moduli of elasticity at the fastest rate of  $0.24 \text{ sec}^{-1}$  were 60 and 40 percent larger, respectively, than the values for static loading.
- (3) The average crack velocity increased with increasing strain rate and reached 132 m/sec (5200 in/sec) for a strain rate of  $0.24 \text{ sec}^{-1}$ .
- (4) A fully developed fracture process zone (FPZ) was not achieved in any of the specimens fractured at strain rates equal to or less than  $0.174 \text{ sec}^{-1}$ . In all specimens, the FPZ extended about 43 mm (1.7 in) prior to the achievement of the maximum load and that length was not strain rate sensitive. Specimens with greater overall depths than those tested here are necessary for studies of FPZ length variations.
- (5) The crack closing stress for a given crack width was strain rate dependent. However, since the tensile strength increased with strain rate and the critical opening displacement,  $\text{COD}_c$ , for zero closing stress decreased with strain rate, the fracture energy density was strain rate independent.

## CHAPTER 5

### IMPACT LOADING THREE-POINT BEND TESTS WITH MOIRE INTERFEROMETRY

#### 5.1 Introduction

In order to examine, in further detail, the dynamic fracture response of concrete under dynamic loading, one series of the three-point bend specimens reported in Chapter 4 was repeated using a drop weight set-up and with the transient moire interferometry fringes surrounding the rapidly propagating crack recorded. This chapter describes the results of those tests and their interpretation.

The test set-up was described previously in Section 3.2 along with details of the Moire Interferometry instrumentation. The experiments used three point bend specimens whose geometry and concrete properties duplicated those of the specimens described in Chapter 4.

#### 5.2 Numerical Analysis

The input conditions for the dynamic finite element propagation analysis of the test results were experimentally determined impact load and an assumed constitutive relationship which relates the crack closure stress and the crack opening

displacements, COD's, in the FPZ. The initial form used for this constitutive relation was the same as that derived in the prior displacement controlled tests. Crack extension was accomplished by advancing the micro-crack tip i.e. the tip of the FPZ, when the crack tip element reached the dynamic tensile strength,  $f'_{td}$ , for the concrete.  $f'_{td}$  was obtained by multiplying the static splitting tensile strength,  $f'_{td} = 6.5 \sqrt{f'_c}$ , by the ratio of the dynamic to static peak loads for failure of the SEN three point bend specimens. The resultant  $f'_{td}$ , which is given in Table 5.1, was 13.1 MPa (1,900 psi). There was an unique value of  $f'_{td}$  since only one drop weight height was used.

The macro-crack tip, (the tip of the traction free crack which is preceded by the FPZ), was advanced when the crack opening displacement (COD) reached a specified critical crack opening displacement ( $COD_c$ ).

A continuous function was used to relate the crack closure stress,  $f_{ccs}$ , and the COD as follows:

$$f_{ccs} = f''_{td} \cdot (1-\bar{\omega})^\alpha \quad (5.1)$$

where  $\bar{\omega} = COD/COD_c$  is the crack opening displacement rate,  $\alpha$ , is the crack closure stress shape factor and  $f''_{td}$  is the "maximum" dynamic crack closure stress which is equal to or less than  $f'_{td}$ .

**TABLE 5.1**  
Mechanical properties

• **Strength**

Static compressive strength; (measured)

$$f_c' = 55.2 \text{ MPa} (7,990 \text{ psi})$$

Static splitting tensile strength; (measured)

$$f_{ts} = 3.96 \text{ MPa} (575 \text{ psi}) = 6.43 \sqrt{f_c'}$$

Dynamic tensile strength (for micro-crack extension criterion);

$$f_{td}' = 13.1 \text{ MPa} (1,900 \text{ psi})$$

• **Dynamic elastic moduli**

Tension  $E_{td} = 34.4 \text{ GPa} (5,000 \text{ ksi})$

Compression  $E_{cd} = 41.6 \text{ GPa} (6,000 \text{ ksi})$

• **Strain rate at the crack tip element**

$$\epsilon = \frac{f_{td}'}{E_{dt} \cdot t_F} = 1.48/\text{sec}$$

where  $t_F$  is time at which the crack propagates

• **Crack closure stress**

$$f_{ccs} = f_{td}'' \cdot \left(1 - \frac{COD}{COD_c}\right)^\alpha$$

where  $f_{td}'' = 5.24 \text{ MPa} (760 \text{ psi})$ ,  $\alpha = 1.5$  and

$COD_c = 0.0762 \text{ mm} (0.003 \text{ in})$

• **Fracture energy density**

$$G_F = \frac{1}{1+\alpha} \cdot f_0 \cdot COD_c = 160 \text{ N/m} (0.912 \text{ lb/in})$$

• **Crack Velocity** (Average value after 12.7 mm crack extension)

$$\dot{a} = 290 \text{ m/s} (977 \text{ fps})$$

Appropriate values for  $\alpha$ ,  $COD_c$ ,  $f''_{td}$  were obtained, as explained previously, by numerically matching the measured and predicted global responses for the specimen. An iterative analysis was required during each time increment of the dynamic finite element analysis in order to obtain a kinematically admissible COD and a dynamically admissible crack closure stress along the FPZ.

The fracture energy density,  $G_F$ , can then be computed by

$$G_F = \int_0^{COD_c} f_{ccs} d(COD) = \frac{1}{1+\alpha} f''_{td} COD_c \quad (5.2)$$

The initial guess for the maximum crack closure stress,  $f''_{td}$ , was obtained using the COD variation near the crack tip. In contrast to the findings in Chapter 4, numerical experimentation showed that for these experiments the maximum crack closing stress,  $f''_{td}$ , could not be equated to the tensile strength,  $f'_{td}$ . The physical significance of this finding will be discussed later. After the numerical iteration process, the fracture properties, i.e. maximum crack closure stress,  $\alpha$  and  $COD_c$ , as well as the tensile and compressive moduli of elasticity,  $E_{td}$  and  $E_{cd}$ , respectively, were obtained via an inverse process in which these properties were optimized to fit the measured strain histories for the three gage locations shown in Figure 4.1.

### 5.3 Results

#### 5.3.1 Experimental Results

Four specimens were fractured with an impact load dropped from a height of 400 mm (15.7 in). As shown in Figure 5.1, the time variations of the impact load were nearly identical for the four tests except for an unexplained spike load in Test No. 3. Figures 5.2, 5.3 and 5.4 show the strain gage times histories of the four tests for gages SGO1, SGO2 and SGO3, respectively. Despite the strong similarity of the load traces, the strains for gages SGO1 and SGO2 in the tension region varied considerably in the four tests. Thus "average" result for those two gages, which was consistent with the strain histories for all four tests, were used in the numerical analysis. That average history is shown as a unbroken line in Figs. 5.1 through 5.4. Also shown in Figures 5.2, 5.3 and 5.4 are the time at which the FPZ tip passed a given strain gage location. The strain peaks for strain gages SGO2 and SGO3 in Figures 5.3 and 5.4, were taken as the time at which the FPZ tip passed those gages. However, such was not the case for the first strain gage, i.e. SGO1 in Figure 5.2, since previous numerical experimentation showed that locked-in shrinkage stresses, generated during the handling and testing of the prenotched specimen, altered the behavior at that location. Previous

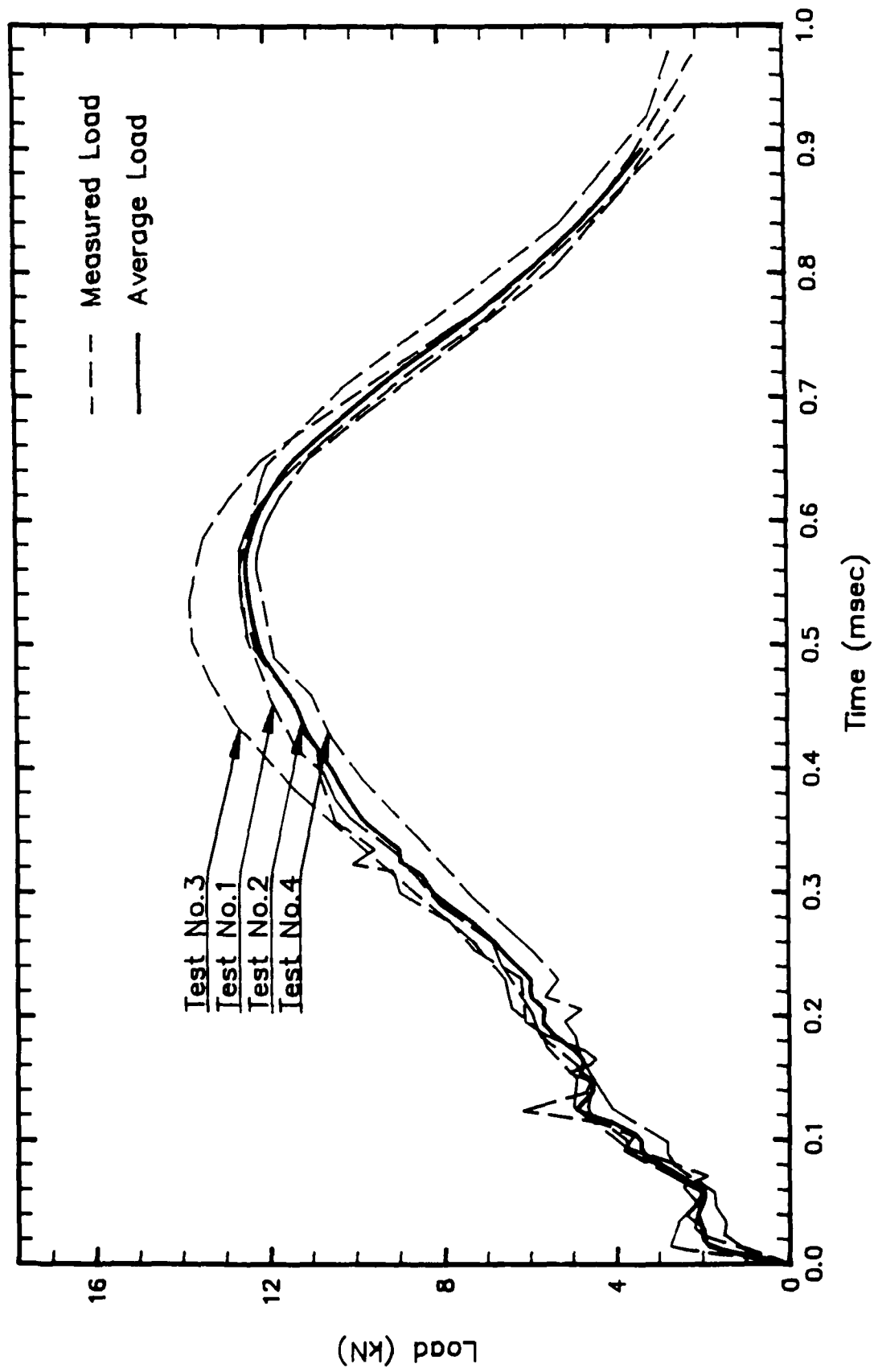


Figure 5.1: Measured and Average Load Histories

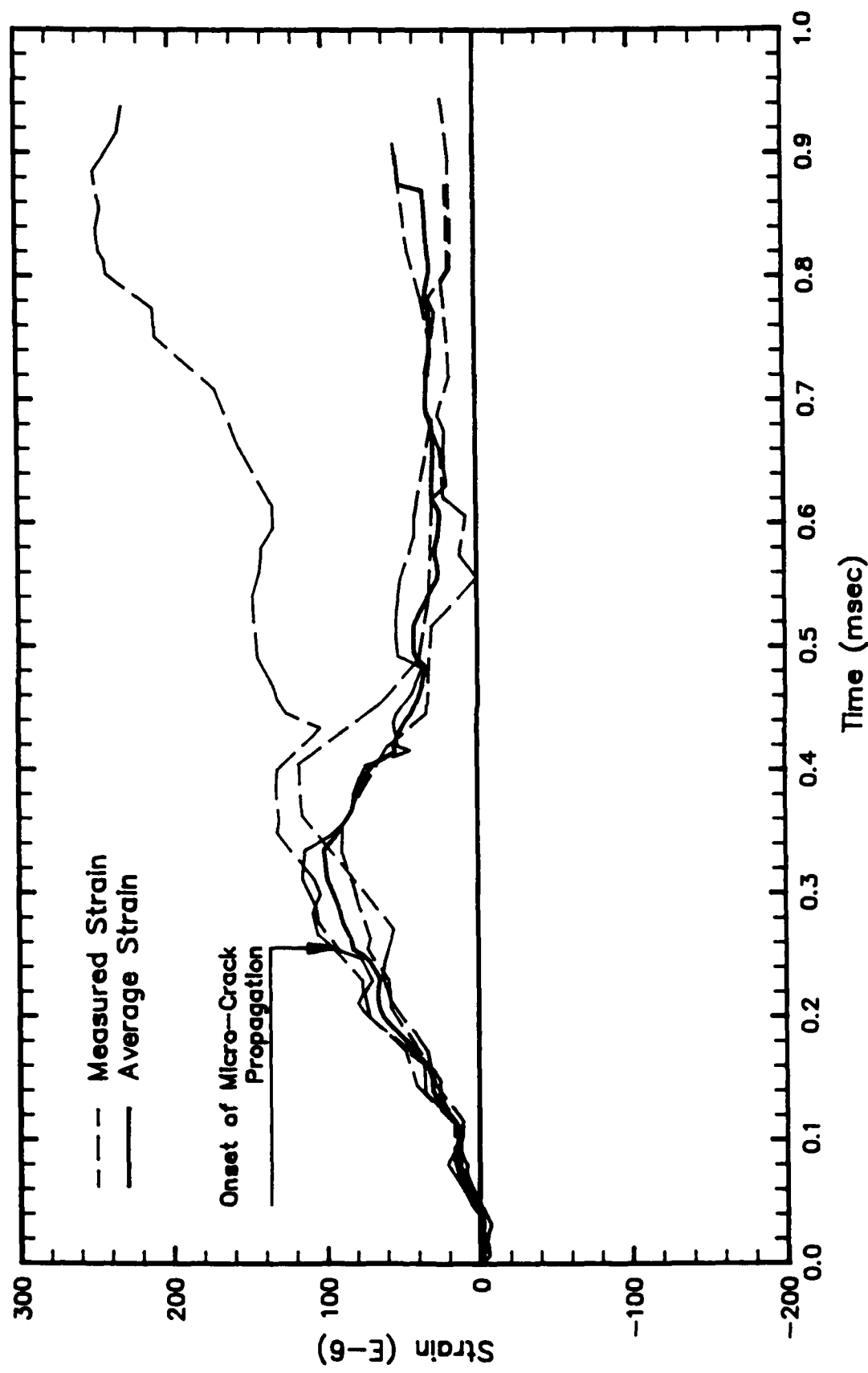


Figure 5.2: Strain Histories at SG01

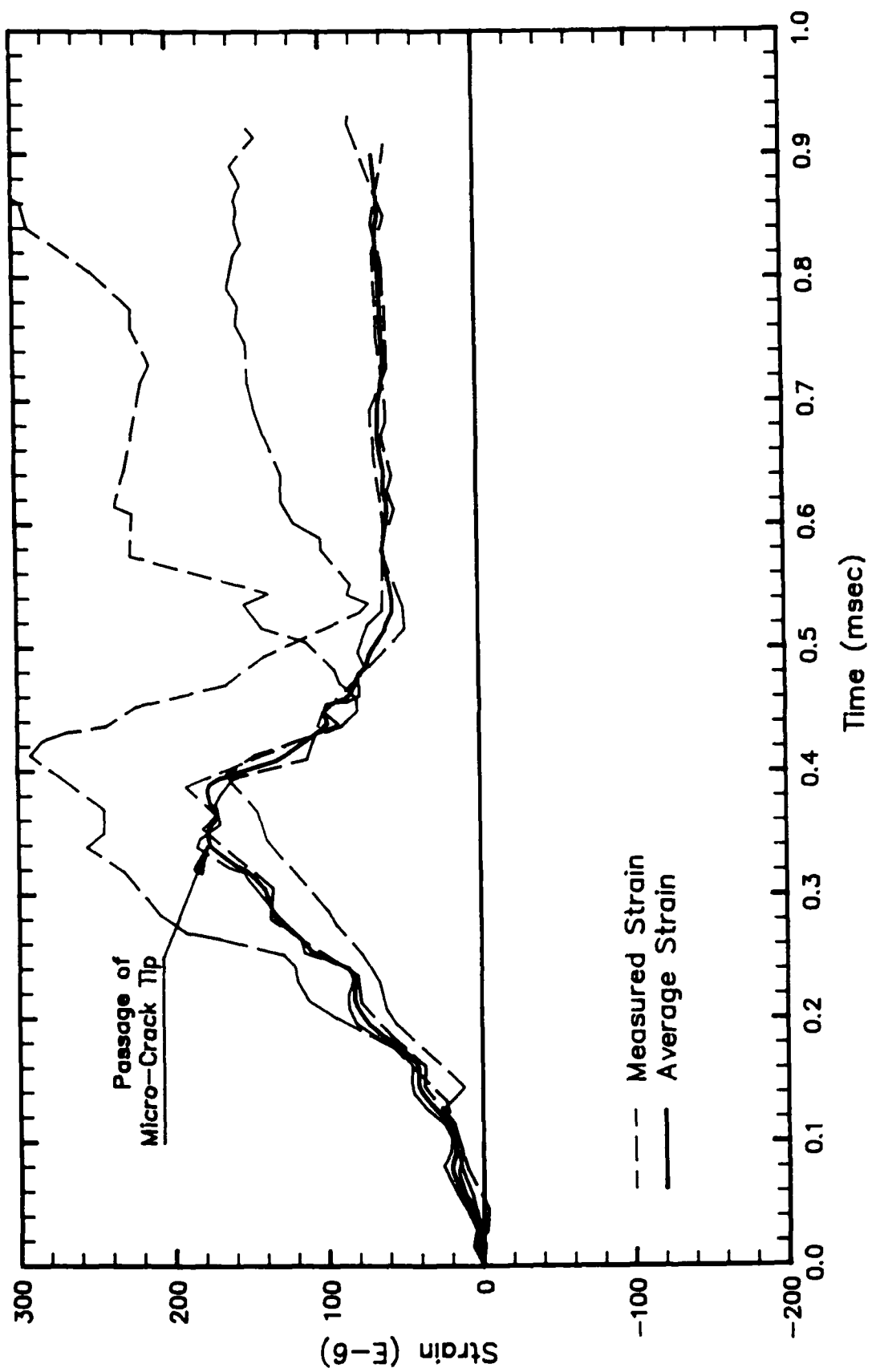


Figure 5.3: Strain Histories at SG02

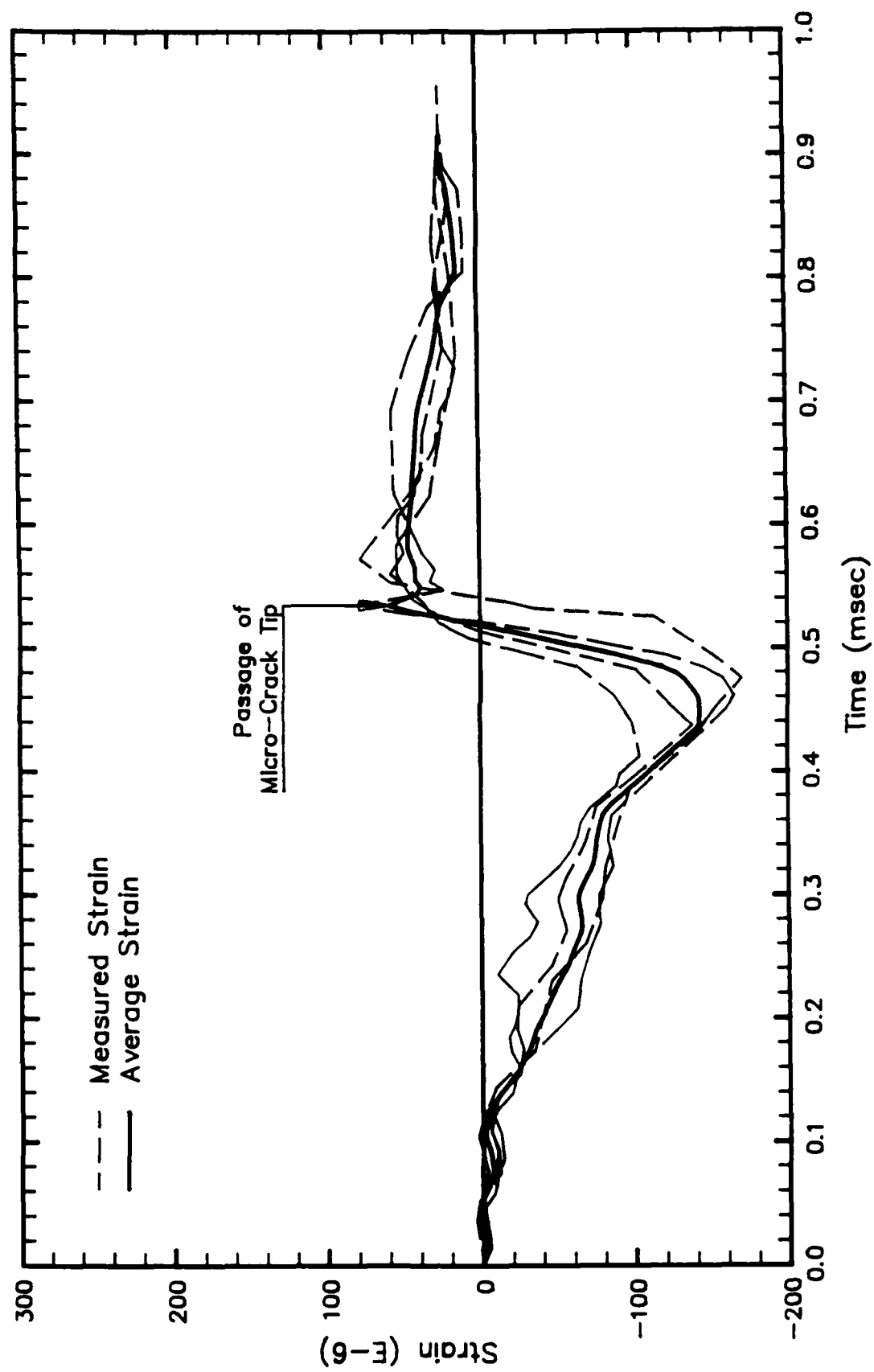


Figure 5.4: Strain Histories at SG03

numerical experimentation also indicated that dynamic microcrack tip extension initiated at 0.26 msec or at the first consistent change in strain rate in the SG01 record. The continued slight rise and the subsequent plateau in the SG01 strain history represented continuous increase in strain in the crack tip element despite the onset of micro-crack propagation at about 0.26 msec. In contrast, the passage of the crack tip at SG02 and SG03 is characterized by a precipitous drop in strains with the passage of the microcrack tip. Average crack velocities were 151 m/sec between strain peaks for SG01 and SG02 and 257 m/sec between strain peaks for SG02 and SG03. This average crack velocity is 19% lower than the crack velocity 320 m/sec which was obtained from the moire interferometry data described next.

Figure 5.5 shows four typical sequential frames of the moire interferometry fringe patterns associated with a propagating crack for a given trigger delay time. By varying for each of the four test beams, the trigger delay time of the IMACON 790 from 30' to 600 micro-seconds in intervals of 100 micro-seconds a sequence of crack opening profiles with rapid crack extension was obtained. Figure 5.6 shows with symbols variations in crack opening displacement (COD) that could be determined from those moire patterns. The authors' previous moire interferometry data, involving stable crack growth in similar concrete fracture specimens loaded statically, [69-71] showed that COD variations narrowed toward the crack tip. In

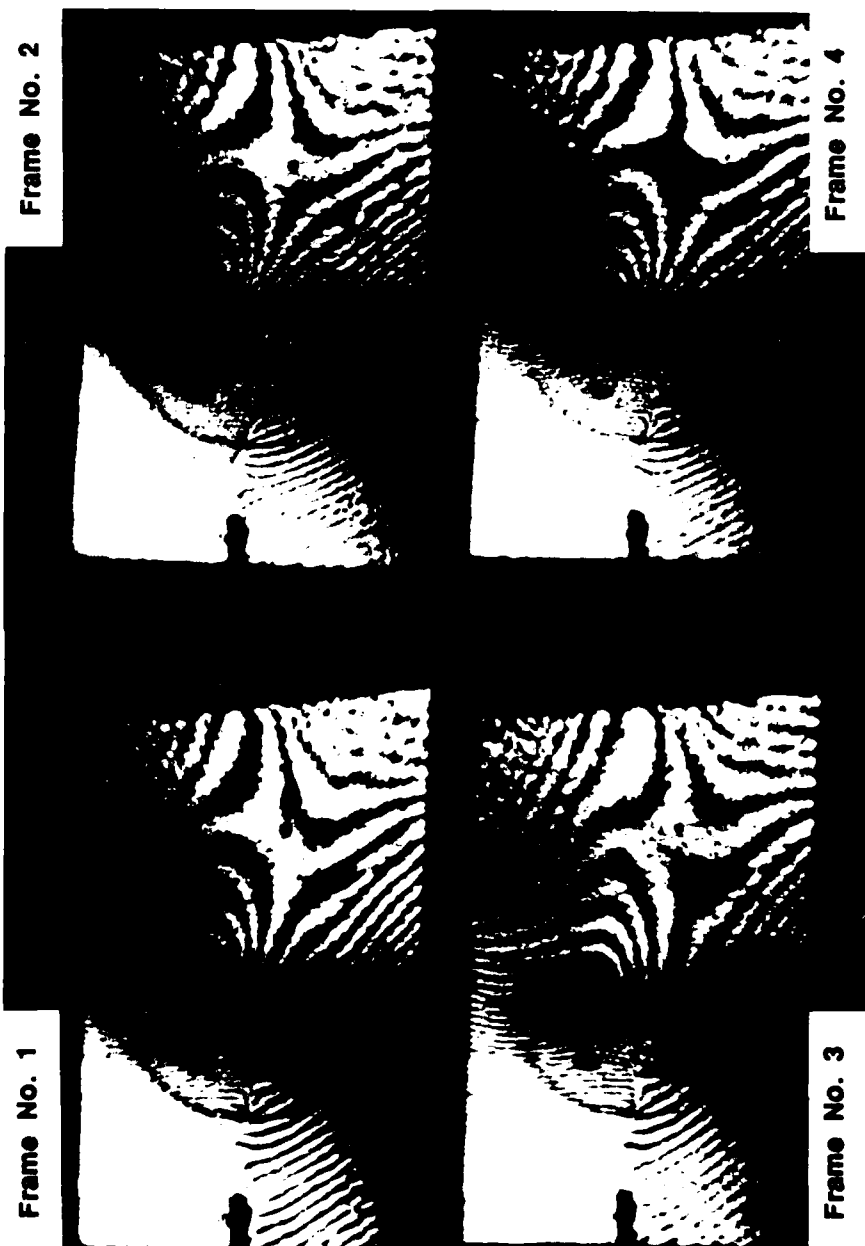


Figure 5.5: Moire Interferometry Record of Specimen No. 3.  
Frame Interval 10 micro-seconds

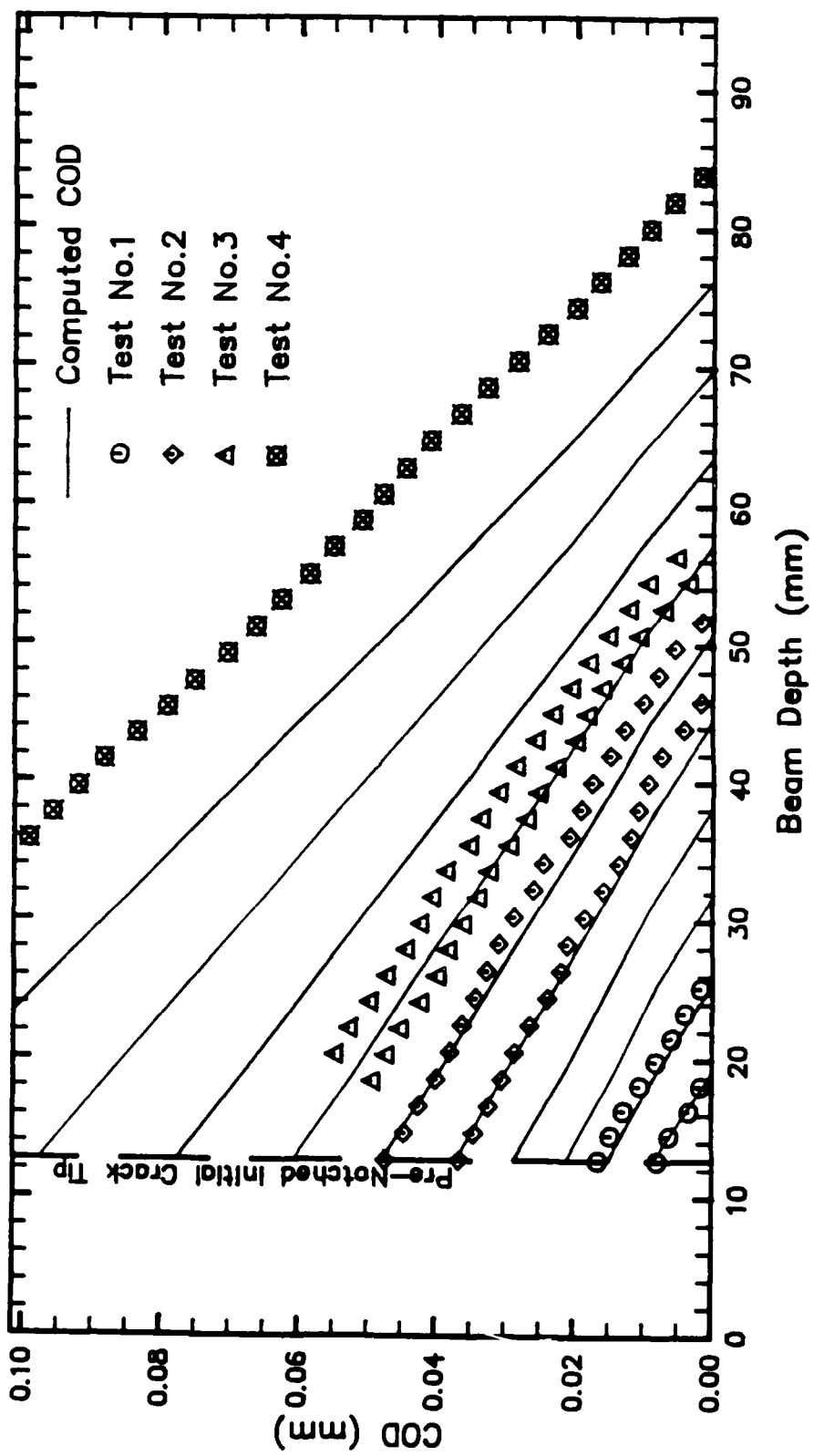


Figure 5.6: COD variations of a propagating crack

contrast, in Fig. 5.6, the COD variations in the vicinity of the crack tip suggest a parabolic crack opening profile. Such a crack opening profile, which is in agreement with the results in [72], suggests a decreasing influence of crack bridging and a gradual transition to linear elastic fracture mechanics with increasing strain rates.

### 5.3.2 Numerical Results

The average impact load and the assumed constitutive relation, i.e. Equation (5.1), were used as input boundary conditions for the propagation analysis [66] of the "average" result of the four tests. The results and the experience obtained from the prior analysis of the displacement controlled tests reported in Chapter Four greatly reduced the effort in the iterative process necessary to match the computed and measured crack extension and the three strain gage histories.

Figure 5.7 shows the computed crack extension histories. The slow crack velocities during the initial phase of dynamic crack propagation are believed to be caused by the pre-existing damage region which, as mentioned previously, is the result of the shrinkage effects at the precast notch tip during curing and subsequent handling of the specimens. The symbols in the figure indicated the measured crack extension as recorded by the strain gage histories of SG01, SG02 and SG03.

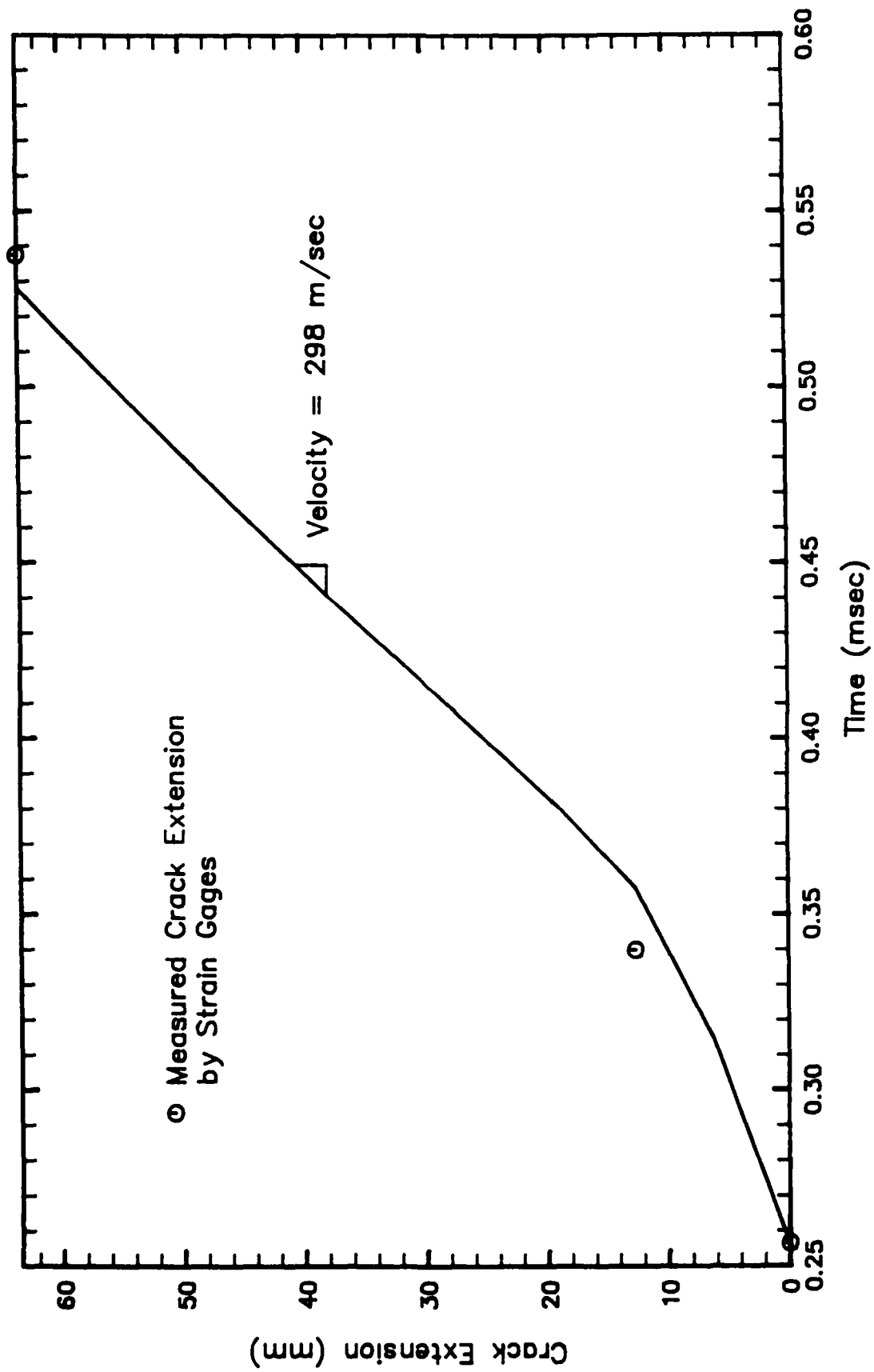


Figure 5.7: Crack Extension History

Figure 5.8 shows the measured and computed average strain histories at the three strain gage locations. Reasonable agreement between the computed and measured strains are noted prior to the arrival of the microcrack tip of the FPZ at the given strain gage location. The subsequent decrease in the measured strains is also modelled relatively well, and particularly well for SG03, by the numerical simulation. As noted previously, the strains for SG01 are less than those expected for elastic behavior because the modulus for the first two elements in front of the crack tip was reduced as described in Chapter Four.

In Figure 5.6, the solid curves represent the computed COD variations with crack extension. In this study, unlike in the previous stable crack growth studies, the computed crack opening profile shows a more blunt crack tip that agrees well with the crack tip profile computed from the moire interferometry results.

Figure 5.9 shows the relation between the average measured load and the computed load-line displacements. Strain softening of the curve was not predicted until a load line displacement in excess of 0.25 mm (0.01 in). However, since the crack tip was only three nodes away from the impact point at that time, computation was terminated at 0.20 mm (0.008 in).

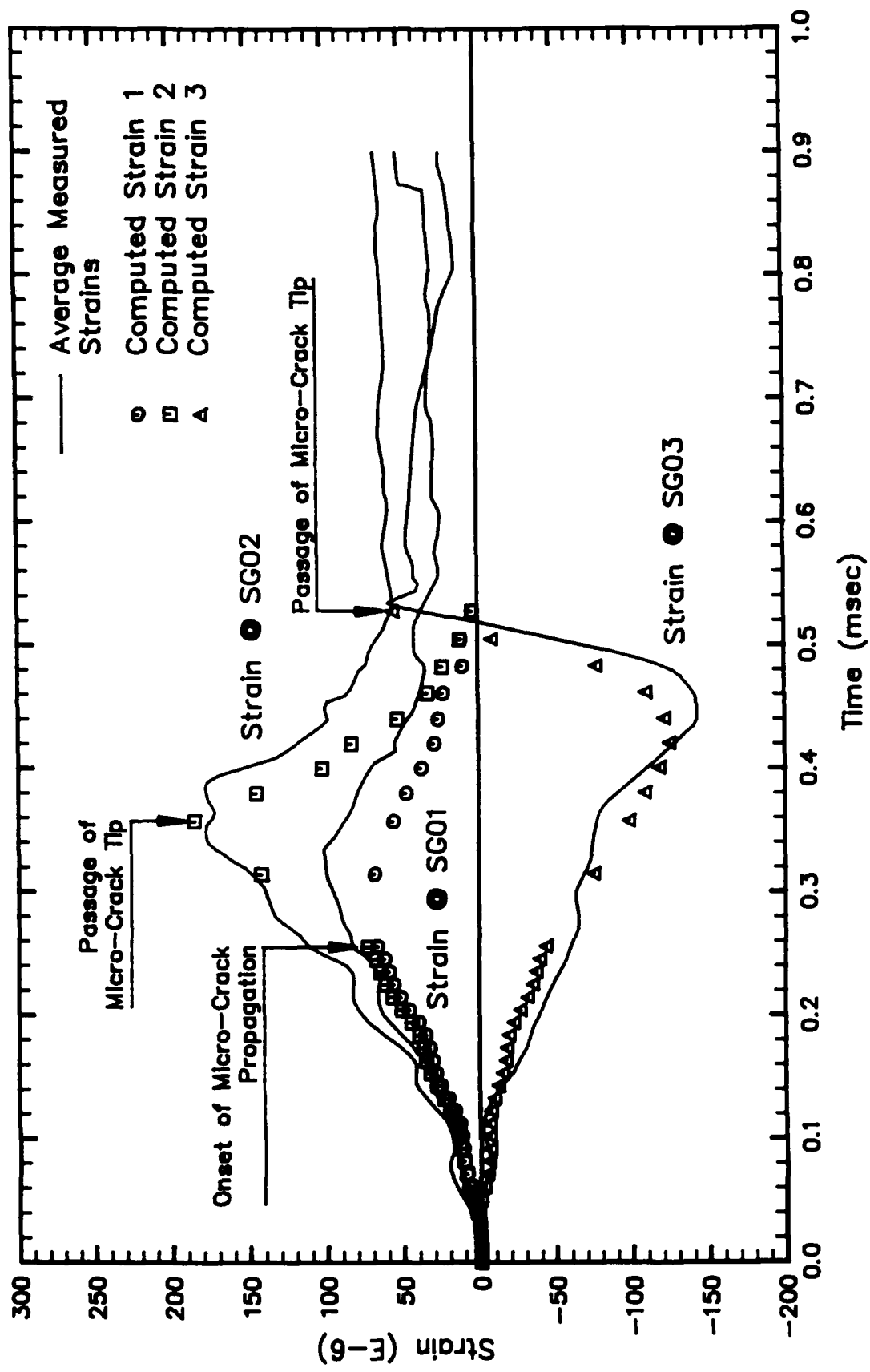


Figure 5.8: Comparisons of Average Measured and Computed Strain Histories

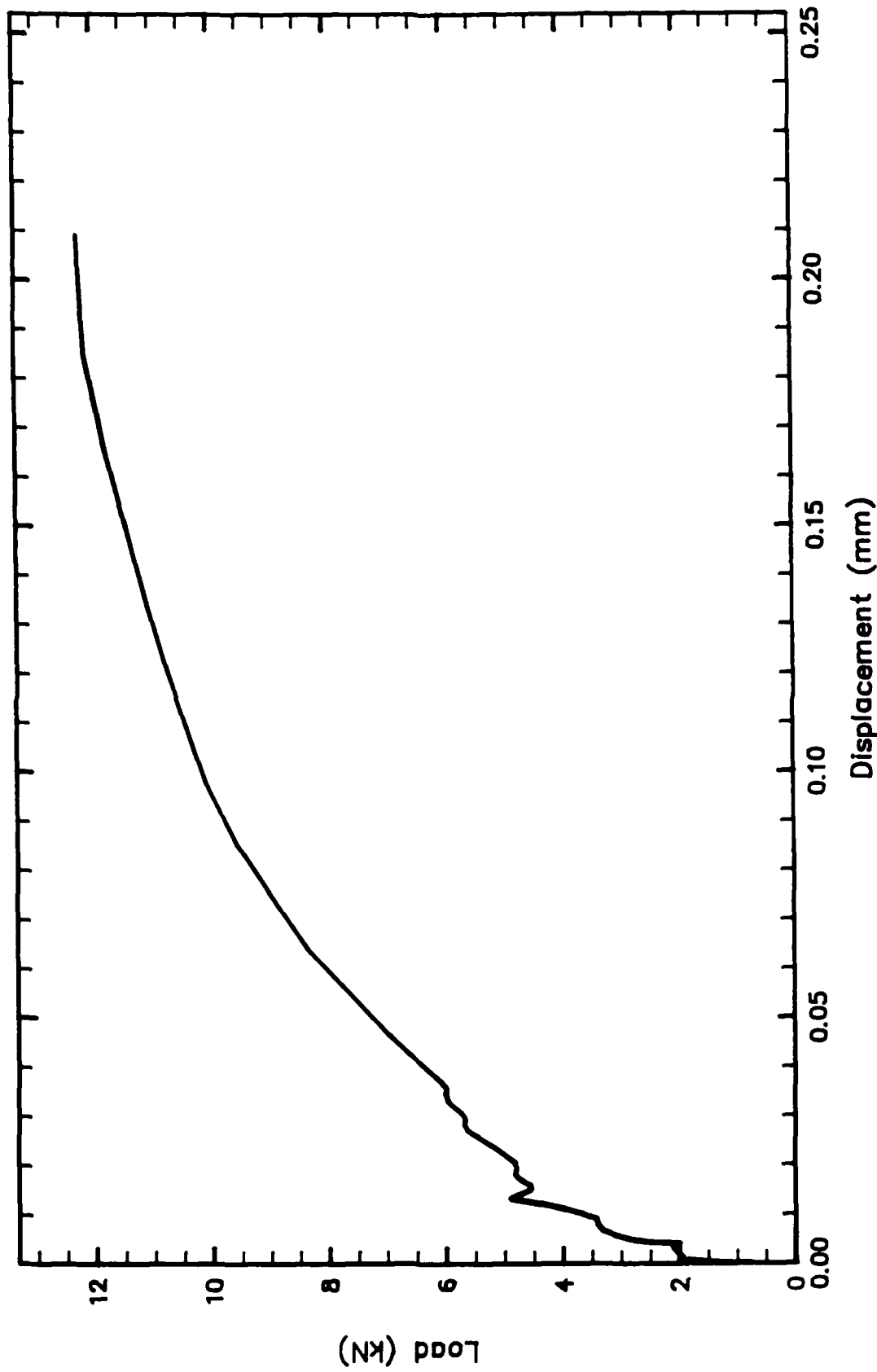


Figure 5.9: Measured Load versus Computer Load-Line Displacement

Figure 5.10 shows the variations in the different energies with crack propagation. The sum of the three energies, i.e. strain, kinetic and fracture, was at the worst within 3 percent of the corresponding input work during the dynamic fracture process. The excellent agreements between the instantaneous measured and computed total energies provides additional verification of the numerical analysis.

### 5.3.3 Strain Rate Sensitivity of Mechanical Properties

The final material properties gleamed from the entire numerical analysis, are summarized in this section. The computed dynamic tensile strength,  $f'_{td}$ , and the tensile and compressive moduli of elasticity are shown in Table 5.1. Also shown are the static properties obtained from compression tests on 152.4 x 304.8 mm (6 x 12 in) cylinders. The increase in the dynamic tensile strength,  $f'_{td}$ , at these high strain rates is consistent with the increased number of trans-aggregate fractures seen on the failure surfaces of these specimens as compared to the surface of the statically loaded specimens. The latter exhibited many more failures at the aggregate-to-paste interface. The factor causing the rapidly propagating crack to penetrate through the higher strength aggregates rather than around them is still an unanswered issue.

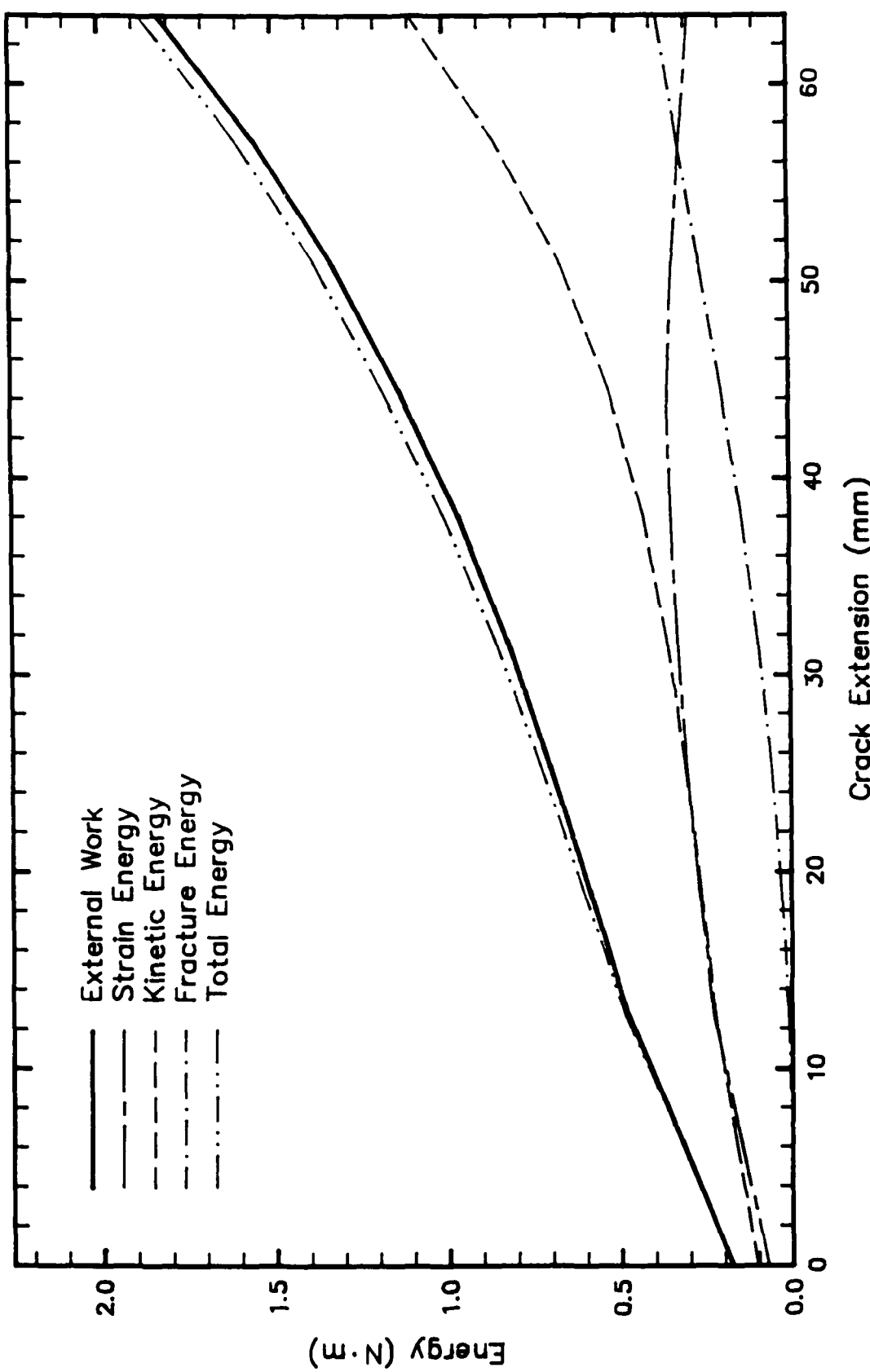


Figure 5.10: Computed Energy Partition

Figure 5.11 shows the variations in the constitutive equation, which relates the crack closure stress and the COD in the FPZ, as determined from the numerical analysis. The crack closure stress shape factor,  $\alpha=1.5$ , is related to the slope of the constitutive relation. The maximum crack closure stress of  $f_{td}'' = 760$  psi is 40% of the maximum tensile strength of  $f_{td}' = 1900$  psi necessary to advance the micro-crack tip of the FPZ.

#### 5.4 Discussion

The two tier tensile strength criterion used in propagating the FPZ in this study resembles the two parameter fracture model for concrete proposed by Jeng and Shah [75]. While a constant tensile strength criterion was used in this finite element model (FEM) to advance the micro-crack tip of the FPZ, the same FEM analysis can also be used to compute the variation in the stress intensity factor. The coarse FEM mesh used in this study required the use of a calibrated crack tip stress field to compute the stress intensity factor variation with crack extension. The result is shown in Figure 5.12. The dynamic stress intensity factor remained essentially constant during crack propagation except for the initial and terminal phases. That lack of constancy means that use of a critical stress intensity factor as a fracture criterion is not justified for these tests. The tensile strength criterion of crack extension

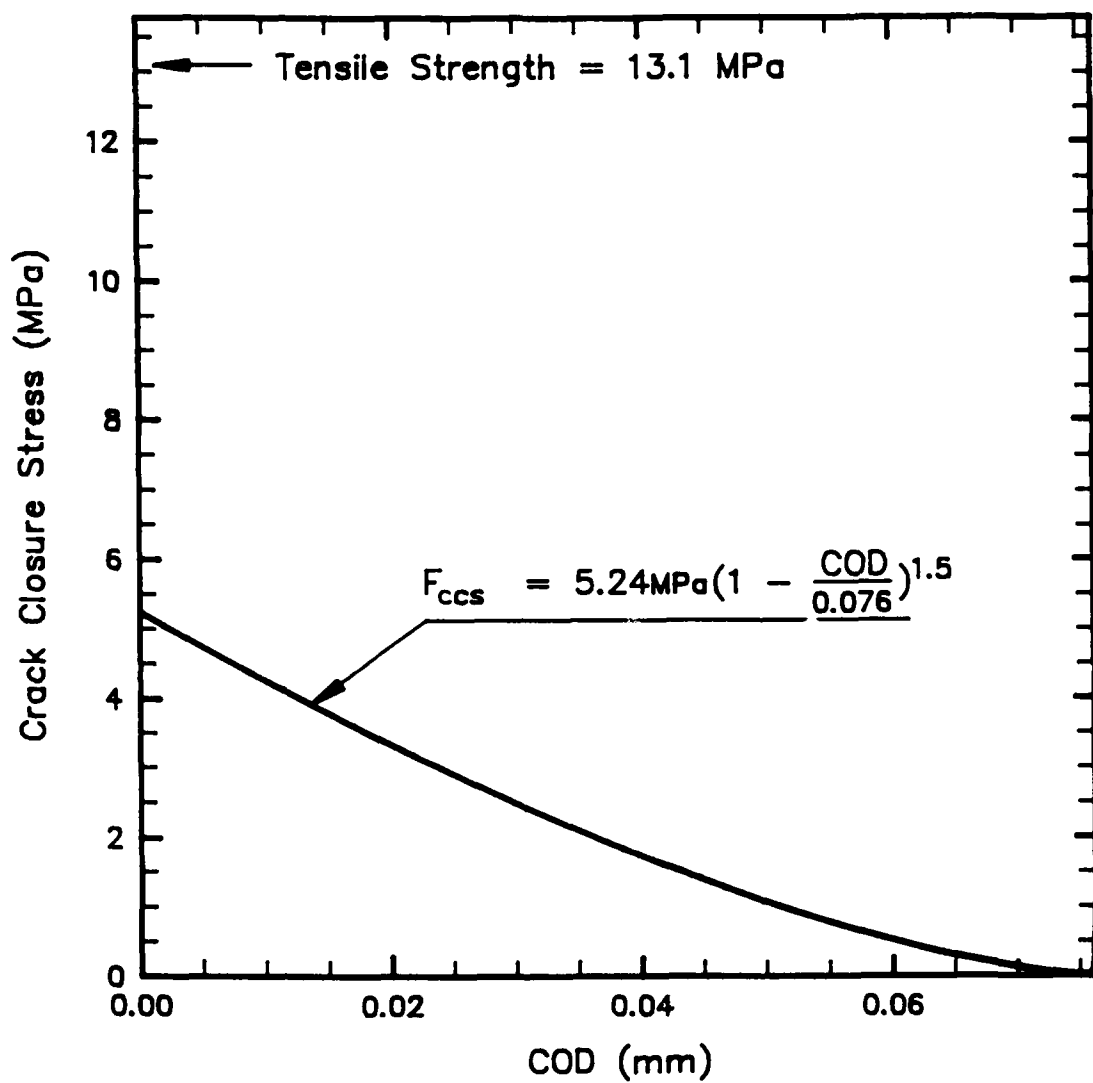


Figure 5.11: FPZ Constitutive Relation

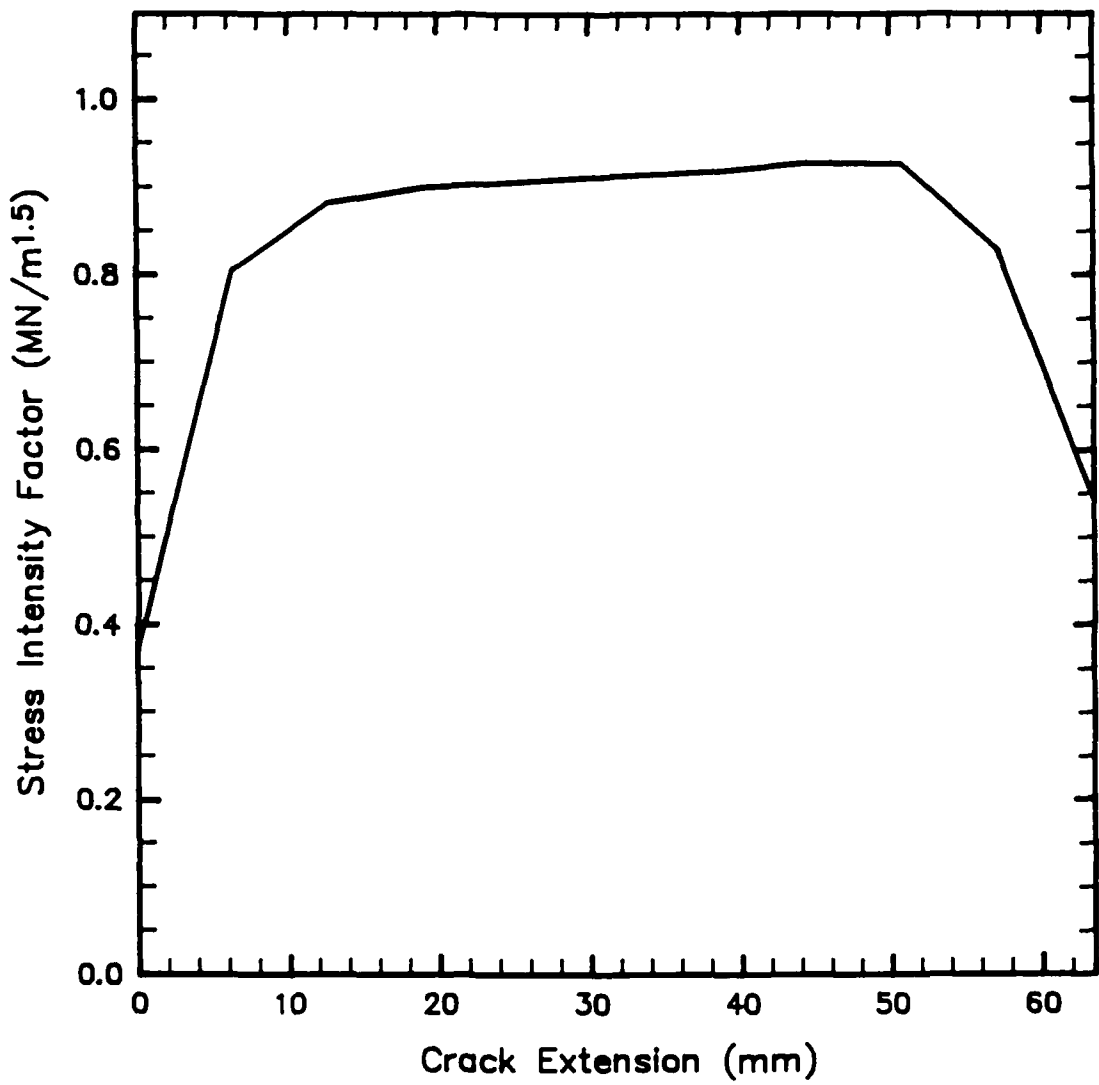


Figure 5.12: Stress Intensity Factor versus Crack Extension

used in this analysis, on the other hand, is enforced apriori in this study and thus  $f'_{td}$  remains constant for all phases of crack propagation.

The six fold increase in the strain rate from that used in Chapter Four resulted in the tensile strength  $f'_{td}$  being equal to 13.1 MPa (1900 psi) and therefore 60 percent higher than the 7.93 MPa (1150 psi) reported in Chapter Four. That change, however, was accompanied by rapid decreases in the FPZ strength and length, and those changes while unexpected, are consistent with the trend for the variations in the FPZ with increasing strain rate observed previously.

### 5.5 Conclusions

The following conclusions can be drawn from the results reported in this study.

- (1) Variations in COD data obtained by moire interferometry can provide additional insight on the dynamic fracture mechanism associated with a rapidly propagating crack in concrete.
- (2) For strain rate achieved in this study,  $1.48 \text{ sec}^{-1}$ , the influence of FPZ on the fracture process is reduced considerably compared to that for static loading. At the

1.48 sec<sup>-1</sup>, the dynamic fracture process approaches that of linear elasticity fracture mechanics.

(3) The tensile strength,  $f'_{td}$ , and maximum crack closure stress,  $f''_{td}$ , differed by a factor of 2.5.

## CHAPTER SIX

### CRACK-LINE, WEDGE-LOADED DOUBLE-CANTILEVER BEAM TESTS

#### 6.1 Experimental Setup

Crack-line wedge-loaded double-cantilever beam (CLWL-DCB) specimens, with proportions based on those described in ASTM E 561-81 [76] for R-curve testing in metals, were used to provide data for proportions of more practical size than the proportions of the three-point bend specimen used for the investigations described in Chapters 4 and 5. The geometry for those CLWL-DCB specimen is shown in Figure 6.1. Similar CLWL-DCB specimens have been used in static fracture studies by Jeang [13] and Du [74].

The CLWL-DCB specimens were selected for studies of strain rate sensitivity for the following reasons:

1. CLWL-DCB specimens can simulate conditions in a practical size beam as shown in Figure 6.2. The distance between the center of the hole and the edge in the CLWL-DCB specimen is about the same as the distance between the bottom of a beam and the center of its longitudinal reinforcement. The degree to which the wedge is driven into the hole in the specimen can also be said to simulate the effective degree of restraint provided by the reinforcement.

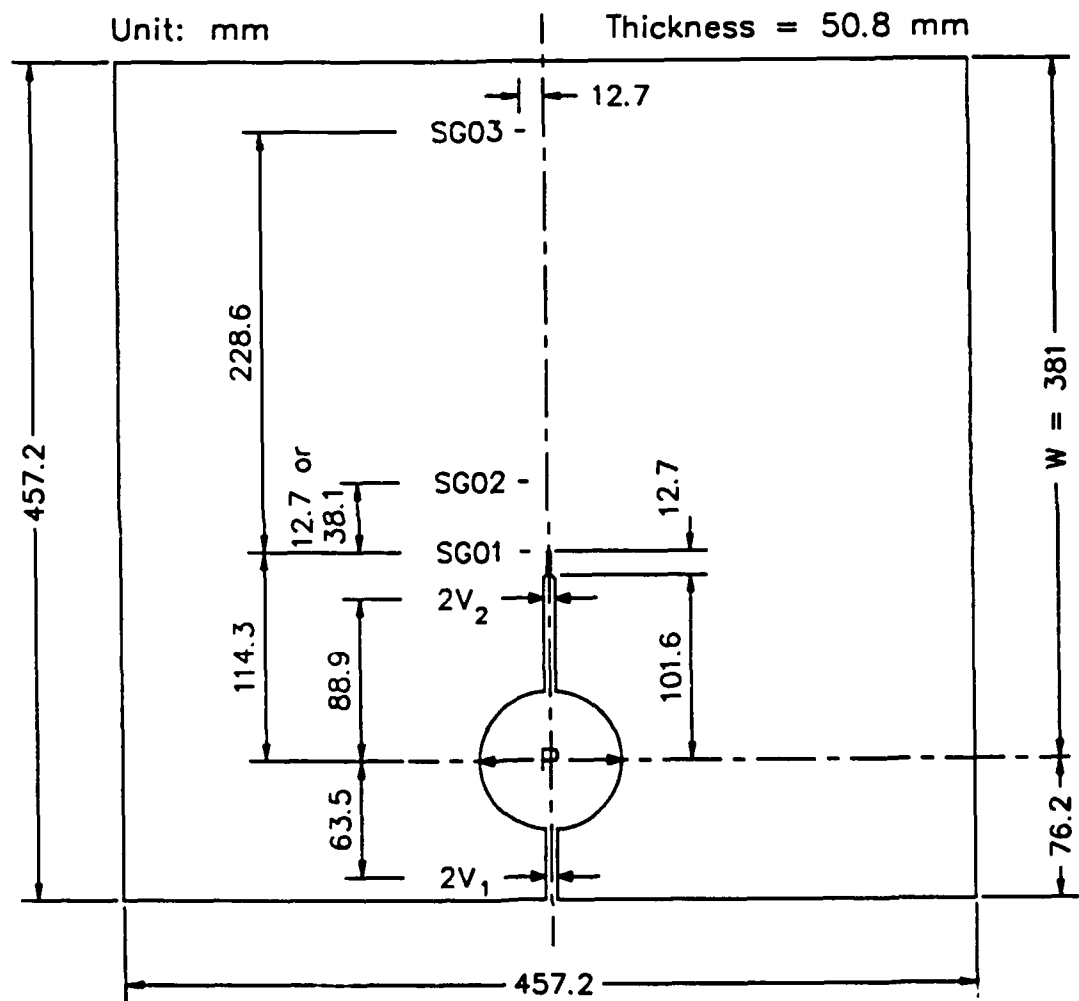


Figure 6.1: Geometry of a CLWL-DCB

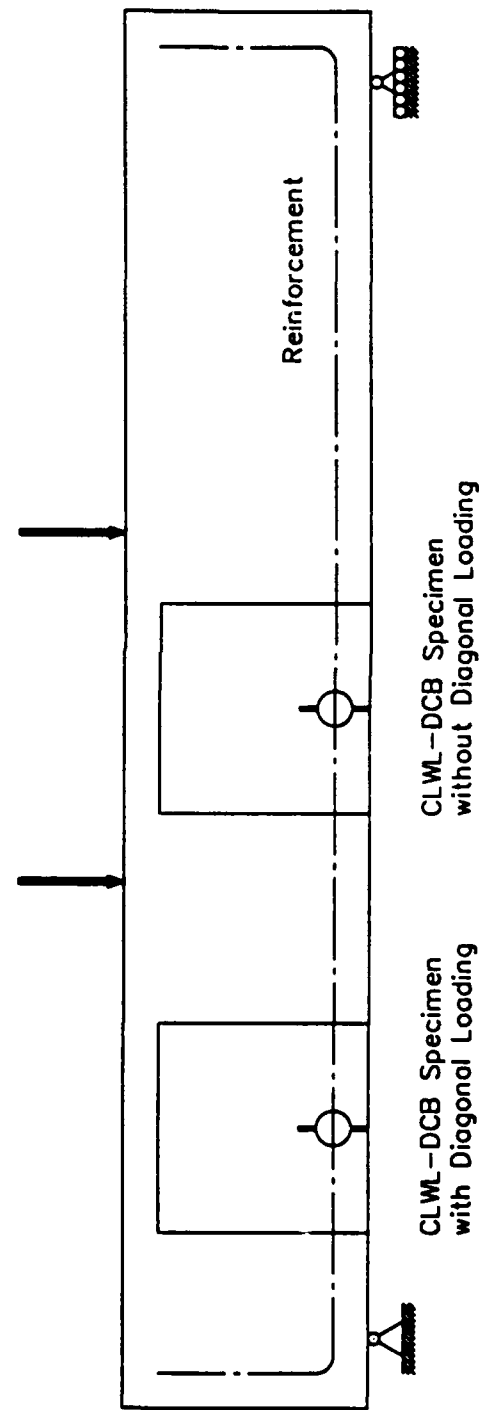


Figure 6.2: Correspondence between CLWL-DCB Specimens and Conditions in a Reinforced Concrete Beam

2. With CLWL-DCB specimens a testing machine can be used economically. With proper lubrication and system alignment, a testing machine producing more than 5 times the maximum expected test load will be adequate if the included angle of the loading wedge is 6 degrees.
3. A segmented split-pin system is effective for maintaining the load line independent of rotation of the specimen arms.

The fixtures for a CLWL-DCB test are more complicated than those for three-point bend tests since the latter are completely constrained by the three external loading points and the crack propagates towards the loading point from the initial notch tip. The fixtures for a CLWL-DCB specimen were designed to transfer the wedge load to the specimen without any motion in the out-of-plane direction and with free motion in the loading wedge direction. Figure 6.3 shows front and side views of the fixture used for the CLWL-DCB specimens. The split-pin loading system is shown in Figure 6.4.

The fixture and the split-pin loading system were designed for the following conditions:

1. The low-taper-angle loading wedge, with an included slope of 1/18 and a polished finish, provides a crack opening velocity of 0.05 mm/msec (0.002 in/msec) at the loading

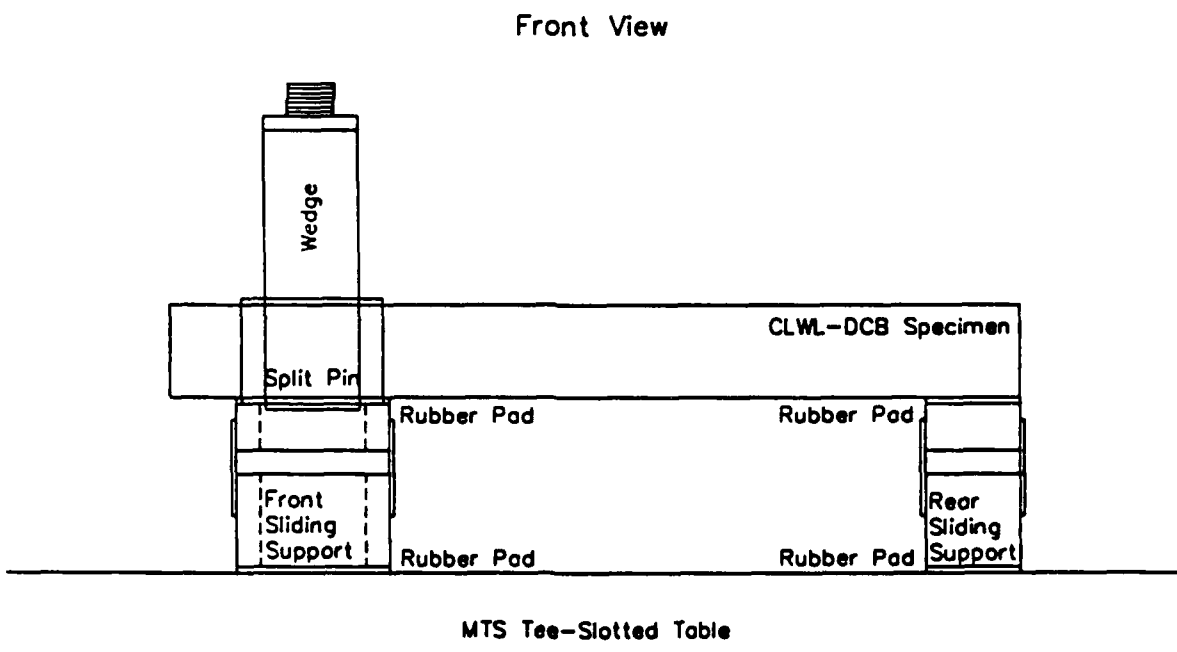
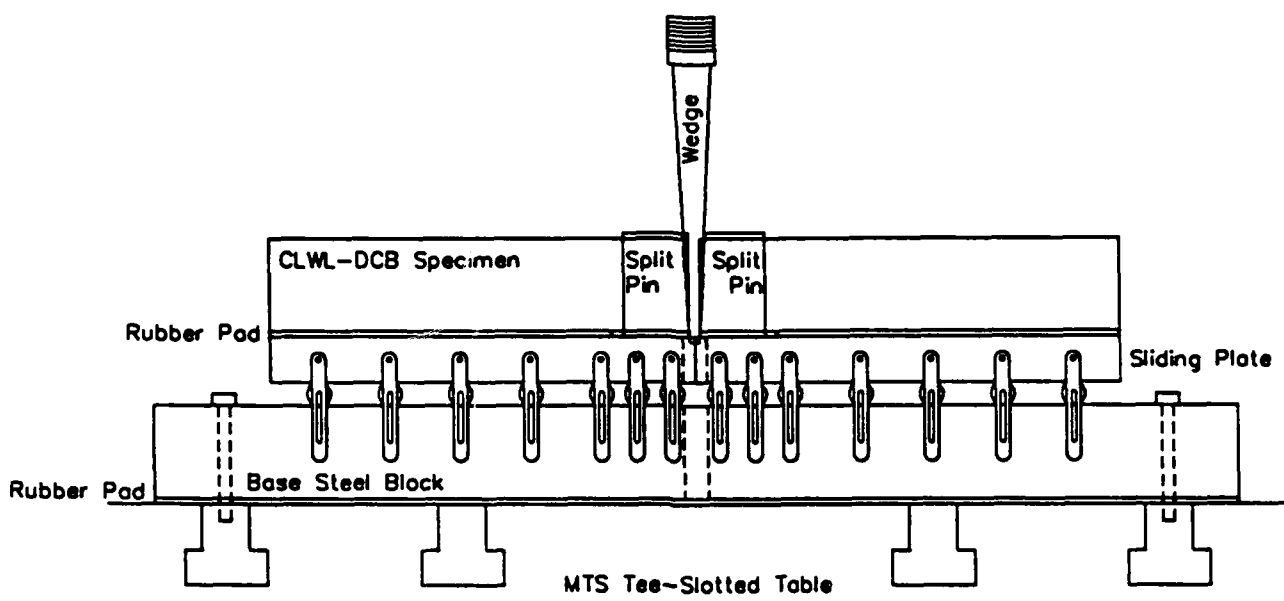


Figure 6.3: Fixture of CLWL-DCB Specimens

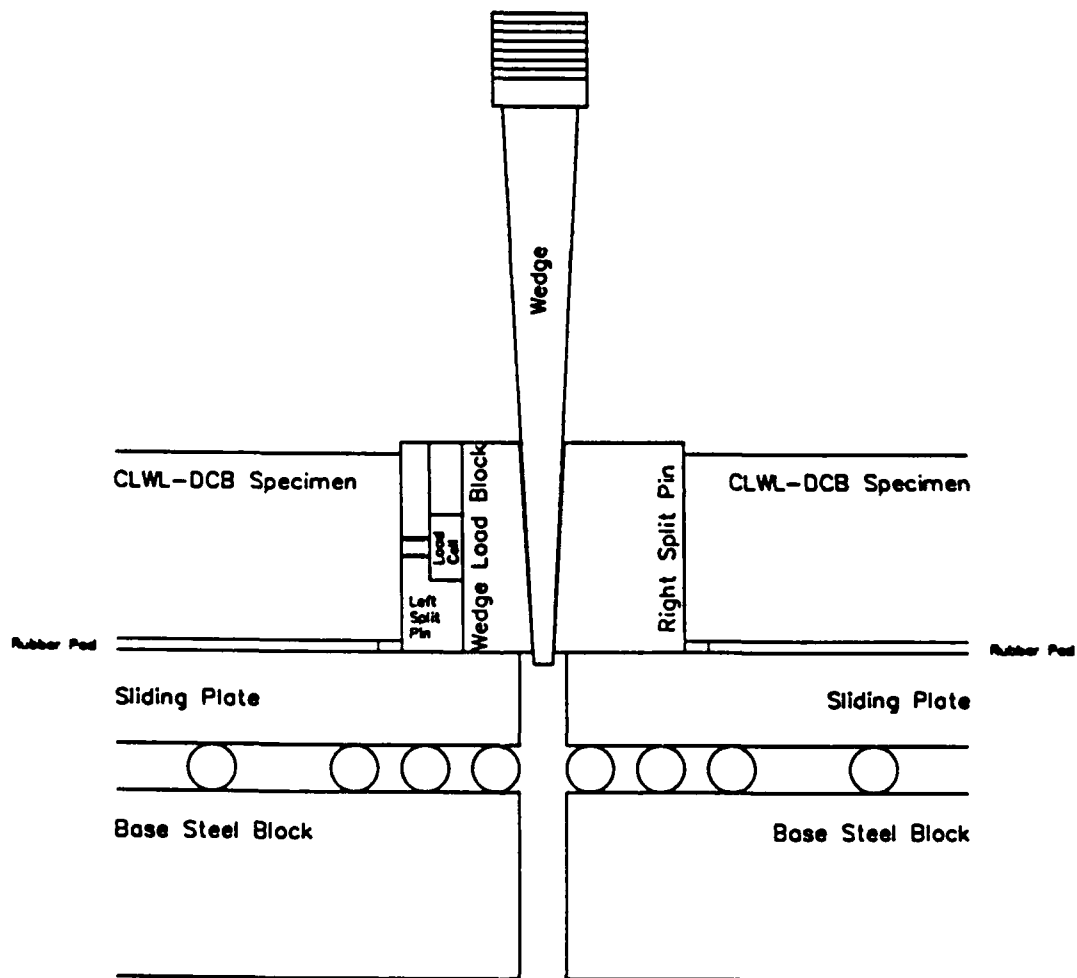


Figure 6.4: Details of Split-Pin Loading System

wedge location for a vertical wedge velocity of 0.9 m/sec  
(36 in/sec.)

2. The wedge load is measured by a dynamic load cell fixed vertically between the wedge-load block and the left-split pin (Figure 6.4).
3. To minimize the friction force in the wedge-load direction, steel rollers are used between the base and the sliding plates.
4. The main rigidity in the vertical direction is provided by the tee-slotted table of the MTS load frame to which the base plates are fixed.
5. Rubber pads are added between the sliding plates and the CLWL-DCB specimen to prevent oscillations in the out-of-plane direction.
6. To prevent rigid body rotations of the specimen and to guide the direction of crack growth so that it is straight from the notch tip, the four corners of the specimen are fixed to the sliding plates with clips.

The two non-contact capacitance gages were used to measure the two crack opening displacements,  $2V_1$  and  $2V_2$  in Figure 6.1. The load-line displacement,  $2V_p$ , was determined by linear

interpolation from the two crack-line displacements  $2V_1$  and  $2V_2$ . The external work history for the CLWL-DCB specimen was determined by integration of the load and load-line displacement histories. That history is being used to validate the numerical simulation of the test results since the external work history is a scalar quantity which represents the average responses of the entire system. Three strain gages were bonded at a half inch offset from the center line of the specimen, as shown in Fig. 6.1, for the same purpose as in the three-point bend test specimens. The locations for gages SGO1 and SGO3 were the same for all tests. The distance of gage SGO2 from SGO1 was 12.7 mm for some specimens and 38.1 mm for others. The analysis procedure being used is the same as that applied to the three-point bend test results for evaluation of the significance of the load, load-line displacement, and strain histories.

## **6.2 Numerical Analysis**

The numerical procedure being used to analyze the experimental results is identical to that described in the previous chapter with the only difference being the specimen geometry. Figure 6.5 shows the finite element model used to reduce the experimental data to the targeted dynamic fracture and elastic properties of the CLWL-DCB concrete specimens. At the time of this writing, that analysis was still in progress

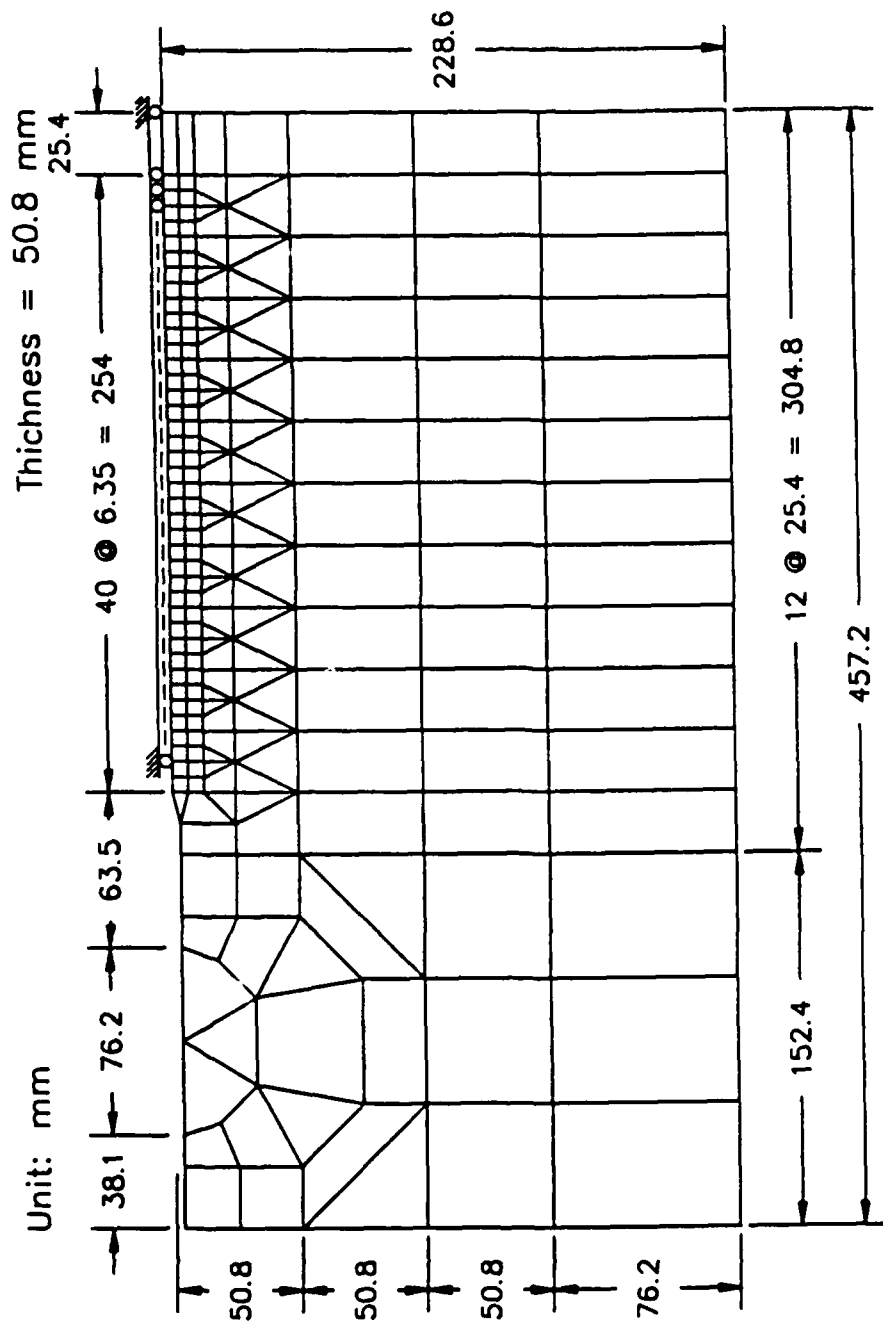


Figure 6.5: Finite Element Model of CLWL-DCB Specimen

and only preliminary findings are described in this report. Complete results will be presented in an addendum to this report to be issued shortly.

### **6.3 Results**

#### **6.3.1 Experimental Results**

A total of eleven CLWL-DCB concrete specimens were tested at varying strain rates. The test conditions for the eleven specimens are listed in Table 6.1. The symbols [1] and [2] in Column 1 of Table 6.1 indicate differences in the location of the second strain gage. For the symbol [1] the second strain gage was located 127 mm (5 in) from the loading wedge's line, and for the symbol [2] the second strain gage was located 152.4 mm (6 in) from that line.

Typical load and strain histories for the specimen, Test No. 2, which was loaded to failure in about 4 msec., are shown in Figure 6.6. The loading rate for Test No. 2 was the fastest rate in the whole test series. The time at which the FPZ tip was taken as passing a given gage position, is indicated by a symbol on the time history response for that gage. The locked-in shrinkage effects at the cast-in place notch tip were much less than those of the three point bend specimens, since as shown in Fig. 6.1, a saw-cut of 12.7 mm (0.5 in) length was made at the cast-in place notch tip to relieve those effects.

Table 6.1: CLWL-DCB Test Data

Test #	P <sub>max</sub> kN	T <sub>P</sub> msec	T <sub>1</sub> msec	T <sub>2</sub> msec	T <sub>3</sub> msec	ā <sub>1</sub> m/sec	ā <sub>2</sub> m/sec	a m/sec	W <sub>3</sub> kN-m
01[2]	12.4	2.54	1.63	2.56	3.88	40.7	144	101	2.44
02[2]	11.0	2.41	1.43	2.18	3.83	16.9	131	95.3	2.36
03[1]	10.1	6.55	4.50	5.90	14.4	9.07	25.1	23.2	1.87
04[2]	9.98	11.3	6.15	9.80	20.5	10.4	17.8	15.9	2.27
05[1]	9.34	40.6	19.2	31.4	78.8	1.04	4.55	3.84	2.21
06[2]	9.14	13.8	7.60	13.4	23.3	6.63	19.2	14.6	1.91
07[2]	8.79	48.5	30.0	50.5	118	1.86	2.85	2.62	1.81
08[1]	7.51	286	92.0	162	600	0.18	0.49	0.45	1.69
09[2]	7.42	108	71.5	110	239	1.00	1.47	1.36	1.53
10[2]	7.23	420	172	406	1136	0.163	0.262	0.237	1.68
11[2]	5.77	2000	932	-	-	-	-	-	-

- T<sub>i</sub> is the time when a micro-crack tip passes the depth of the strain gage *i*.
- T<sub>P</sub> is the time at the peak load P<sub>max</sub>.
- W<sub>3</sub> is the external work at T<sub>3</sub>.
- ā is the average crack velocity.

	[1]	[2]	
Δa <sub>1</sub> (mm)	12.7	38.1	ā <sub>1</sub> = Δa <sub>1</sub> /(T <sub>2</sub> -T <sub>1</sub> )
Δa <sub>2</sub> (mm)	216	191	ā <sub>2</sub> = Δa <sub>2</sub> /(T <sub>3</sub> -T <sub>2</sub> )
Δa (mm)	229	229	ā = Δa/(T <sub>3</sub> -T <sub>1</sub> )

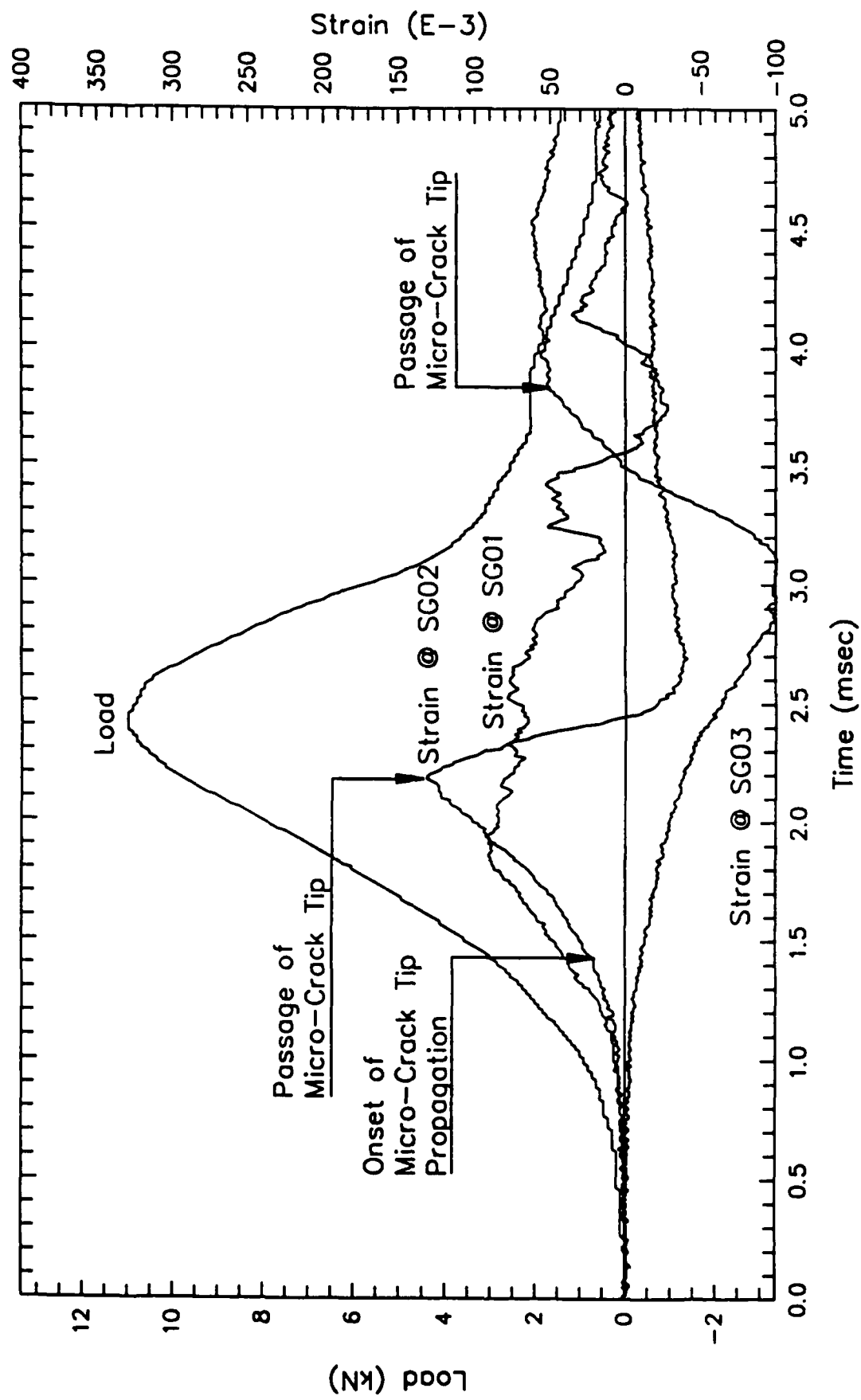


Figure 6.6: Load and Strain Histories of Test 2

Figure 6.7 shows the COD gage responses. The load and  $2V_1$  and  $2V_2$  are plotted against  $2V_p$  which is the load-point displacement linearly interpolated from  $2V_1$  and  $2V_2$ . The  $2V_1$  and  $2V_2$  data provided additional data, which together with the strain gage data, were used to match the numerical modelling in the hybrid experimental-numerical analysis. The locations for gages  $2V_1$  and  $2V_2$  are shown in Fig. 6.1.

Figures 6.8 and 6.9 show the corresponding data for specimen No. 07 which was tested to failure in about 120 msec. That rate was about the average loading rate for the whole test series. Figures 6.10 and 6.11 show the corresponding results for specimen No. 10 which was loaded to failure in about 1.2 sec. That loading rate was the slowest loading rate for which complete data were obtained.

Careful observations were also made of the fracture surfaces of the specimens and the deviations of the propagating crack from the centerline of the specimen. Procedures are being developed to describe numerically observed variations. However, qualitatively it was clear that, as described previously in Chapter 4, the roughness of the failure surface decreased and the degree of transgranular aggregate fracture increased as the loading rate increased. Further it was apparent that expected variations in the strain and displacement time histories were

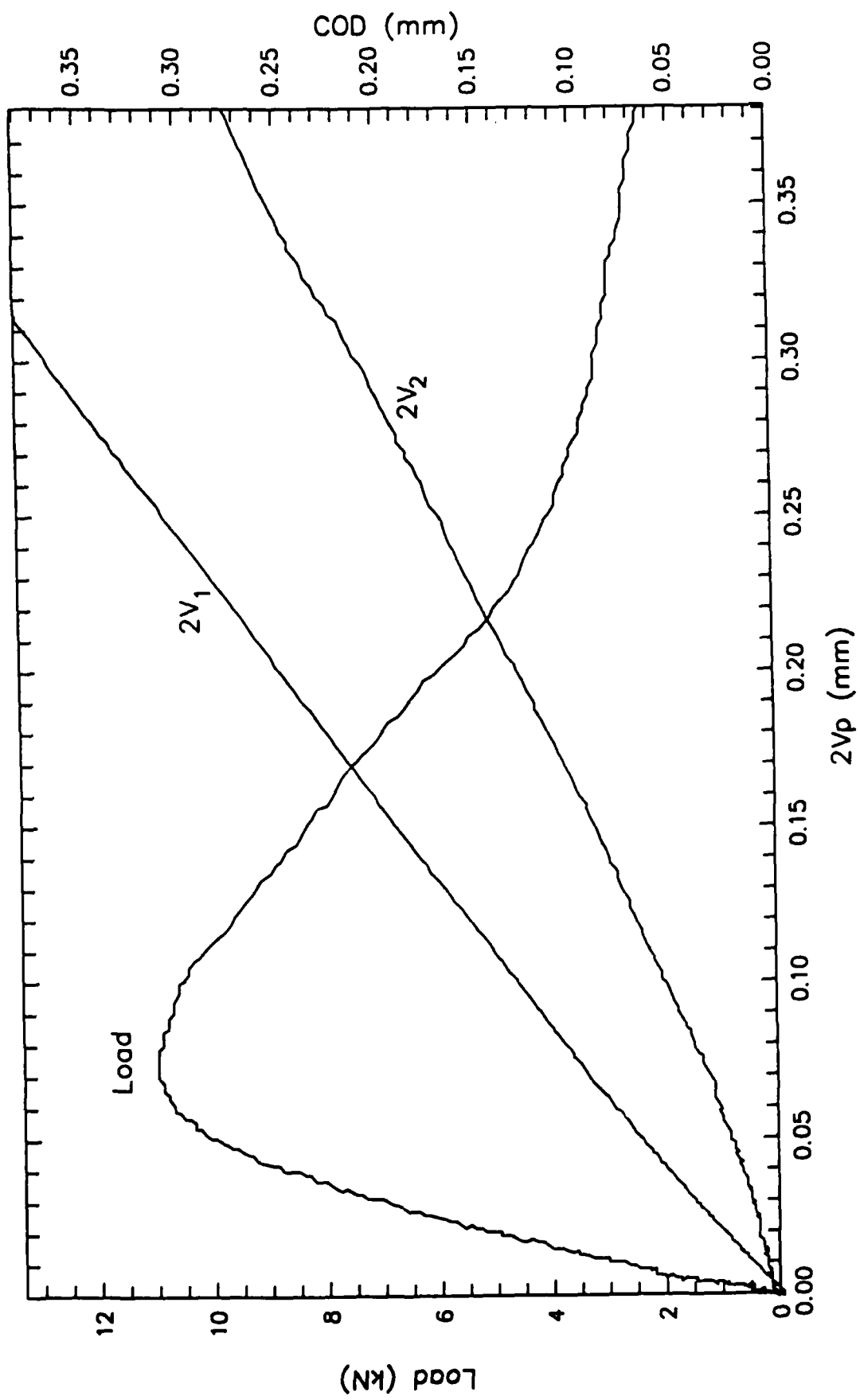


Figure 6.7:  $2V_1$ ,  $2V_2$  and Load against Load-Line Displacement of Test 2

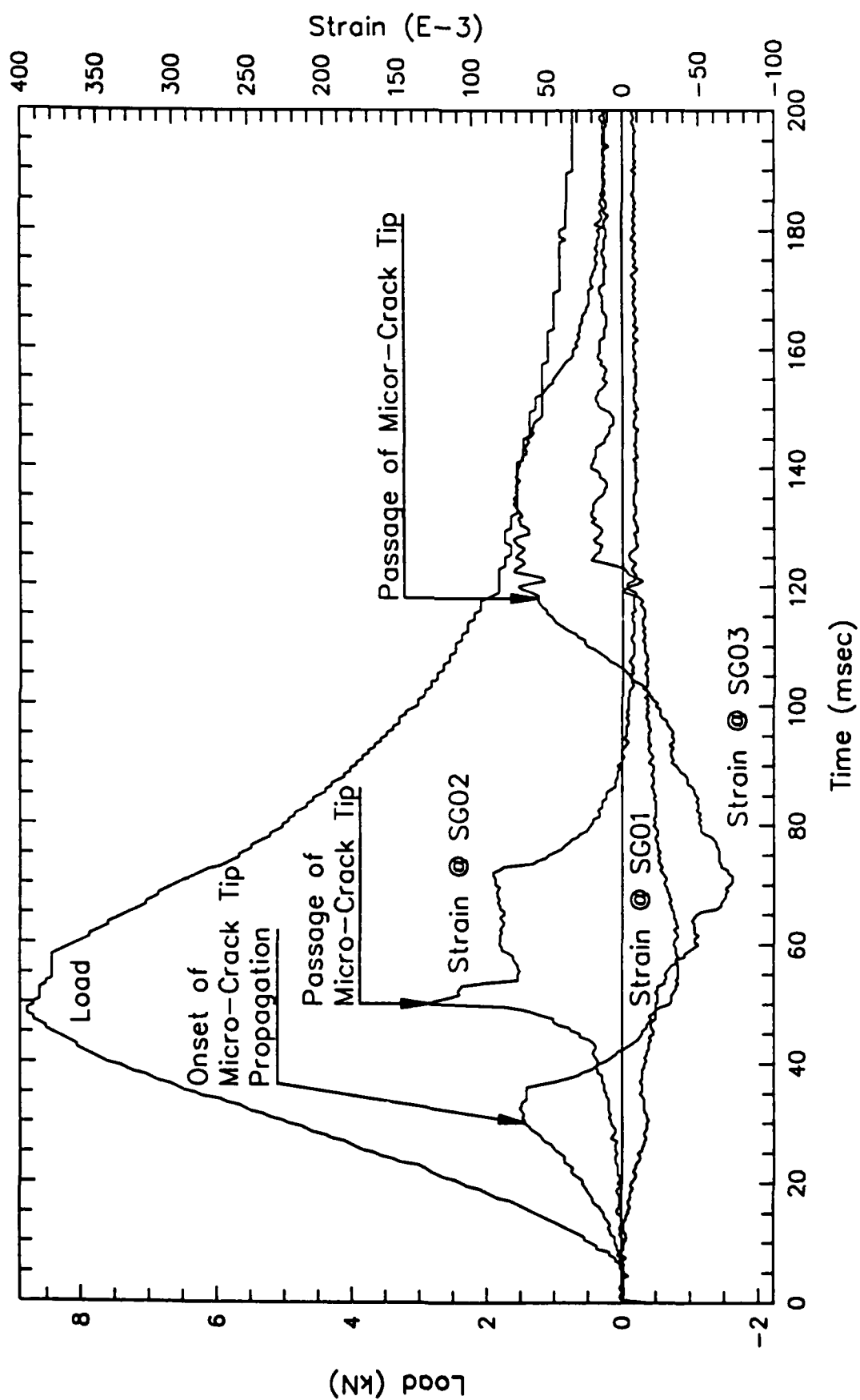


Figure 6.8: Load and Strain Histories of Test 7

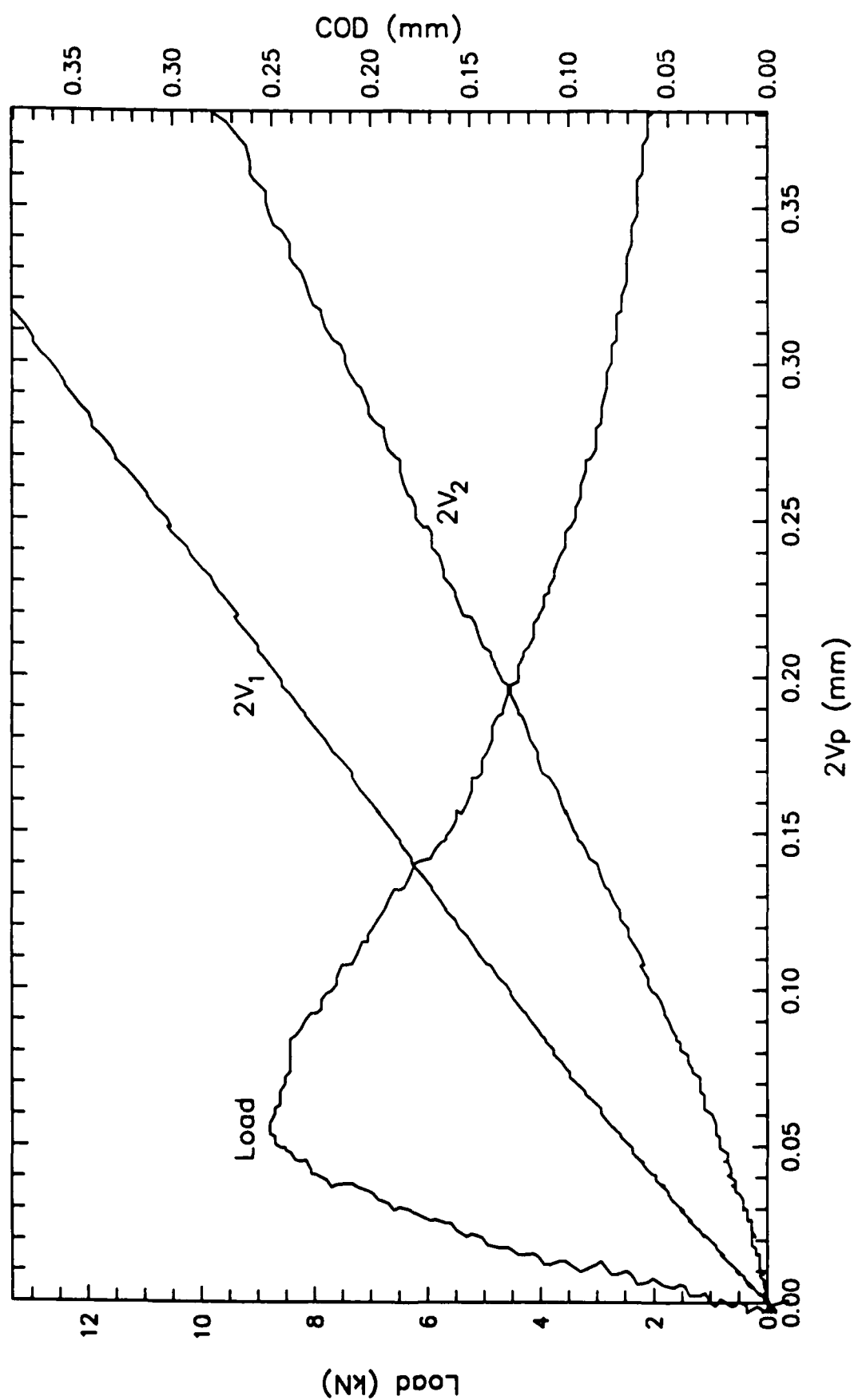


Figure 6.9:  $2V_1$ ,  $2V_2$  and Load against Load-Line Displacement of Test 7

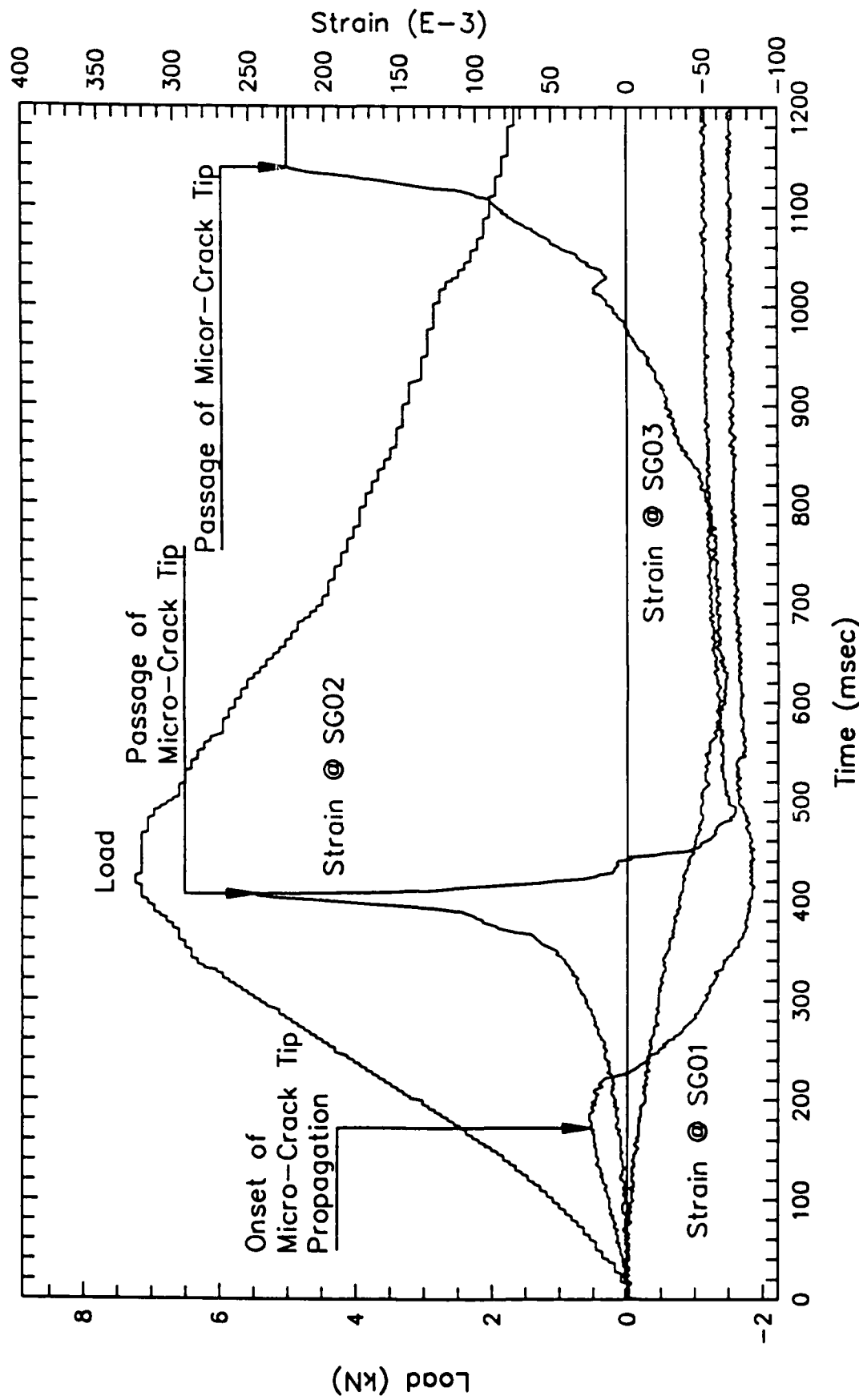


Figure 6.10: Load and Strain Histories of Test 10

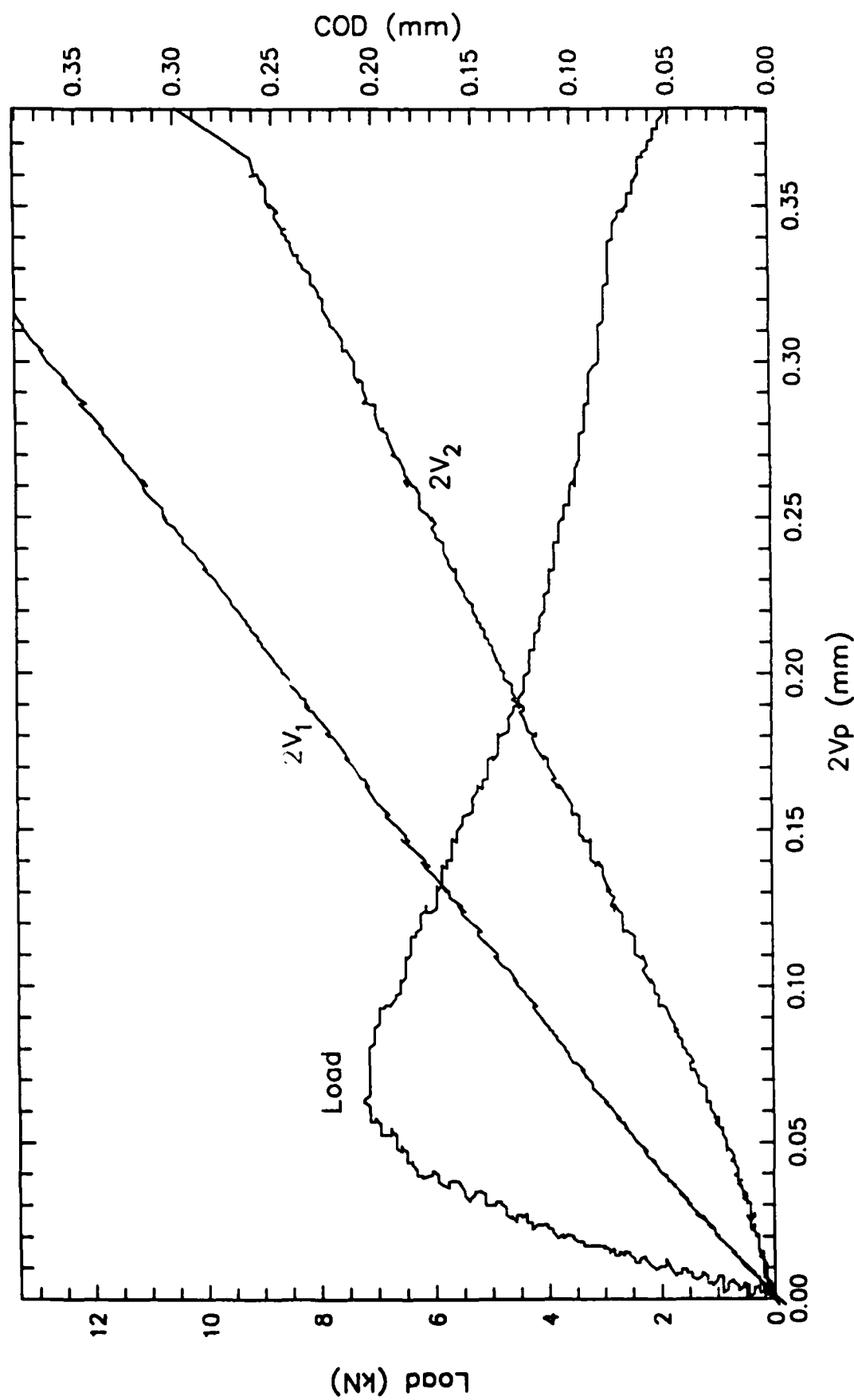


Figure 6.11:  $2V_1$ ,  $2V_2$  and Load against Load-Line Displacement of Test 10

often related to the initiation of gross deviations in the direction of the propagating crack from the centerline of the specimen.

### 6.3.2 Numerical Results

Critical test results as summarized in numerical form in Table 6.1 and experimental responses, as typified by responses of Figures 6.6 through 6.11, are being used as the experimental data for executing the inverse analysis to delineate dynamic effects. The  $2V_1$  and  $2V_2$  data indicate the approximate crack opening profile for the rapidly propagating crack and the need to satisfy that profile consistent with the strain and load data have significantly influenced the appropriate choice for the constitutive relation of the FPZ. Preliminary analysis favor constitutive relations of the form of Figure 5.11 rather than Figure 4.13.

### 6.4 Discussion

As described above, the results of a preliminary analysis of the CLWL-DCB tests indicate that the constitutive relation for a rapidly propagating FPZ is not only substantially different from that of a stably growing FPZ but that the limiting crack opening displacement ( $COD_c$  in Table 5.1) also diminishes in magnitude with increasing strain rate. It appears that the tensile strength value,  $f_{td}$  in Table 5.1, is more strain rate dependent than the maximum value  $f_{td}''$  of  $f_{ccs}$  the crack closing stress. Should the form of the relation of Figure 5.11

be verified from the CLWL-DCB experiments, then the results of Chapter 4 must be re-evaluated for consistency with the results of this investigation.

### **6.5 Conclusions**

1. From the analyses completed to date, it is clear that to obtain an adequate understanding of the dynamic fracture behavior of concrete, specimens with dimensions large enough to allow the full development of the FPZ, together with precise measurements of the accompanying displacements and loads are needed. The conditions of full development of the process zone, coupled with loads that are within the capabilities of normal testing facilities, are difficult to achieve with three point bend specimens. Even special facilities, such as the large drop weight apparatus reported in Ref. [3], do not allow full development of the FPZ. Data obtained using CLWL-DCB specimens are highly desirable since all necessary conditions can be achieved with such specimens, as demonstrated by the results reported here.
2. For future CLWL-DCB tests, it is desirable that additional recording channels be utilized. The crack opening profile could then be more accurately measured, and with more strain gages distributed along the centerline of the specimen, variations in the form of the FPZ and the

velocity of the crack and the reasons for those variations, could be better identified.

3. For future CLWL-DCV tests, it is desirable that crack opening profiles and displacements for dynamic loading be measured using Moire interferometry techniques. As demonstrated by the results in Part I and in Chapter 5 of this Part II, the form of the crack opening profile is an important criteria for verifying the form and magnitude of the crack closing pressures.

## CHAPTER 7

### SUMMARY

The objectives, described in Chapter One of this report, were all achieved except for the final numerical analysis of the CLWL-DCB specimens. The results from that analysis will be reported in a PhD dissertation by Jung Heum Yon which is expected to be completed by June 1990. Copies of this PhD dissertation will be submitted to the AFOSR contract monitor as a supplement to this report.

Specific results, achieved during the course of this investigation were as follows:

1. A displacement controlled dynamic test system and instrumentation for dynamic fracture testing of concrete specimens were developed.
2. The advantages and disadvantages of displacement control versus impact loading and the use of three point bend versus CLWL-DCB specimens for dynamic fracture testing of concrete were identified.
3. A hybrid experimental-numerical procedure for evaluating dynamic fracture properties of concrete from test data was developed. The ambiguity in this inverse analysis was

reduced through the use of that procedure combined with either the results of moire interferometry or dynamic COD measurements.

4. The strain sensitivities of the elastic properties and the fracture process zone characteristics of concrete were determined.

- a) The tensile strength increased with increasing strain rates with the log of the increase in strength increasing almost linearly with the log of the strain rate for values up to about  $0.2 \text{ sec}^{-1}$ . For higher strain rates, the increase was greater than for the logarithmic relation valid up to  $0.2 \text{ sec}^{-1}$ . At a strain rate of  $0.24 \text{ sec}^{-1}$ , the tensile strength was 110 percent of the static strength. At a strain rate of  $1.48 \text{ sec}^{-1}$ , the tensile strength was 330 percent of the static strength.
- b) The tensile and compressive moduli of elasticity increased with strain rate but percentage increases were much less than percentage increases in tensile strength.
- c) The average crack velocity increased with increasing strain rate. Values reached  $132 \text{ m/sec}$  and  $230 \text{ m/sec}$  for strain rates of  $0.24$  and  $1.48 \text{ sec}^{-1}$  respectively. Both velocity values are considerably less than the theoretical terminal velocity for crack propagation in concrete.

- d) The fracture energy density was found to be independent of strain rate and equal to 160 N/m for the concrete used in these tests.
- e) The influence of the FPZ on the fracture process decreased as the strain rate increased. At  $1.48 \text{ sec}^{-1}$ , the dynamic fracture process approached that for linear elastic fracture.
- f) The form of the FPZ changes with increasing strain rates. At the crack tip there is effectively a decoupling of the stress for advancement of that tip, the tensile strength, and the crack closing pressure immediately behind that tip. At a strain rate of  $1.48 \text{ sec}^{-1}$ , there was a difference of 2.5 in those values. The tensile strength is more strain rate dependent than the maximum crack closing pressure. The COD at which the crack closing pressure vanishes also diminishes with increasing strain rate.
- g) The percentage of transaggregate fractures increases as the strain rate increases so that the effective roughness of the fracture surface decreases as the strain rate increases.

## CHAPTER 8

### PUBLICATIONS FROM THIS STUDY

1. Kobayashi, A.S., Hawkins, N.M., and Bradt, R.C., "Non-linear Fracture of Concretes and Ceramics," *Non-Linear Fracture Mechanics*, eds. A. Saxena, J.D. Landes and JL. Bassani, ASTM, STP 995, 1989, pp 457-471.
2. Du, J.J., Kobayashi, A.S., and Hawkins, N.M., "Fracture Process Zone of a Concrete Fracture Specimen," *Fracture of Concrete and Rock*, eds, S.P. Shah and S.E. Swartz, Springer-Verlag, 1989, pp 199-204.
3. Du, J.J., "A Fracture Mechanics Study of Concrete Failure," Ph.D. thesis, Department of Mechanical Engineering, University of Washington, August 1988.
4. Nobuta, Y., "Applicability of Acoustic Emission Technique for Assessing Debonding Between Reinforcing Bars and Surrounding Concrete," M.S.C.E. thesis, Department of Civil Engineering, University of Washington, August 1988.
5. Du, J.J., Hawkins, N.M. and Kobayashi, A.S., "A Hybrid Analysis of Fracture Process Zone in Concrete," *Proceedings, International Conference on Recent Developments on the Fracture of Concrete and Rocks*, edited by S.P. Shah, S.E. Swartz, and B. Barr, Elsevier Applied Science, London, Sept 1989, p. 297-306.
6. Hawkins, N.M., Du, J.J., Yin, X., and Kobayashi, A.S., "Fracture Testing of CLWL-DCB Specimens," *Fracture Toughness and Fracture Energy: Test Methods for Concrete and Rock*, edited by H. Mihashi, H. Takahashi, and F.K. Wittman, A.A. Balkema, Rotterdam, 1989, p. 205-220.
7. Yon, J.H., Hawkins, N.M., and Kobayashi, A.S., "Dynamic Fracture Testing of Concrete Bend Specimens," *Fracture Toughness and Fracture Energy: Test Methods for Concrete and Rock*, edited by H. Mihashi, H. Takahashi, and F.K. Wittman, A.A. Balkema, Rotterdam, 1989, p. 489-500.
8. Hawkins, N.M., McCabe, W.M., and Nobuta, Y., and "Use of Acoustic Emission to Detect Debonding of Reinforcing Bars in Concrete," *Progress in Acoustic Emissions IV*, Japan Society for Non-Destructive Inspection, Kobe, Japan, November 1988, p. 342-349.
9. Hawkins, N.M., and Nobuta, Y., "Acoustic Emission Technique to Detect Debonding Between a Reinforcing Bar

and the Surrounding Concrete," *Proceedings, International Workshop on Nondestructive Evaluation for Performance of Civil Structures*, University of Southern California, Los Angeles, February 1988, pp. 231-240.

10. McCabe, W.M., and Nobuta, Y., "Detecting Rock Bolt and Reinforcing Bar Debonding Using the Acousto-Ultrasonic Method," *Proceedings, International Workshop on Nondestructive Evaluation for Performance of Civil Structures*, University of Southern California, Los Angeles, February 1988, pp. 341-347.
11. Du, J.J., Kobayashi, A.S., and Hawkins, N.M., "FEM Dynamic Fracture Analysis of Concrete Beams," *ASCE-EMD Journal*, Vol. 115, No. 10, October 1989, p. 2136-2149
- b. Accepted for publication
12. Du, J.J., Kobayashi, A.S., and Hawkins, N.M., "An Experimental-Numerical Analysis of Fracture Process Zone in Concrete Fracture Specimens," *Engineering Fracture Mechanics*.
13. Liaw, B., Jeang, F.L., Hawkins, N.M., and Kobayashi, A.S., "An Improved Linear Model for Concrete Fracture," *ASCE-EMD Journal*, February 1990.
14. Yon, J.H., Hawkins, N.M., and Kobayashi, A.S., "Dynamic Fracture of Concrete," *Proceedings, Oji International Seminar on dynamic Fracture*, Toyohashi, Japan, August, 1989.
15. Du, J.J., Kobayashi, A.S., and Hawkins, N.M., "A Direct FEM Concrete Fracture Procedure," *ASCE-EMD Journal*, March 1990.
16. Akutagawa, S., Jeang, F.L., Du, J.J., Hawkins, N.M., and Kobayashi, A.S., "Effects of Loading History on Fracture Properties of Concrete," *Journal of American Concrete Institute*, accepted Sept 1989.
17. Du, J., Yon, J.H., Hawkins, N.M., Arakawa, K., and Kobayashi, A.S., "Analysis of the Fracture Process Zone of a Propagating Concrete Crack Using Moire Interferometry," *Proceedings, International Conference on Micromechanics of Failure of Quasi-Brittle Materials*, Elsevier, June 1990.
18. Yon, J.-H., Hawkins, N.M. and Kobayashi, A.S., "Strain Rate Sensitivity of Concrete Mechanical Properties," *ACI Materials Journal*.

19. Liaw, B.M., Jeang, F.L., Hawkins, N.M., and Kobayashi, A.S., "Fracture Process Zone for Mixed-Mode Concrete Fracture," *ASCE EMD Journal*.
- c. Submitted for Publication
20. Du, J., Yon, J.H., Hawkins, N.M., Arakawa, K., and Kobayashi, A.S., "Fracture Process Zone for Concrete for Dynamic Loading," submitted to *ACI Materials Journal*.

## CHAPTER 9

### RECOMMENDATIONS FOR FUTURE RESEARCH

#### 9.1 Justification

Damage analysis of concrete based on dynamic fracture mechanics is still in its developmental stage. The changes observed in the fracture process zone with strain rate in this report vividly demonstrate the decreasing influence of the dominant fracture energy dissipation mechanism, i.e., the fracture process zone, with increasing dynamic effects. Presumably, a better knowledge of the macro- and micro-mechanisms, which trigger this effect, would provide the basis for designing a concrete structural component to retain its static fracture process zone during rapid crack propagation and hence be engineered against dynamic fracture. For example, trans-aggregate failure during rapid crack propagation could possibly be decreased by using stronger and larger aggregates together with stronger interfacial adhesion with the cement. It is well known that the toughness of concrete can also be increased by the addition of fibers [3, 32, 33] and theoretically it should be possible to predict the response for planar damage in a fiber reinforced concrete by combining the response predicted for the fibers crossing the damage plane with the response predicted for the matrix (concrete) crossing the same plane.

## **9.2 Recommended Research**

It is recommended that a hybrid experimental-numerical method be used to delineate the macro- and micro-mechanics of dynamic fracturing of concrete. The macro-fracture work should involve static and dynamic, mode I and mixed mode fracture testing of CLWL-DCB specimens and three- and four-point bend concrete specimens using the displacement controlled test set-up already developed. All specimens should have extensive strain gage and COD gage instrumentation utilizing the multichannel recording systems purchased under the AFOSR Equipment Grant No. 89-0123 to the Department of Civil Engineering. Fractography analyses of the fracture surfaces and profilometer measurements of cross sections normal to the crack should be used to document micro-mechanics contributions to the observed macro-mechanic response and for the formulation of a mathematical model to predict those contributions from the physical and mechanical characteristics, and the gradation, of the aggregate.

In order to extend the maximum rate of straining to values greater than those which can be obtained with the MTS servo-hydraulic testing machine, tests should also be made using impact loading. The initial work should be done using small-scale CLWL-DCB specimens impact loaded in the drop-weight facility in the Fracture Mechanics Laboratory of the Department of Mechanical Engineering. That work should be complemented with the testing of large-scale CLWL-DCB specimens impact loaded in the drop weight facility in the Department of Civil Engineering at the University of British Columbia. These drop-weight tested

specimens should be instrumented so that with both strain and displacement gages, and with moire interferometry, the transient displacement field in the vicinity of the running crack can be determined.

Linear and nonlinear finite element analyses should be used to analyze the experimental results to determine the transient states displacement of stress and strain and hence the fracture parameters in those statically and dynamically loaded specimens.

Experimental procedures should follow those used previously for static loadings with careful screening of constituent materials, and the simultaneous casting and curing of the multiple specimens in a given test group. CLWL-DCB specimens should be tested having wider variations in maximum aggregate size and in aggregate gradation than used previously. Maximum aggregate size should range from 3/4 to 1/4 inch. Careful attention in the static tests should be given to "creep" effects so that strain rate effects for the static loading can be defined [14]. While the experimental results should guide the direction of any subsequent test in a given series, the basic hypothesis of a dual mechanism of crack bridging at the FPZ and brittle fracture based on LEFM should be probed analytically and, if necessary, an alternate basic hypothesis formulated and tested analytically. If any crack branching effects are observed experimentally, the significance of that branching should be investigated analytically.

### 9.3 Relevancy

In order to assess the durability of a concrete runway, which is an essentially unreinforced structure subjected to repeated impact loadings, it is highly desirable to know the dynamic material, as well as dynamic fracture, properties of concrete. In addition, fundamental knowledge on the strain rate dependency of concrete tensile strength is also desirable for assessing the through-wall shear strength of a concrete silo or the through-roof or wall shear strength of slabs for magazines and other base facilities which may be subjected to either conventional or nuclear weapon explosions.

In addition to the need for procedures to assess the dynamic fracture properties of concrete, there is an equal need for procedures to assess the significance of pre-existing cracks for estimates of the residual life of runways, missile silos, slabs and walls and for establishing strategies and schedules for maintenance, upgrading and strengthening of existing structures. The CLWL-DCB specimen developed by the investigators for quasi-static testing is ideal for examination of those issues and their implications for dynamic loading situations. The specimen has a large enough planar surface that crack propagation, crack reflection, and FPZ variation effects can be identified.

## REFERENCES

1. H.W. Reinhardt. Tensile fracture of concrete at high rates of loading. In S.P. Shah, editor, *Application of Fracture Mechanics to Cementitious Composites*, pages 539-590, Martinus Nijhoff Publisher, 1985.
2. S. Mindess. Rate of loading effects on the fracture of cementitious materials. In S.P. Shah, editor, *Application of Fracture Mechanics to Cementitious Composites*, pages 465-484, Martinus Nijhoff Publisher, 1985.
3. A. Bentur, S. Mindess, and N. Banthia. The fracture of reinforced concrete under impact loading. In S. Mindess and S.P. Shah, editors, *Cement-Based Composites: Strain Rate Effect on Fracture*, pages 225-234, Material Research Society, Pittsburgh, 1986.
4. O.S. Lee, A.S. Kobayashi, and A. Komine. Crack tip plasticity of a tearing crack. *Experimental Mechanics*, 25:66-74, 1985.
5. D.S. Dugdale. Yielding of steel sheets containing slits. *Journal of Mechanics and Physics of Solid*, 8:100-104, 1960.
6. A. Hillerborg, M. Modeér, and P.-E. Petersson. Analysis of crack formation and crack growth in concrete by means of fracture mechanics and finite elements. *Cement and Concrete Research*, 6:773-782, 1976.
7. M. Wecharatana and S.P. Shah. Prediction of nonlinear fracture process zone in concrete. *Journal of Engineering Mechanics, ASCE*, 109:1231-1246, 1983.
8. Z.P. Bažant and S.S. Kim. Plastic-fracturing theory for concrete. *Journal of Engineering Mechanics, ASCE*, 105:407-428, 1979.
9. W. Suaris and S.P. Shah. Properties of concrete subjected to impact. *Journal of Structural Engineering, ASCE*, 109:1727-1741, 1983.
10. H. Green. Impact strength of concrete. *Proceedings of the Institution of Civil Engineering*, 28:383-396, 1964.
11. W. Goldsmith, V.H. Kenner, and E.E. Ricketts. Dynamic loading of several concrete-like mixtures. *Journal of Structural Engineering, ASCE*, 94:1803-1827, 1968.
12. R.L. Sierakowski. Dynamic effects in concrete materials. In S.P. Shah, editor, *Application of Fracture Mechanics to*

*Cementitious Composites*, pages 391-411, Northwestern University, 1984.

13. F.L. Jeang and N.M. Hawkins. *Non-Linear Concrete Fracture in CLWL-DCB Specimens*. Technical Report SM 85-2, Department of Civil Engineering, University of Washington, Seattle, 1985.
14. S. Akutagawa. *Experimental Investigation of the Fracture Process Zone of Concrete CLWL-DCB Specimens*. Master's thesis, Department of Civil Engineering, University of Washington, 1984.
15. S. Mindess and A. Bentur. A preliminary study of the fracture of concrete beams under impact loading, using high speed photography. *Cement and Concrete Research*, 15:474-484, 1985.
16. S. Ziegeldorf. Phenomenological aspects of the fracture of concrete. In F.H. Wittmann, editor, *Fracture Mechanics of Concrete*, pages 31-41, Elsevier Science Publishers, Amsterdam, 1983.
17. T.C. Hsu, F.O. Slate, and G.M. Sturman. Microcracking of plain concrete and shape of the stress-strain curve. *Journal of the American Concrete Institute*, 60:209-224, 1963.
18. F.O. Slate and S. Olsefsky. X-rays for study of internal structure and microcracking of concrete. *Journal of the American Concrete Institute*, 60:575-588, 1963.
19. R.K. Dhir and C.M. Sangha. Development and propagation of microcracks in plain concrete. *Matériaux et Constructions*, 7:17-23, 1974.
20. J. Glucklich. The effect of microcracking on time-dependent deformations and the long-term strength of concrete. In A.E. Brooks and K. Newman, editors, *The Structure of Concrete*, pages 176-189, Proceedings of International Conference, London, 1965, Cement and Concrete Association, London, 1968.
21. R.N. Swamy. Aggregate-matrix interaction in concrete systems. In *Structure, Solid Mechanics and Engineering Design*, pages 301-315, Wiley-Interscience, 1971.
22. F.O. Slate. X-ray technique for studying cracks in concrete with emphasis on method developed and used at Cornell University. In F.H. Wittmann, editor, *Fracture Mechanics of Concrete*, pages 85-93, Elsevier Science Publishers, Amsterdam, 1983.

23. H. Rüsh. Research forward a general fractural theory for structural concrete. *Journal of the American Concrete Institute*, 57:1-28, 1960.
24. R.H. Evans and M.S. Marathe. Microcracking and stress-strain curves for concrete in tension. *Matériaux et Constructions*, 1:61-64, 1968.
25. P.-E. Petersson. Fracture energy of concrete: practical performance and experimental results. *Cement and Concrete Research*, 10:91-101, 1980.
26. L. Cedolin, S. Dei Poli and I. Iori. Experimental determination of the stress-strain curve and fracture energy for concrete in tension. In *Proceedings of International Conference on Constitutive Laws for Engineering Materials*, pages 393-398, University of Arizona, 1983.
27. L. Cedolin, S. Dei Poli and I. Iori. Tensile behavior of concrete. *Journal of Engineering Mechanics, ASCE*, 113:431-449, 1987.
28. H.A.W. Cornelissen, D.A. Hordijk, and H.W. Reinhardt. Experimental determination of crack softening characteristics of normalweight and lightweight concrete. *Heron*, 31(2):45-56, 1986.
29. D.Z. Yankelevsky and H.W. Reinhardt. Response of plain concrete to cycle tension. *Material Journal, ACI*, 84:365-373, 1987.
30. M.F. Kaplan. Strain and stresses of concrete at initiation of cracking and near failure. *Journal of the American Concrete Institute*, 60:853-880, 1963.
31. A. Hillerborg. Analysis of one single crack. In F.H. Wittmann, editor, *Fracture Mechanics of Concrete*, pages 223-249, Elsevier Science Publishers, Amsterdam, 1983.
32. V.K. Nanda and D.J. Hannant. Fiber reinforced concrete. *Concrete Bldg. and Concrete Pros.*, XLIV:179-181, 1969.
33. ACI Committee 544. Measurement of properties of fiber reinforced concrete. *Journal of the American Concrete Institute*, 75:283-289, 1978.
34. W. Suaris and S.P. Shah. Inertial effect in the instrumented impact testing of cementitious composites. *Cement, Concrete and Aggregates, ASTM*, 3:77-83, 1981.
35. S. Mindess, N.P. Bantia, A. Ritter, and J.P. Skalny. Crack development in cementitious materials under impact loading.

In S. Mindess and S.P. Shah, editors, *Cement-Based Composites: Strain Rate Effects on Fracture*, pages 217-223, Material Research Society, Pittsburgh, 1986.

36. ASTM E23-86. Notched bar impact testing of metallic material. In *Annual Book of ASTM Standards*, pages 282-306, American Society for Testing and Materials, Philadelphia, 1987.
37. J.E. Bluhm. The influence of pendulum flexibilities on impact energy measurements. In *ASTM STP 167*, pages 84-92, American Society for Testing and Materials, 1955.
38. H. Krenchel. Fiber reinforced brittle matrix materials. In *ACI Publication SP 44*, pages 45-77, American Concrete Institute, Detroit, 1974.
39. C.D. Johnston. Steel fiber reinforced mortar and concrete—a review of mechanical properties. In *ACI Publication SP 44*, pages 127-142, American Concrete Institute, Detroit, 1974.
40. A.P. Hibbert. *Impact Resistance of Fibre Concrete*. PhD thesis, University of Surrey, 1977.
41. W. Radomski. Application of the rotating impact machine to testing fiber reinforced concrete. *International Journal of Cement Composites and Lightweight Concrete*, 3:3-12, 1981.
42. V.S. Gopalaratnam, S.P. Shah, and R. John. A modified instrumented Charpy test for cement based composites. *Journal of Experimental Mechanics, SEM*, 24:102-111, 1984.
43. V.S. Gopalaratnam and S.P. Shah. Properties of steel fiber reinforced concrete subjected to impact loading. *Journal of the American Concrete Institute*, 83:117-126, 1986.
44. V.S. Gopalaratnam and S.P. Shah. Strength, deformation and fracture toughness of fiber cement composites at different rates of loading. In S.P. Shah and A. Skarendahl, editors, *Steel Fiber Concrete*, pages 299-331, Proceedings of U.S.-Sweden Seminar (NSF-STM), Elsevier Applied Science Publishers, U.K., 1986.
45. J. Bhargava and A. Rehnstrom. Dynamic strength of polymer modified and fibre-reinforced concrete. *Cement and Concrete Research*, 7:199-207, 1977.
46. H.W. Reinhardt, H.A. Kormeling, and A.J. Zielinski. The split Hopkinson bar, a versatile tool for the impact testing of concrete. *Matériaux et Constructions*, 19:55-63, 1986.

47. I. Jawed, G. Childs, A. Ritter, S. Winzer, T. Johnson, and D. Barker. High-strain-rate behavior of hydrated cement pastes. *Cement and Concrete Research*, 17:433-440, 1987.
48. D.L. Birkimer and R. Lindeman. Dynamic tensile strength of concrete materials. *Journal of the American Concrete Institute*, 68:47-49, 1971.
49. J.K. Gran and L. Seaman. Strain-softening calculations for concrete in dynamic uniaxial tension. *Journal of Engineering Mechanics, ASCE*, 114:1911-1928, 1988.
50. K. Kobayashi and R. Cho. Flexural behavior of polyethylene fibre reinforced concrete. *International Journal of Cement Composites and Lightweight Concrete*, 3:19-25, 1981.
51. D.A. Abrams. Effect of rate of application of load on the compressive strength of concrete. In *ASTM STP 17, Part 2*, pages 364-367, 1917.
52. B.L. MacNeely and S.D. Lash. Tensile strength of concrete. *Journal of the American Concrete Institute*, 60:751-760, 1963.
53. B.L. Atchly and H.L. Furr. Strength and energy absorption capacity of plain concrete under dynamic and static loading. *Journal of the American Concrete Institute*, 64:745-756, 1967.
54. B.P. Hughes and R. Gregory. Concrete subjected to high rates of loading in compression. *Magazine of Concrete Research*, 24(78):25-36, 1972.
55. B.P. Hughes and A.J. Watson. Compressive strength and ultimate strain of concrete under impact loading. *Magazine of Concrete Research*, 30(105):189-199, 1978.
56. A.S. Evans. Slow crack growth in brittle materials under dynamic loading conditions. *International Journal of Fracture*, 10:251-259, 1974.
57. S. Mindess and J.S. Nadeau. Effect of loading rate on the flexural strength of mortar. *Journal of the American Ceramic Society*, 56:429-430, 1977.
58. H. Mihashi and M. Izumi. A stochastic theory for concrete fracture. *Cement and Concrete Research*, 7:411-421, 1977.
59. B. Zech and F.H. Wittmann. Variability and mean value of strength as a function of load. *Journal of the American Concrete Institute*, 77:358-362, 1980.
60. S.P. Shah and R. John. Rate-sensitivity of mode I and mode II fracture of concrete. In S. Mindess and S.P. Shah,

editors, *Cement-Based Composites: Strain Rate Effects on Fracture*, pages 21-37, Material Research Society, Pittsburgh, 1986.

61. A.J. Zielinski and H.W. Reinhardt. Stress, strain behavior of concrete and mortar at high rates of tensile loading. *Cement and Concrete Research*, 3:309-319, 1982.
62. A.J. Zielinski. Model for tensile fracture of concrete at high rates of loading. *Cement and Concrete Research*, 14:215-224, 1984.
63. H.W. Reinhardt. Strain rate effects on the tensile strength of concrete as predicted by thermodynamic and fracture mechanics models. In S. Mindess and S.P. Shah, editors, *Cement-Based Composites: Strain Rate Effects on Fracture*, pages 1-13, Material Research Society, Pittsburgh, 1986.
64. L.E. Malvern, T. Tang, D.A. Jenkins, and J.C. Gong. Dynamic compressive strength of cementitious materials. In S. Mindess and S.P. Shah, editors, *Cement-Based Composites: Strain Rate Effects on Fracture*, pages 119-138, Material Research Society, Pittsburgh, 1986.
65. O.C. Zienkiewicz. *The Finite Element Method*. McGraw-Hill, London, third edition, 1977.
66. A.S. Kobayashi. Dynamic fracture analysis by dynamic finite element method-generation and propagation analysis. In N. Perrone and S.N. Atluri, editors, *Nonlinear and Dynamic Fracture Mechanics*, pages 19-36, ASME, AMD-35, 1979.
67. A.S. Kobayashi. Hybrid experimental-numerical stress analysis. *Experimental Mechanics*, 23:338-347, 1983.
68. B.M. Liaw, F.L. Jeang, J.J. Du, N.M. Hawkins and A.S. Kobayashi, "An Improved Non-linear Model for Concrete Fracture," to be published in *Journal of Engineering Mechanics, ASCE*.
69. J.J. Du, A.S. Kobayashi and N.M. Hawkins, "An Experimental-Numerical Analysis of Fracture Process Zone in Concrete Fracture Specimens," to be published in *Engineering Fracture Mechanics*.
70. J.J. Du, A.S. Kobayashi and N.M. Hawkins, "FEM Dynamic Fracture Analysis of Concrete Beams," *Journal of Engineering Mechanics, ASCE*, Vol. 115, No. 10, Oct. 1989, p. 2136-2149.
71. N.M. Hawkins, A.S. Kobayashi and J.J. Du, "An Impact Damage Model of Concrete," *Cement Based Composites: Strain Rate Effects of Fracture*, ed. by S. Mindess and S.P. Shaw, Material Research Society, Pittsburgh, 1986, pp. 203-215.

72. Jiaji Du, N.M. Hawkins and A.S. Kobayashi, "A Hybrid Analysis of Fracture Process Zone in Concrete," *Fracture of Concrete and Rock, Recent Development*, eds. S.P. Shah, S.E. Swartz and B. Barr, Elsevier Applied Science, pp. 297-306, 1989.
73. Mehmet A. Tasdemir, Arup K. Magi and Surrendra Shah, "Mixed Mode Crack Propagation in Concrete Under Uniaxial Compressive Loading," *Fracture of Concrete and Rock, Recent Development*, eds. S.P. Shah, S.E. Swartz and B. Barr, Elsevier Applied Science, pp. 615-624, 1989.
74. J. Du. *A Fracture Mechanics Study of Concrete Failure*. PhD thesis, Department of Mechanical Engineering, University of Washington, Seattle, 1988.
75. Y.S. Jenq and S.P. Shah, "Two Parameter Fracture Model for Concrete," *Journal of Engineering Mechanics, ASCE*, Vol. 111, No. 4, pp. 1227-1241, October 1985.
76. ASTM E561-86. R-curve determination. In *Annual Book of ASTM Standards*, pages 793-812, American Society for Testing and Materials, Philadelphia, 1987.

ASK:cm/sag3